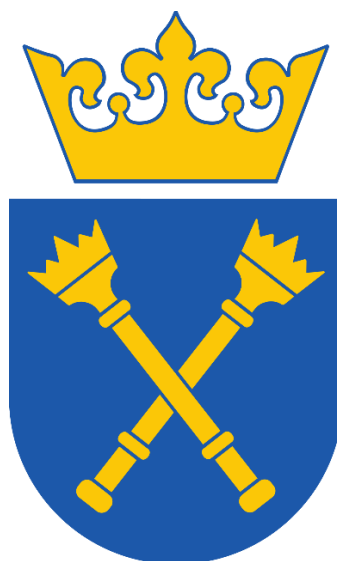


**Spectroscopic molecular probes of endothelial function
and dysfunction in *in vitro* models and their potential in *ex
vivo* applications**

Bassem Radwan, MPharm

Submitted in fulfilment of the requirements for the degree of
Doctor of Philosophy

Faculty of Chemistry,
Jagiellonian University in Krakow



Supervisor: Prof. Dr. hab. Małgorzata Barańska

Faculty of Chemistry and Jagiellonian Centre for Experimental
Therapeutics,
Jagiellonian University, Krakow, Poland

Acknowledgements

I have been lucky enough to receive so much help and support since the beginning of my PhD journey until this moment on both the professional and personal levels. It is more than fair to say that this thesis and the underlying work done towards achieving it would not have been possible without the immense support I received.

First and foremost, I would like to express my sincerest gratitude to my supervisor, Prof. Malgozata Baranska for her continuous support, guidance, trust and patience. I am truly grateful for her as she has given me the opportunity to learn and improve a lot, for encouraging me to challenge myself, and for pushing me to always achieve more.

I am very grateful to my professors at Jagiellonian University, where I have had the great fortune to study and work. I would like to express my thanks, especially to Prof. Wojciech Macyk, the dean of the Faculty of Chemistry, Prof. Artur Michalak and Prof. Barbara Gil for their great help and flexibility throughout the process of finalizing my PhD, despite their busy schedules. My gratitude extends to my thesis advisory committee members.

I would like to extend my thanks to the research and the administrative staff at the Jagiellonian Centre for Experimental Therapeutics (JCET), where I spent the past few years learning and following my passion. My gratefulness especially goes to Prof. Stefan Chlopicki, the director of JCET for his valuable insights and support. I am also grateful to the senior researchers at JCET who were generous enough to share their knowledge and expertise with me, helping me improve my skills substantially, starting from Dr. Krzysztof Czamara who was the first to introduce me to the techniques I would later depend on for my PhD work. I would like to extend my thanks to Dr. Ewelina Matuszyk and Dr. Magdalena Sternak who have been very helpful and supportive, and Mr. Stefano Rocchetti who was to me a great friend and a familiar colleague sharing my expat experience as well as the passion for science and the frustrations accompanying the quest for this passion.

I have had the great pleasure of being a part of the Raman Imaging Group of Jagiellonian University, whose team members made my life easier, supporting me through lengthy

bureaucratical processes. Moreover, I thoroughly enjoyed learning, discussing and sharing my progress during the team meetings and seminars. I am truly grateful for the whole team, and especially to Ms. Adrianna Wislocka–Orlowska whose help and involvement with various documents and processes throughout my stay in Poland made it possible for me to go so far.

My gratitude extends to my superiors and colleagues from different institutions within the framework of LogicLab ITN who created an international cooperative environment where I had the chance to learn about different subjects in a truly multidisciplinary setting.

Last but definitely not least, I owe my life, my very understanding of love, my sanity and the will to wake up every morning to my family. To my dad, who lives forever in the hearts and minds of the people who love him and whom he taught and helped to an infinite degree. Thank you for teaching me that "... that which benefits people remains on the earth (forever)." even if I might have learned it a bit too late. To my mom who taught me how to be my own person, who always accepts me for who I am and who made me passionate to always learn and look for knowledge. To my brother, I truly could not have asked for a better companion, I love you more than I can understand. And to my wife, my chosen family, and my best friend who tolerated so much and lived through the good, the bad and the very bad with me. I love you, and I thank you more than words can describe.

The work undertaken throughout my PhD was supported by the "European Union's Horizon 2020 Research and Innovation Programme under Marie Skłodowska-Curie [Grant Agreement 813920 (LogicLab ITN)]". Some of the work was supported by "a grant from the National Science Center Poland (NCN) (Opus15 no. UMO-2018/29/B/ST4/00335)".

Abstract

Endothelial cells (ECs) line the lumen of all the blood vessels from the heart to the extremities in the configuration of a continuous monolayer. ECs have several regulatory functions towards maintaining cardiovascular homeostasis. With their multiple autocrine, paracrine and endocrine roles, the vascular endothelium is regarded as a unique organ that carries out vital tasks to regulate vascular tone and blood flow, vascular permeability, the proliferation of smooth muscle cells, immune and inflammatory responses, thrombosis, and angiogenesis. Failure of ECs to perform any of their basal regulatory functions characterizes endothelial dysfunction (ED). ED is interconnected with the development and progression of many diseases, especially cardiovascular diseases such as atherosclerosis, hypertension and stroke, as well as diabetes and insulin resistance, chronic kidney failure, liver diseases, cancer and severe infectious diseases such as COVID-19. Therefore, studying endothelial phenotype, especially at the ECs subcellular level could provide valuable information on cardiovascular health and diseases. Imaging of ECs' cellular organelles and studying the underlying mechanisms associated with ED and disease development hold great potential to improve our understanding of disease progression, enhance diagnosis and prognosis and assess new therapeutic solutions.

Spectroscopic imaging, using multiple microscopy techniques in a complementary fashion, to study models of ED at the subcellular level, and the development of novel approaches to image ECs and investigate alterations in cellular processes could shed the light on cellular mechanisms associated with disease development aiding in narrowing the bench to bedside gap in endothelial diagnosis and treatment. With fluorescence microscopy being considered a standard technique to investigate ECs and the development of ED, Raman imaging is regarded as a strong technique to study ECs organelles and biochemical alterations at the subcellular level in a label-free fashion. Nevertheless, molecular Raman probes hold great potential of improving the sensitivity and selectivity of Raman microscopy techniques.

ECs prolonged activation and inflammation is one of the common causes of the development of ED and the advancement of cardiovascular diseases. Inflamed ECs express, among others, alterations in intracellular lipids content presented in lipid-rich cellular

organelles such as lipid droplets (LDs) and the endoplasmic reticulum (ER). Inflamed ECs also present increased expression of surface adhesion molecules such as ICAM-1. The phenotype of ED is also often associated with altered ECs proliferation and regeneration capacities limiting them from mending ED. Therefore, looking for markers underlying cellular processes such as changes in intracellular lipids distribution in inflamed ECs and studying altered ECs proliferative and regenerative capacities in *in vitro* and *ex vivo* models of ED is of great value.

The experimental work undertaken towards completion of the PhD thesis demonstrated novel labelled Raman imaging approaches to study changes in ECs lipidic substructures, especially LDs, ER and the nuclear envelope associated with ECs inflammation. Moreover, a novel labelled Raman imaging approach to assay ECs proliferation and regeneration in ECs and isolated aortae tissues. The presented novel approaches to study models of ED have been complemented with previously established methods such as label-free Raman imaging, fluorescence microscopy and transient absorption microscopy. Moreover, the presented molecular Raman probes have been assessed in ECs from various organs i.e. in ECs from the microvasculature (HMEC-1), the aorta (HAoEC), the heart (HCAEC) and the brain (HBEC-5i) addressing the heterogeneity of ECs that tend to have different properties depending on their respective vascular beds.

Astaxanthin (AXT) is a natural red pigment with established antioxidant and anti-inflammatory properties. AXT is shown to be highly lipophilic and tends to accumulate in lipids. Moreover, AXT exhibits a resonantly enhanced Raman spectrum when excited with a 532 laser. These properties motivated its consideration as a molecular Raman probe for lipidic structures in ECs. AXT demonstrated a time-dependent accumulation in lipid-rich cellular organelles in ECs i.e. LDs, ER and the nuclear envelope, it was detectable in the Raman spectra of cells after only 30 minutes of incubation. Furthermore, AXT allowed Raman imaging of subcellular lipidic structures in ECs using relatively low laser power compared to label-free detection (3 mW instead of 30 mW), highlighting its applicability to visualize lipids in fragile samples which could be affected by high laser power such as live ECs. The presented AXT-labelled Raman imaging approach allowed visualizing the nuclear envelope in ECs, which is not possible to visualize using label-free Raman imaging.

AXT was assessed as a molecular Raman probe for lipids in ECs from various origins. It proved to be taken up similarly by different ECs and accumulated in ECs' lipidic organelles, thus being considered a universal Raman probe for visualizing LDs, ER and the nuclear envelope in ECs despite their heterogeneity. ECs intracellular lipids distribution shows distinct alterations when ECs are subjected to proinflammatory treatment such as with the proinflammatory cytokine TNF- α . AXT allowed visualizing changes in lipids distribution associated with inflammation of ECs, with AXT-labelled Raman imaging allowing visualizing lipids using relatively low laser power and providing information on the morphology of the nuclear envelope, and label-free Raman imaging allowing the detection of biochemical changes in lipids compositions associated with inflammation such as increased lipids unsaturation in LDs of ECs.

Raman and fluorescence microscopies revealed that AXT uptake into ECs could be improved through encapsulating AXT in neutral liposomes or positively charged lipoplexes. Furthermore, the anti-inflammatory effects of AXT on inflamed ECs could also be improved through encapsulation. Free AXT exhibited an anti-inflammatory role by decreasing the expression of ICAM-1, however, in its free form AXT did not cause significant changes to lipids distribution. When AXT-loaded liposomes or lipoplexes were used, both the overexpression of ICAM-1 and the number of LDs in inflamed ECs were reduced significantly.

5-ethynyl-2'-deoxyuridine (EdU) is a thymidine analogue with an alkyne tag that gets incorporated into newly synthesized DNA. EdU has gained a lot of popularity as a probe for cell proliferation due to its advantages of not relying on antibodies or requiring DNA denaturation. It could be fluorescently labelled *via* a copper-catalysed cycloaddition reaction "click chemistry" with a fluorescent azide. Due to the cytotoxic effects that copper compounds exert on cells and the weak permeability of most azide dyes, EdU fluorescence detection usually requires sample fixation and permeabilization. On the other hand, Raman detection of EdU is possible to be carried out in a "click-free" manner due to the alkyne tag of EdU exhibiting a Raman band in the spectroscopically silent region, where there are no possible overlapping with Raman bands from other biological compounds, at ca. 2122 cm^{-1} . Therefore, Raman identification of EdU could be achieved in live ECs without the need

for any additional dyes bypassing the undesirable effects of cell fixation and permeabilization.

Raman imaging of EdU-labelled ECs nuclei was possible following ECs incubation with EdU for 3h. Improved imaging of ECs nuclei, based on the detection of the EdU Raman band in the silent region compared to label-free Raman imaging of nuclei based on the DNA Raman band at ca. 788 cm^{-1} , were obtained when cells were subjected to EdU treatment for 24h. EdU labelling improved Raman imaging of nuclei of ECs from various sources. Moreover, live ECs imaging of EdU-labelled cells was achieved presenting its advantage over the methods that rely on “click chemistry”.

A novel approach to assay ECs proliferation based on the Raman detection of EdU-labelled ECs was presented. Raman detection of EdU was sensitive to changes in ECs introduced by cell treatment with two antiproliferative drugs. ECs pre-treated with cycloheximide (CHX) or doxorubicin (DOX) were used as *in vitro* models of impaired DNA synthesis and inhibited cell proliferation. EdU-labelling allowed the detection of these effects on ECs, presented in a decrease in the EdU marker Raman band and a significant decline in the number of proliferating (EdU-positive) cells. Fluorescence imaging of EdU-labelled ECs, dyed with Alexa fluor® azide dyes, in similar conditions confirmed the presented Raman imaging-based approach. Moreover, this approach was applied to study ECs regeneration *ex vivo* after induced mechanical injury in isolated murine aortae. ECs and smooth muscle cells (SMC) were shown to regenerate in aortic rings when they were incubated *ex vivo* in the presence of vascular endothelial growth factor (VEGF). Detecting changes in the regenerative capacity of ECs in *in vitro* and *ex vivo* models of ED was possible via EdU-labelling, a feature not possible to study using label-free Raman imaging techniques.

The spectroscopic molecular probes presented here to study alterations in ECs lipid-rich organelles and ECs regenerative capacities associated with the phenotypes of ED, complemented with established techniques such as label-free Raman imaging and fluorescence microscopy revealed the potential of spectroscopic imaging in *in vitro* and *ex vivo* models of ED to acquire comprehensive qualitative and quantitative information on the distribution and biochemical changes underlying ED. This could open the door for the development of new methods assessing ECs pathology development, improving diagnosis

and therapeutics potential and narrowing the bench to bedside gap in endothelial diagnosis and treatment.

Table of contents

Acknowledgements	II
Abstract	IV
Table of contents	IX
Abbreviations	XII
List of Tables	XV
List of Figures	XVI
1. Objectives of the thesis	22
Introduction Section	23
2. Endothelial cells	24
2.1. Endothelial cells' functions and their mechanisms	26
3. Endothelial dysfunction	31
3.1. Endothelial dysfunction involvement in disease development	31
4. Endothelial dysfunction at the subcellular level	34
4.1. Nucleus	34
4.2. Mitochondria	35
4.3. Endoplasmic reticulum	36
4.4. Lipid droplets	36
4.5. Lysosomes	37
5. Current methods to study endothelial dysfunction	38
5.1. Molecular markers of endothelial inflammation and endothelial dysfunction	38
5.2. <i>In vitro</i> , <i>in vivo</i> and <i>ex vivo</i> models of endothelial pathology	41
6. Spectroscopic imaging techniques to study endothelial cells	43
6.1. Fluorescence microscopy	43
6.2. Transient absorption microscopy	45
7. Raman Spectroscopy	47
7.1. Confocal Raman imaging	47
7.1.1. Label-free Raman imaging of cellular organelles	49
8. Molecular Raman probes	51
8.1. Concept, advantages and limitations	51
8.2. Label-free vs labelled Raman imaging of cellular organelles	54

8.2.1.	Nucleus.....	55
8.2.2.	Mitochondria.....	57
8.2.3.	Lipid droplets	57
8.2.4.	Lysosomes.....	58
Experimental Section		60
9.	Introduction to the experimental section.....	61
9.1.	A novel approach to image lipids in endothelial cells based on astaxanthin labelling ..	61
9.2.	Assessment of astaxanthin as a Raman probe for endothelial cells lipids, addressing cells heterogeneity.	62
9.3.	Studying the endothelial cells' uptake of astaxanthin in free and encapsulated forms ..	62
9.4.	A novel approach to assay endothelial cells' proliferation and regeneration in <i>in vitro</i> and <i>ex vivo</i> conditions	63
10.	Imaging lipids in endothelial cells based on astaxanthin labelling	66
10.1.	Objectives of the study.....	66
10.2.	Materials and methods	66
10.3.	Results and discussion	68
10.3.1.	Astaxanthin localization in endothelial cell lipid-rich organelles	68
10.3.2.	Live-cell imaging, the advantage of using low laser power	73
10.3.3.	Visualizing the nuclear envelope	74
10.3.4.	Astaxanthin as an anti-inflammatory agent.....	76
10.4.	Conclusions.....	77
11.	Astaxanthin as a Raman probe for lipids in endothelial cells of different origins.	79
11.1.	Objectives of the study.....	79
11.2.	Materials and methods	80
11.3.	Results and discussion	81
11.3.1.	Label-free vs astaxanthin-labelled Raman imaging of endothelial cell lipids.....	81
11.3.2.	Astaxanthin visualizing lipids in endothelial cells of different vascular beds	84
11.3.3.	Does astaxanthin exist in isolated or aggregated form in cellular lipids? Complementary information from transient absorption microscopy	85
11.4.	Conclusions.....	87
12.	Astaxanthin uptake by endothelial cells in free and encapsulated conditions	89
12.1.	Objectives of this study	89
12.2.	Materials and methods	90
12.3.	Results and discussion	92

12.3.1.	Astaxanthin-loaded liposomes characterized by Raman spectroscopy	92
12.3.2.	Time-dependent uptake of astaxanthin and astaxanthin-loaded liposomes by endothelial cells.....	94
12.3.3.	Effects of liposomal encapsulation on astaxanthin anti-inflammatory activity in endothelial cells.....	95
12.4.	Conclusions	98
13.	Imaging endothelial cell proliferation and regeneration: a novel approach based on Raman imaging	99
13.1.	Objectives of the study.....	99
13.2.	Materials and methods	100
13.3.	Results and discussion	104
13.3.1.	EdU-labelled Raman imaging of endothelial cell DNA.....	104
13.3.2.	Live cell imaging, the advantage of the Raman imaging approach	105
13.3.3.	Endothelial cell proliferation assay based on Raman imaging, and fluorescence imaging as a reference method.....	107
13.3.4.	EdU labelled Raman-based detection of doxorubicin effects on endothelial cells	111
13.3.5.	<i>Ex vivo</i> imaging of endothelial cells and smooth muscle cells regeneration in the isolated murine aorta.....	113
13.4.	Conclusions.....	115
14.	Summary and final conclusions	117
15.	Limitations	120
16.	Future directions	122
16.1.	Non-linear Raman imaging techniques.....	122
16.2.	Development of novel Raman probes for click chemistry applications.....	123
16.2.1.	Resonance Raman enhancement	124
16.2.2.	Enhancement of the Raman band in the silent region.....	126
16.3.	Multiplex Raman imaging	128
	List of Publications	129
	List of secondments and internships	131
	References	132

Abbreviations

EC, ECs:	“endothelial cell”, “endothelial cells”
ED:	“endothelial dysfunction”
AXT:	“astaxanthin”
EdU:	“5-ethynyl-2'-deoxyuridine”
SMC:	“smooth muscle cells”
BBB:	“blood-brain barrier”
eNOS:	“endothelial nitric oxide synthase”
RAS:	“renin-angiotensin system”
ACE:	“angiotensin-converting enzyme”
ARBs:	“angiotensin II receptor blockers”
VEGF:	“vascular endothelial growth factor”
ICAM-1:	“intercellular adhesion molecule 1”
VCAM-1:	“vascular cell-adhesion molecule 1”
TNF-α:	“tumour necrosis factor-alpha”
IL-6:	“interleukin 6”
NF-κB:	“nuclear factor kappa-light-chain-enhancer of activated B cells”
ROS:	“reactive oxygen species”
ER:	“endoplasmic reticulum”
UPR:	“unfolded protein response”
LDs:	“lipid droplets”
oxLDL:	“oxidized low-density lipoprotein”

COX-2:	“cyclooxygenase-2”
ECM:	“extracellular matrix”
CRP:	“C-reactive protein”
LOX-1:	“low-density lipoprotein receptor-1”
HUVEC:	“human umbilical vein endothelial cells”
HMEC-1:	“human microvascular endothelial cells”
HAoEC:	“human aortic endothelial cells”
HBEC-5i:	“human cerebral microvascular endothelial cell”
HCAEC:	“human coronary artery endothelial cells”
HCECs:	“human corneal epithelial cells”
LPS:	“lipopolysaccharides”
IR:	“Infrared”
BODIPY:	“boron dipyrromethene”
TA:	“transient absorption”
UV:	“ultraviolet”
NIR:	“near-infrared”
CCD:	“charged-coupled device”
DLS:	“dynamic light scattering”
FasL:	“Fas ligand”
CuAAC:	“copper(I)-catalyzed azide–alkyne [3 + 2] cycloaddition”
EU:	“5-ethynyl uridine”
TPP⁺:	“triphenylphosphonium cation”
BADY:	“bis(aryl)butadiyne”

AITQs:	“analogues of coenzyme Q”
CHX:	“cycloheximide”
DOX:	“doxorubicin”
FBS:	“foetal bovine serum”
EGF:	“epidermal growth factor”
CA:	“cluster analysis”
KMCA:	“k-means cluster analysis”
SD:	“standard deviations”
DPPC:	“1,2-dipalmitoyl-sn-glycero-3-phosphocholine”
DOPE:	“1,2-dioleoyl-sn-glycero-3-phosphoethanolamine”
DOTAP:	“1,2-dioleoyl-3-trimethylammonium-propane”
LUVs:	“large unilamellar vesicles”
CD-31 (PECAM-1):	“platelet/endothelial cell adhesion molecule-1”
SRS:	“stimulated Raman scattering”
CARS:	“coherent anti-stokes Raman scattering”

List of Tables

Table 5.1. Selected markers of endothelial inflammation, dysfunction and cardiovascular risk. The table is reproduced from Ref. [66], covered by CC BY 4.0 license allowing free sharing and adapting.40

Table 8.1. Summary of Raman probes. The table represents the names of Raman probes, the chemical structures of their targeting and Raman reporting moieties, their subcellular targets, their characteristic Raman bands positions, and the references where they were studied. ER: endoplasmic reticulum. The table is reproduced from Ref. [10], covered by CC BY 4.0 license allowing free sharing and adapting.53

List of Figures

- Figure 2.1. Structure of arteries and veins.** The figure is adapted from Ref. [21] after receiving the required permissions.25
- Figure 2.2. Summary of endothelial cell functions.**.....30
- Figure 7.1. Basic setup of a Raman microscope.** The figure is adapted from Ref. [37], covered by CC BY 3.0 license allowing free sharing and adapting.48
- Figure 8.1. Label-free Raman imaging biomolecules.** In the middle: a bright field image of a fixed HMEC-1, scale bar equals 10 μm , surrounded by pseudo-colour intensity images (scale bars equal 4 μm) showing the distribution of all organic compounds, lipids, proteins and nucleic acids, constructed by the integration of the Raman spectra at 2800-3030 cm^{-1} , 2830-2900 cm^{-1} , 996-1016 cm^{-1} and 770-810 cm^{-1} , respectively. 55
- Figure 8.2 Labelled Raman subcellular imaging.** (A) Labelled Raman imaging of mitochondria using the Raman probes MitoBADY, ALTQ2 and Mito-Azo (left) compared to label-free Raman imaging of cytochrome c (right) in live HeLa cells ^{108,110,111}. (B) Structures of EU-¹³C₂, EdU-¹³C, and 17-ODYA above their corresponding SRS images in live HeLa cells, showing the distributions of RNA, DNA and fatty acids, respectively ¹¹⁶. (C) SRS imaging of lysosomes (P2), mitochondria (P3) and nucleus (p4) based on targeting corresponding PDDA probes overlaid with lipids distribution (2850 cm^{-1}) ¹¹³. Scale bars equal 10 μm . The figure is reproduced from Ref. [3], covered by CC BY 4.0 license allowing free sharing and adapting.59
- Figure 9.1. Fluorescence “click chemistry” vs Raman “click free” detection of EdU.** (A) Basis of the fluorescence microscopy detection of EdU as EdU incorporates into DNA, then a “click chemistry” reaction is used to fluorescently label it. (B) A Raman spectrum of EdU (black) showing its alkyne (C \equiv C) Raman band in the cell spectroscopically silent region presented in an averaged cell spectrum (red).65
- Figure 8.1. Label-free Raman imaging biomolecules.** In the middle: a bright field image of a fixed HMEC-1, scale bar equals 10 μm , surrounded by pseudo-colour intensity images (scale bars equal 4 μm) showing the distribution of all organic compounds, lipids, proteins and nucleic acids, constructed by the integration of the Raman spectra at 2800-3030 cm^{-1} , 2830-2900 cm^{-1} , 996-1016 cm^{-1} and 770-810 cm^{-1} , respectively.55
- Figure 8.2 Labelled Raman subcellular imaging.** (A) Labelled Raman imaging of mitochondria using the Raman probes MitoBADY, ALTQ2 and Mito-Azo (left) compared to label-free Raman imaging of cytochrome c (right) in live HeLa cells ^{103,105,106}. (B) Structures of EU-¹³C₂, EdU-¹³C, and 17-ODYA above their corresponding SRS images in live HeLa cells, showing the distributions of RNA, DNA and fatty acids, respectively ¹¹¹.

(C) SRS imaging of lysosomes (P2), mitochondria (P3) and nucleus (p4) based on targeting corresponding PDDA probes overlaid with lipids distribution (2850 cm^{-1})¹⁰⁸. Scale bars equal $10\text{ }\mu\text{m}$. The figure is reproduced from Ref. [10], covered by CC BY 4.0 license allowing free sharing and adapting.59

Figure 10.1. Label-free and AXT-labelled Raman spectra of EC lipids. Structure of AXT above (A) Raman spectrum of a lipid droplet (LD) in an EC measured using high ($\sim 30\text{ mW}$) laser power. (B) Raman spectrum of an LD in an EC measured using low ($\sim 3\text{ mW}$) power. (C) Raman spectrum of an LD in an EC subjected to AXT treatment (for 6h) and measured using low laser power. (D) Raman spectrum of AXT solution in a non-polar solvent (castor oil). (E) Raman spectrum of AXT powder.70

Figure 10.2. Time-dependent AXT accumulation and AXT-labelled Raman imaging in healthy and inflamed HMEC-1. Raman visualization of the distribution of organic matter, lipids, and AXT using high and low laser power (approximately 30 mW and 3 mW , respectively). The integration of Raman spectra obtained from designated regions in the figure was used to image these compounds in both control and AXT-labelled HMEC-1 cells at different time points (30 min, 1h, 3h, and 6h). In addition, a group of cells were pre-incubated with TNF- α for 24h to induce inflammation (labelled inflamed).72

Figure 10.3. AXT shows colocalization with lipids in ECs. (A) Raman images of organic compounds ($3030\text{-}2830\text{ cm}^{-1}$) with the arrow indication the area from which the spectra in (G) were obtained. (B and C) Raman images of lipids ($2900\text{-}2830\text{ cm}^{-1}$) and AXT ($1545\text{-}1495\text{ cm}^{-1}$) were obtained using low (3 mW) laser power. (D and E) Raman images of lipids were obtained using high (30 mW) laser power. (F) merged image showing DNA ($800\text{-}775\text{ cm}^{-1}$, red) and AXT (blue) distributions. (G) extracted Raman spectra of an LD obtained using low and high laser power.73

Figure 10.4. AXT allows labelled live cell imaging with low laser power. Raman images of 5 different live HMEC-1 showing the distribution of AXT ($1545\text{-}1495\text{ cm}^{-1}$) obtained using low (3 mW) laser power. Cells were pre-incubated with TNF- α (24h), then treated with AXT for 6h.74

Figure 10.5. AXT allows visualizing the nuclear membrane of ECs, revealed by 3D Raman imaging. (A) Raman images showing intensity projection of AXT marker band at ca. 1520 cm^{-1} in the xy plane of an HMEC-1 pre-incubated with TNF- α (24h) and labelled with AXT (3h). (B) Imaging of the section indicated by the green line constructed from layers in the z-direction with $1\text{ }\mu\text{m}$ step size. (C) Characteristic AXT band at ca. 1520 cm^{-1} from AXT in DMSO and water (grey), LDs (red) and the nuclear envelope (blue).75

- Figure 10.6. AXT anti-inflammatory effect on HMEC-1, a fluorescence microscopy quantification of ICAM-1 expression.** ICAM-1 expression per cell in HMEC-1 presented as means \pm SEM for the groups: control (untreated), DMSO (cells incubated with the solvent used for AXT), TNF- α (24h), AXT (3h), and AXT treated groups before and after TNF- α incubation.77
- Figure 11.1. Label-free vs AXT-labelled Raman imaging of lipids in ECs.** Raman images of HAoEC with and without TNF- α pre-treatment (24h) and incubated with AXT for 0 (no AXT), 1, 3 or 6h, showing the distribution of organic matter, lipids, unsaturated lipids or AXT by Raman spectral integration at the spectral regions mentioned in the figure.82
- Figure 11.2. Spectral profiling of different ECs in normal and inflamed conditions.** Raman spectra (presented as averaged spectra \pm SD) of HAoEC (red), HBEC-5i (blue) and HCAEC (grey) with the TNF- α treated inflamed cells spectra presented in the respective darker colour.83
- Figure 11.3. Assessment of AXT as a molecular Raman probe for lipids in ECs of various origins.** Raman images of normal (A) and inflamed (TNF- α -pre-treated) cells (B) of HAoEC, HBEC-5i and HCAEC visualizing the distribution of organic matter ($3030\text{-}2800\text{ cm}^{-1}$), lipids ($2900\text{-}2830\text{ cm}^{-1}$) and AXT ($1535\text{-}1502\text{ cm}^{-1}$). Scale bars indicated at each image equal $5\text{ }\mu\text{m}$85
- Figure 11.4. Transient absorption microscopy revealed that AXT does not aggregate in cells lipids.** (A) Transient absorption spectra of AXT in DMSO (pump wavelength = 510 nm) at the delay times of (0.2, 1.0, 5.0, 8.0 and 15 ps) with the spectrum of filled and scale-inverted steady-state absorption referencing ground-state bleaching. (B) Phase image and transient absorption microscope image (pump and probe wavelengths = 470 and 625 , respectively) of an MCF7 cell. (C) The kinetic traces of AXT in solvent (DMSO), fixed and live cells with the insert showing the spectra from the first and second runs of the experiment. The figure is adapted from Ref. [¹⁶¹] with the permission of the Royal Society of Chemistry.86
- Figure 12.1. Characterization of astaxanthin-loaded liposomes** (A) Structure and Raman spectra of AXT powder (red) and in DPPC liposomes (blue). (B) Absorption and emission spectra of AXT in CH_3Cl . (C) Dynamic light scattering (DLS) results of Astaxanthin-loaded liposomes (100 nm).93
- Figure 12.2. ECs uptake of AXT-loaded liposomes studied by Raman imaging.** Representative images of HAoEC, control and cells incubated with AXT, AXT-loaded liposomes or lipoplexes (for 30 minutes, 1, 3 and 24 hours) constructed by integrating the Raman bands in the following spectral regions: $3030\text{-}2800\text{ cm}^{-1}$ (C-H stretching), $2900\text{-}2830\text{ cm}^{-1}$ (lipids), and $1535\text{-}1502\text{ cm}^{-1}$ (AXT). Raman imaging was carried out once with low laser power (3 mW) to detect AXT Raman bands and once with high laser power (30 mW) to detect bands associated with lipids. Scale bars indicated on the first image of each group ($3\text{-}4\text{ }\mu\text{m}$).94

Figure 12.3. The effects of free and encapsulated AXT on activated ECs lipids, studied by Raman imaging. (A) Raman images of HAoEC, other than the control group, all the presented groups were pre-incubated with TNF- α for 24h and then incubated with AXT, AXT-loaded liposomes or lipoplexes (for 1, 3 or 24h). Pseudocolour images constructed based on the relative intensities of the Raman bands at: 2800-3030 cm^{-1} (C-H stretching), 2830-2900 cm^{-1} (lipids), 3000- 3030 cm^{-1} (unsaturated lipids) and 1502-1535 cm^{-1} (AXT). Imaging was carried out once with low laser power (3 mW) to detect AXT Raman bands and once with high laser power (30 mW) to detect bands associated with lipids. Scale bar indicated on the first image of each group (equals 4 μm). (B) Averaged Raman spectra of the lipids cluster of the control (grey), TNF- α pre-treated group (black), TNF- α pre-treated then incubated with AXT (red), AXT-loaded liposomes (blue) and lipoplexes (purple). n = 6 cells in each group, 3 independent experiments were performed.....96

Figure 12.4. Fluorescence-based quantification of free and encapsulated AXT anti-inflammatory effects. (A) ICAM-1 expression, and (B) lipid droplets (LDs) per cell; of control, and TNF- α pre-treated groups that were later treated with AXT, AXT-loaded liposomes or AXT-loaded lipoplexes. The bars and whiskers represent means + SD from 3 independent experiments, * P < 0.05, ** P < 0.01 and *** P < 0.001. (C) Representative fluorescence images of HAoEC, visualizing nuclei (Hoechst stained, blue), lipids (BODIPY stained, green) and ICAM-1 (red). Scale bars equal 50 μm . ..97

Figure 13.1. The method used for studying ex vivo regeneration of ECs...... 102

Figure 13.2. EdU-labelling improves Raman imaging of nuclei in ECs of different origins. (A) EdU's chemical structure and Raman spectrum of the pure compound. (B) Raman images of HMEC-1, HAoEC and HCAEC showing the distribution of organic matter (3030-2800 cm^{-1}), nuclei acids (810-770 cm^{-1}) and EdU (2132-2112 cm^{-1}) in ECs labelled with EdU for 0, 3 or 24h..... 105

Figure 13.3. Raman-based EdU imaging could be done in live ECs. (A) Live HMEC-1 images with and without EdU labelling, showing the distribution of all organic matter, nucleic acids, EdU and cytochrome c by the integration of the Raman spectra at the respective spectral regions presented in the figure. (B) Averaged Raman spectra of the nucleus of EdU-labelled (red) and control cell (grey) showing the alkyne band at 2122 cm^{-1} 106

Figure 13.4. CHX pre-treatment effects on HMEC-1 studied by EdU-labelled Raman imaging (A) Raman imaging of HMEC-1 tagged with EdU that either did not receive (control) or received CHX pre-treatment at lower (1 $\mu\text{g}/\text{ml}$) and higher (10 $\mu\text{g}/\text{ml}$) concentrations, showing the distribution of all organic matter, nucleic acids, and EdU. (B) averaged spectra of the HMEC-1 nuclei class from each group. Inserts showing the DNA band at 788 cm^{-1} and the EdU band at 2122 cm^{-1} 108

Figure 13.5. Raman imaging-based ECs proliferation assay based on EdU sensing. (A) Raman imaging of HMEC-1 labelled with EdU, that received CHX pre-treatment at 0

(control), 1 or 10 $\mu\text{g/ml}$. The images show the distributions of organic matter (blue), nucleic acids (green), EdU (red) and a composite images (overlapped EdU and DNA signal in yellow), Scale bars = 30 μm . **(B)** EdU-positive cells (ECs expressing a band at ca. 2122 cm^{-1}) compared to all ECs (based on the label-free DNA band at ca. 788 cm^{-1}) shown as percentages (means \pm SD) obtained in 3 independent experiments, $n=50$ cells per group. ** $P < 0.01$ vs. control..... 109

Figure 13.6. Fluorescence imaging of EdU confirms the Raman imaging results. **(A)** Fluorescence images showing EdU-positive HMEC-1 nuclei (green), all cell nuclei based on Hoechst staining (blue), and composite images of EdU-labelled cells that received CHX pre-treatment at 0 (control), 1 or 10 $\mu\text{g/ml}$. Scale bars = 100 μm **(B)** EdU-positive ECs percentage. **(C)** Averaged fluorescence signal intensity from Alexa fluor® 488-stained EdU. Results are presented as means \pm SD, experiments were repeated 3 times, * $P < 0.05$, ** $P < 0.01$ vs. control..... 111

Figure 13.7. EdU-labelled Raman imaging is sensitive to Doxorubicin-induced effects on ECs. **(A)** Raman spectrum of DOX and its chemical structure. **(B)** Averaged area of the HMEC-1 nuclei in different conditions, presented as means \pm SD * $P < 0.05$ vs. control. **(C)** EdU-positive HMEC-1 percentage. **(D)** Raman imaging of EdU-labelled control and DOX pre-treated (0.1 and 1 μM , 24h) HMEC-1 showing the distribution of organic matter, nucleic acids, EdU, and DOX (presented by an elevated spectral background in the range of $4200 - 3800\text{ cm}^{-1}$). Scale bars = 5 μm 113

Figure 13.8. ECs regeneration in intact and injured en face murine aorta studied by Raman and fluorescence microscopies. **(A)** Fluorescence microscopy of isolated mice aortae samples with intact (control) or injured endothelium, with or without the supplementation of VEGF. Images show staining against CD31 marker for ECs (red), Hoechst (blue) and EdU (yellow). **(B)** Raman images of EdU-labelled en face aorta demonstrating the distributions of organic matter, elastin, nucleic acids and EdU (spectral regions indicated in the figure). The averaged spectra of two cells exhibiting EdU bands is shown below. 115

Figure 16.1. “Click chemistry” for Raman detection. The concept of Raman microscopy detection of EdU as EdU incorporates into DNA, then an CuAAC reaction “click chemistry” is used to enhance EdU signal. 125

Figure 16.2. The “click chemistry” reaction between EdU and the azide Raman reporter, with the spectra of the azide reporter (yellow), and EdU (red) on the right side compared the relative intensity of their respective characteristic bands. On the left side, the Raman spectrum of the end product (EdU-A1)..... 125

Figure 16.3. Synthesis of a potential azide Raman probe. **(A)** The synthesis scheme of the azide Raman probe. **(B)** NMR spectrum of the final product. 126

Figure 16.4. Enhancement of the Raman signal using a potential click chemistry Raman probe. **(A)** Structure of the synthesis final product and EdU. Raman spectra of

the product (blue) and EdU (black) in solid state (**B**) and dissolved in DMSO (10 mM, **C**). 127

Figure 16.5. Multiplex labelled Raman imaging of cell organelles. HMEC-1 labelled with EdU, MitoBADY and falcarinol to image the nucleus, mitochondria and ER, respectively, showing their composite image and the distribution of all organic matter for reference. On the right side cropped Raman spectra of the nucleus (red) showing EdU alkyne band, and of the cytoplasm (blue) showing the alkyne bands of MitoBADY and falcarinol. The figure was adopted from Ref. [¹⁵⁷], 128

1. Objectives of the thesis

The main objective of this thesis is the introduction of novel spectroscopic imaging methodologies to study ECs functionality and ED. The hypothesis is that based on the pre-established imaging techniques, the new approaches will provide complementary information on the functionality of ECs and the tissues containing them.

The particular objectives of this thesis are:

- Introducing a novel labelled Raman imaging-based method to study ECs subcellular lipidic structures relying on AXT as a new Raman probe for intracellular lipids.
- Establishing the properties of AXT as a lipids biomarker in ECs of various origins, and its excited state dynamics in live cells.
- Investigating the uptake and anti-inflammatory effects of free and encapsulated AXT in ECs using label-free and labelled Raman, and fluorescence imaging techniques.
- Introduction of a novel labelled Raman imaging-based approach to study ECs proliferation and *ex vivo* regeneration, complemented with fluorescence imaging.

Introduction Section

2. Endothelial cells

The vascular endothelium is the layer that coats the innermost walls of all of the body's blood vessels from arteries and veins to capillaries ¹. Arteries are tasked with nourishing organs with oxygenated blood and nutrients pumped from the heart. They contain elastin and smooth muscle cells (SMC) that help them accommodate the high pressure under which they constantly are. When arteries reach certain organs, they branch into smaller vessels further branching into arterioles ². Arterioles lack the elasticity of the arteries and are composed mainly of SMC. They deliver blood to the organs and play a vital role in vascular resistance. Capillaries are the narrowest blood vessels that consist of a single layer of ECs and exchange nutrients and metabolites with the tissues of the body through diffusion ³. The blood travels from the capillaries into venules that also play a role in oxygen and nutrient exchange in organs. The blood then flows into veins which consist of the same layers as the arteries but are thinner and less elastic. Some veins have one-way valves allowing the blood to flow in the direction of the heart ².

The most significant role of the vasculature is the transfer of nutrients and oxygenated blood to the tissues of the body and the transfer of the waste and deoxygenated blood back to the heart and then the lungs where the blood is oxygenated again. Gas and nutrients exchange occurs mostly in the capillaries, regulated by the vascular endothelium ³.

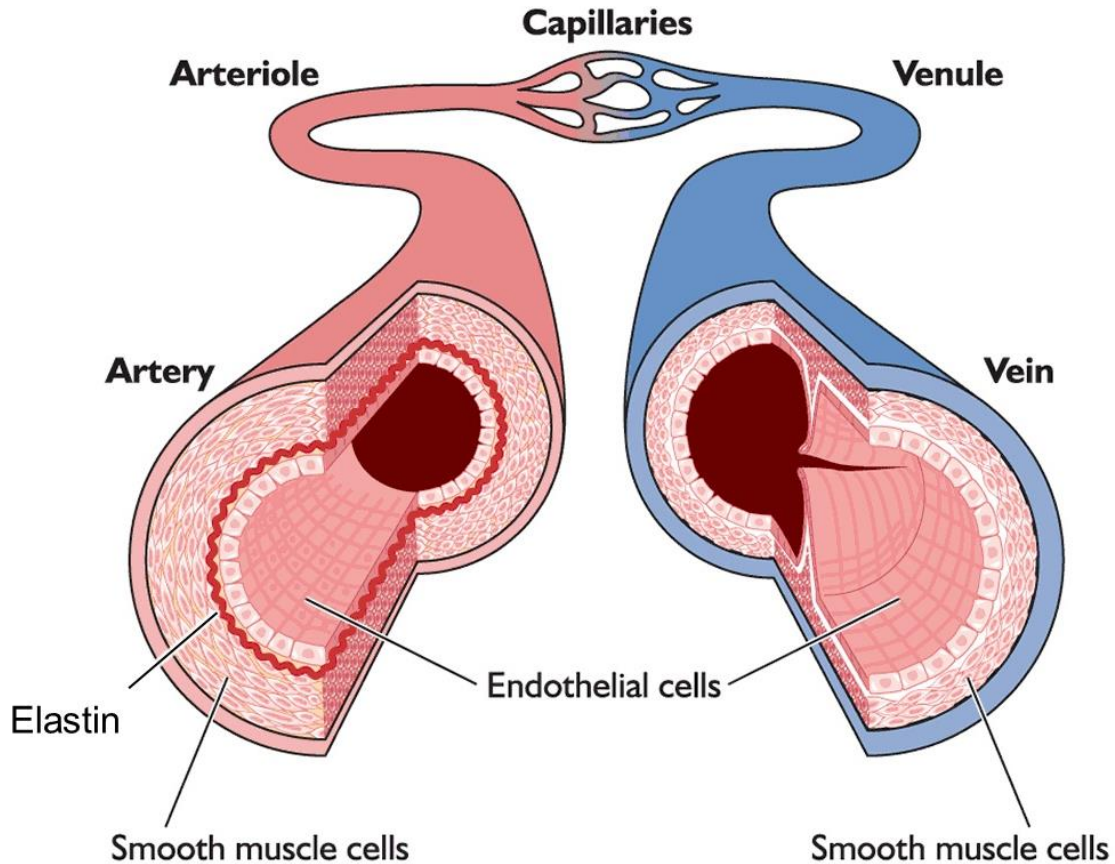


Figure 2.1. Structure of arteries and veins. The figure is adapted from Ref. [4] after receiving the required permissions.

The vascular endothelium is constituted by a monolayer of ECs that line the lumen of blood vessels while being anchored to the basal lamina (BL) ³. Nothing much was thought of ECs functions until the 1980s other than having selective permeability to control the passage of electrolytes and water. However, since the 1980s, major developments in cardiovascular research paved the way for a clearer view of the endothelium function and its regard as a large and special organ tasked with many endocrine, paracrine, and autocrine roles essential for maintaining cardiovascular homeostasis ⁵. ECs regulate vascular tone and the flow of the blood, vascular permeability, the proliferation of SMC, immune and inflammatory responses, thrombosis, and angiogenesis ^{1,5}.

2.1. Endothelial cells' functions and their mechanisms

The endothelium is a continuous monolayer of ECs connected to one another by different adhesive structures or junctions forming a semi-permeable barrier that controls the transport of various molecules between the blood and the tissues ⁵. ECs are tasked with supplying their surrounding tissue cells with their metabolic needs. For example, ECs express GLUT-1 and GLUT-4 managing the transport of glucose, which is a major source of energy in the body, to different organs ^{6,7}.

ECs barrier is maintained by endothelial cell-cell connections such as tight junctions, adherens junctions and adhesion molecules ⁸. Tight junctions regulate the paracellular transport of ions, water and some macromolecules while blocking the passage of large macromolecules across ECs. Adherens Junctions are formed by Cadherins, specifically VE-cadherin which is expressed only by ECs ⁹. Together with PECAM-1 (also known as CD31), VE-cadherin initiates contact among ECs and provides ECs with mechanical support essential for junction stability ^{8,9}.

Junctions between ECs vary in ECs with different vascular beds, allowing various levels of permeability in different organs. For instance, highly specialized ECs form the blood-brain barrier (BBB) connecting to one another through tight junctions maintaining highly selective semi-permeability and protecting the central nervous system from an array of pathogens and potentially harmful molecules ⁷.

One of the most important functions of ECs is the regulation of vascular tone. This function of ECs is done by a fine-tuned balance between endothelial mediator vasoconstrictive and vasodilative molecules ^{1,10}. Different physical and chemical stimuli such as shear stress, acetylcholine, bradykinin and thrombin cause ECs to produce and release mediators resulting in SMC relaxation ¹¹. Nitric oxide (NO) is among the well-studied endothelial-derived vasoactive substances. NO is a potent vasodilator with important involvement in regulating the vascular tone. NO is produced in ECs through an endothelial nitric oxide synthase (eNOS)-catalyzed oxidation of L-arginine in the existence of tetrahydrobiopterin (BH4) ^{12,13}. After its

release from ECs, NO diffuses to SMC inducing smooth muscle relaxation through cyclic guanosine monophosphate (cGMP) ^{12,13}.

Besides NO, other vasodilators participate in the endothelial regulation of vascular tone. Prostacyclin (PGI₂) is an endothelial-derived vasodilator that is synthesized by the cyclooxygenase-derived breakdown of arachidonic acid. PGI₂ induces SMC relaxation and vasodilation via Cyclic adenosine monophosphate (cAMP) ¹⁴. Another group of vasodilators generated by ECs is endothelium-derived hyperpolarizing factors (EDHFs). EDHFs are a collection of molecules with a common mechanism of inducing vasodilation by hyperpolarization of SMC through activation of K⁺ channels ^{11,12}.

Countering the actions of these vasodilators, there are endothelium-derived vasoconstricting factors such as endothelin-1, thromboxane A₂ (TXA₂), and angiotensin II ¹². Endothelin-1 is among the most potent known vasoconstrictor peptides. It is involved in the long-term management of arterial blood pressure ¹⁴. Produced and released mainly by ECs, endothelin-1 also contributes to vascular SMC proliferation ¹⁴. Endothelin-1 is also known to have proinflammatory effects, antagonizing NO and contributing to endothelial dysfunction ¹⁵. Another well-known vasoconstrictor is angiotensin II which is considered to carry out major effects within the renin-angiotensin system (RAS) ¹⁶. Angiotensin II is formed in ECs through the cleavage of angiotensin I by the angiotensin-converting enzyme (ACE). The RAS is known to be involved in the regulation of blood pressure, reabsorption of sodium and water, and secretion of potassium. However, RAS and angiotensin II in particular have been shown to induce inflammation and fibrosis ¹⁶. Several hypertension medications belonging to the ACE inhibitors or the angiotensin II receptor blockers (ARBs) group act directly on the RAS to counter its vasoconstrictive effects. A healthy endothelium maintains the balance of vasoactive molecules responding to different stimuli and regulating the vascular tone. Whereas in different endothelial pathologies, this balance is shown to be impaired ¹.

Angiogenesis is a complex and extremely important process that leads to the formation of new blood vessels from pre-existing ones. Angiogenesis involves ECs

migration, differentiation, and proliferation following stimulation by several pro-angiogenic agents such as vascular endothelial growth factor (VEGF), which was the first example of a growth factor specific for the endothelium ^{1,17}. In embryos, angiogenesis does not only aid the formation of blood vessels necessary to supply oxygen and nutrients, but also provides instructive trophic signals promoting the morphogenesis of organs ¹⁷. The processes of angiogenesis and endothelial cell proliferation in most blood vessels of healthy adults remain mostly quiescent with the exceptions of the cycling ovary and the placenta during pregnancy. However, in response to stimuli such as hypoxia, inflammation or physical injury endothelial cells can rapidly divide to allow healing and repair ¹⁸. Moreover, the phenotype of endothelial dysfunction has been linked to the inability of ECs to regenerate and heal vascular dysfunction due to an altered capacity of endothelial regeneration ¹⁹.

Hemostasis is a term used to describe a set of processes that controls blood clotting, platelet activation, and vascular repair towards cessation of bleeding. The hemostatic system is activated upon vascular injury starting a series of vascular and extravascular events aiming to seal the damage ²⁰. Thrombosis refers to the development of an occlusive clot in a blood vessel, restricting the blood flow and the delivery of oxygen and nutrients to certain tissues or organs ²⁰. Ensuring a proper balance between promoters and inhibitors of blood coagulation, maintaining hemostasis and preventing thrombosis are of great importance and are mainly regulated by ECs.

In normal physiological conditions, the luminal surface of ECs (the surface in contact with blood) provides a non-thrombogenic layer that prevents the attachment of cells and clotting proteins, maintaining blood fluidity ¹. Moreover, ECs are responsible for the secretion of different platelet inhibitors such as NO and prostacyclin preventing platelet aggregation and the expression of various anticoagulants such as thrombomodulin and endothelial cell protein C receptor (EPCR) preventing fibrin formation ²⁰⁻²². On the other hand, upon the development of endothelial dysfunction, ECs promote the formation of fibrin and platelet adhesion and aggregation, for example by the expression of von Willebrand factor (VWF). Lastly, ECs also play a

role in dissolving formed blood clots by releasing pro-fibrinolytic agents such as tissue plasminogen activator (tPA) ²⁰.

Inflammation develops as the body's response to injury or infection through increased permeability of ECs, vascular leakage and neutrophil activation. Inflammatory responses are designed to be life-preserving, acting towards removing pathogens and injurious agents along with infected or damaged cells ^{5,23,24}. After eliminating the cause of acute inflammation, pathogens and cellular debris along with apoptotic cells are removed by macrophages, proinflammatory cytokines are exhausted and anti-inflammatory responses are induced. If these processes are not carried out properly, it may lead to prolonged and chronic inflammation and pathologies ⁵. ECs and leucocytes are the main cell types involved in the inflammatory response.

In normal physiological conditions, ECs maintain their barrier function, control vascular permeability and do not promote leucocyte adhesion. In the non-inflammatory state, ECs suppress the expression of adhesion molecules such as intercellular adhesion molecule 1 (ICAM-1), vascular cell-adhesion molecule 1 (VCAM-1) and E-selectin ²⁴. Different stimuli including turbulent flow or proinflammatory cytokines such as tumour necrosis factor-alpha (TNF- α) and Interleukin 6 (IL-6) induce endothelial cell activation, thus inducing expression of adhesion molecules (ICAM, VCAM and E-selectin) which causes the recruitment of circulating leucocytes ²⁵. Moreover, as ECs play a major role in the inflammatory response after activation, ECs are also very important players in the resolution of the inflammatory response through highly coordinated complex mechanisms due to their ability to release various anti-inflammatory mediators ²³.

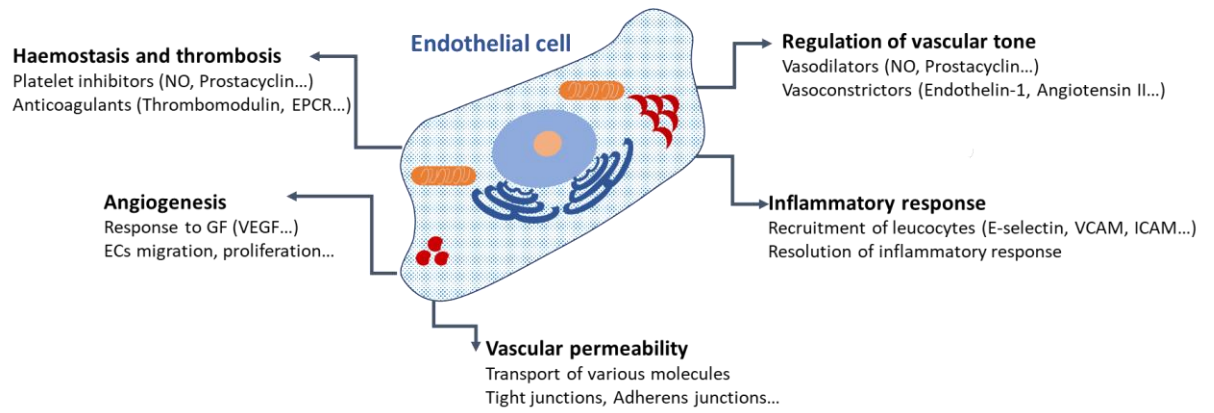


Figure 2.2. Summary of endothelial cell functions.

3. Endothelial dysfunction

Endothelial cell dysfunction (endothelial dysfunction, ED) is characterized by the failure of ECs to carry out any of their basal functions, namely regulating the vascular tone and the blood flow, maintaining blood fluidity, regulating the vascular permeability, the proliferation of SMC, controlling immune and inflammatory responses, thrombosis and thrombolysis, and angiogenesis^{10,24}. Consequently, ECs' actions shift to a vasoconstrictive phenotype with elevated permeability, proinflammatory response and prothrombic properties¹. There are various mechanisms underlying the progression of ECs into an ED state. However, vascular inflammation, oxidative stress and reduced NO bioavailability are often considered the major players in the development of ED in various pathologies.

There are various risk factors that may lead to the progression of ED, including pathological conditions such as diabetes mellitus, hypertension and hyperlipidaemia, chronic inflammatory diseases including rheumatoid arthritis and psoriasis, and other risk factors such as smoking, extended exposure to noise and pollution and mental stress^{1,10}. With the increased understanding of endothelial physiology and pathophysiology, it became undoubtedly that the endothelial phenotype provides valuable information on cardiovascular health and diseases. Indeed, the progression of many diseases has been linked to ED, particularly there is a strong connection between ED and the development of cardiovascular diseases such as atherosclerosis, hypertension and stroke. Moreover, ED has been linked to diabetes and insulin resistance, chronic kidney failure, liver diseases, cancer and severe infectious diseases such as COVID-19^{1,10,26-30}.

3.1. Endothelial dysfunction involvement in disease development

As mentioned earlier, ED has a strong connection with the development of cardiovascular diseases. Moreover, the state of vascular endothelium and ED could be considered a true barometer for cardiovascular pathogenesis¹⁰. Cardiovascular incidences are of great significance due to the fact that cardiovascular diseases reside

at the top of global causes of death, with myocardial infarctions (commonly known as heart attacks) and strokes responsible for the vast majority of deaths. This is especially apparent in low-income countries where access to routine healthcare solutions is not as widespread compared to developed countries ³¹.

ED is shown to be both a cause and a consequence of cardiovascular diseases, contributing to the initiation and progression of cardiovascular pathogenesis. For instance, in the case of hypertension, characteristic findings include lowered production, ineffectiveness or decreased bioavailability of endothelial vasodilatory mediators (especially NO), paired with increased production or sensitivity to endothelial vasoconstriction mediators (such as endothelin-1) ^{1,15}. It is suggested that decreased bioavailability of NO in hypertension could be attributed to increased oxidative stress in the hypertensive state. For instance, increased levels of angiotensin II cause the generation of reactive oxygen species (ROS) by stimulating NADPH oxidase, eventually leading to vascular inflammation ³². Thus, it has been demonstrated that antihypertensive treatment using ACE inhibitors or ARBs causes improvement in endothelial functions, unlike antihypertensive treatment using beta blockers ³³.

ED is closely linked to atherosclerosis, particularly atherosclerosis is connected to the change of endothelial phenotype towards a proinflammatory and prothrombotic state. Several risk factors could lead to this state including smoking, hypertension, hyperlipidaemia and diabetes ³⁴. Endothelial NO production is inhibited, restricting its antiatherogenic role, while an elevated expression of endothelial-derived adhesion molecules (such as VCAM-1) and cytokines promote monocyte adhesion and penetration through ECs ³⁴. Furthermore, proinflammatory cytokines (such as TNF- α) released from monocytes induce growth factors production in ECs and SMC contributing more to atherogenesis ¹.

Despite over 5 decades of research on EC functions and ED, the popularity of which is still on the rise, there is still a significant bench-to-bedside gap in endothelial-targeted diagnosis, prognosis and therapy. This gap is the result of the difficulty of translating the huge amount of knowledge that has been accumulated over the years

into routine clinical practice ³⁵. It is particularly difficult due to the extreme complexity and heterogeneity of the vascular endothelium and the inapplicability of the current methods used to assess endothelial function or dysfunction in everyday clinical settings. However, on the plus side, there are numerous new studies focusing on a deeper understanding of the endothelium, introducing novel methods to study ED, and developing new therapeutics with the potential of improving endothelial health.

4. Endothelial dysfunction at the subcellular level

Cells are the building blocks of living organisms. Constituted by smaller organelles that have different characteristics and functions, and interact with the surrounding environment, they acquire and utilize energy, grow and reproduce, and eventually die. Abnormalities in the cellular and subcellular level and biochemical alterations are often the underlying cause of various pathologies. Investigating the composition of subcellular compartments and tracking the changes that occur at the subcellular level during various cellular processes such as pathology development, improves our understanding of the mechanisms by which various diseases develop, consequently, improving diagnosis and treatment^{36,37}.

Being considered a large and unique organ that runs along the circulatory system, the vascular endothelium is constituted of a single type of a continuous layer of cells; endothelial cells. Nevertheless, ECs are extremely complex and heterogenous allowing the endothelium to carry out an array of tasks suitable for each organ or tissue in the body. Failure of ECs to perform their vital functions opens the door to the development of endothelial dysfunction. ED usually starts at the subcellular level, initiated by changes and abnormalities in the biochemical processes of ECs^{10,36,37}.

4.1. Nucleus

Carrying the genetic materials (Cellular DNA) condensed in chromosomes and surrounded by a porous membrane (the nuclear envelope), ECs nuclei are where vital biological processes such as DNA replication, cell growth and division, and transcription take place. Various stimuli could trigger the activation of nuclear transcription, causing the expression of certain genes. In the case of endothelial inflammation, an increased expression of proinflammatory cytokines is observed. The proinflammatory cytokines activate different pathways including the “nuclear factor kappa-light-chain-enhancer of activated B cells” (NF- κ B), which consequently leads

to chromatin rearrangement, eventually activating ECs proinflammatory and prothrombotic phenotype and leading to apoptosis^{10,34,38}. Upon DNA damage, especially due to oxidative stress, cellular DNA damage response (DDR) is employed, involving the recruitment of different DNA repair factors such as Poly (ADP-ribose) polymerase (PARP) in order to repair the damage. Nevertheless, byproducts of DDR have been shown to initiate biomineralization leading the way to vascular calcification³⁸.

4.2. Mitochondria

Nicknamed “the powerhouse of the cell”, mitochondria are responsible for harnessing energy inside phosphate bonds producing adenosine triphosphate (ATP) during a process called oxidative phosphorylation. Despite the fact that ECs rely mainly on anaerobic glycolytic metabolism for energy production, ECs' mitochondrial functions exceed providing a source of energy for the cells. ECs mitochondria are tasked with handling cellular Ca^{2+} , vascular redox signalling and programmed cell death (apoptosis)³⁹⁻⁴¹.

Cellular reactive oxygen species (ROS) are known to originate mainly in the mitochondria possibly as byproducts of oxidative phosphorylation. In normal conditions, low levels of mitochondrial ROS are essential for vascular signalling³⁹. Mitochondrial ROS are known to signal ECs and SMC proliferation, vasodilation and apoptosis¹⁰. However, excess ROS is known to cause alterations and damage to the fundamental biomolecules (DNA, proteins and lipids). This ROS-caused damage is commonly known as oxidative stress. Excess ROS and oxidative stress cause mitochondrial DNA damage, reduced NO bioavailability and lipids peroxidation^{10,39-41}. Furthermore, elevated levels of mitochondrial ROS signal ECs apoptosis³⁹. As mentioned earlier, oxidative stress and inflammation are the underlying causes of ED development in many cases, explaining the involvement of the mitochondria in endothelial pathology. Changes in mitochondrial functions have been linked to

different endothelial pathologies such as hyperglycemia, diabetes mellitus, hypertension and atherosclerosis ⁴²⁻⁴⁶.

4.3. Endoplasmic reticulum

The endoplasmic reticulum (ER) is a large organelle that consists of a network of tubules stretching from the nuclear envelope to the cell membrane. The ER is involved in key cellular processes including lipid biosynthesis, protein folding and protein post-translational modifications. Within ECs, the ER is tasked with the regulation of different metabolic processes. Failure of the ER to carry out these regulatory functions is generally termed ER stress, which has been connected to the development of ED ^{12,47}.

One of the most important functions of the ER is the post-translational folding of proteins. This ER function is moderated by the unfolded protein response (UPR). UPR sustain an equilibrium between the ER folding capacity and its folding load by reducing protein translation, activating transcriptional processes that enhance the ER protein folding capacity and inducing degradation of irreparably misfolded proteins ^{12,48}. ER stress could develop as a consequence of UPR failure to sustain the equilibrium between the ER folding capacity and its folding load or as a result of chronically activated UPR. UPR could be activated by an array of effectors including oxidized low-density lipoprotein (oxLDL), free fatty acids, disturbed flow and angiotensin II ⁴⁹. ER stress leads to activation of the ECs' proinflammatory and vasoconstrictive phenotypes and increased ROS production, causing ED development and eventually leading to cell death ^{10,12,48,50}.

4.4. Lipid droplets

LDs are cellular organelles that are rich in lipids and have been known for their role as energy-storing entities. However, LDs have been later recognized for their involvement in important regulatory functions in the cells. In particular, LDs play

major roles in regulating the uptake, metabolism, distribution and utilization of lipids in ECs⁵¹. LDs' involvement in the progression of ED and their contributions to the development of various diseases such as atherosclerosis, obesity and metabolic syndrome was demonstrated⁵²⁻⁵⁴.

Upon ECs inflammation through the NF- κ B pathway, increased expression of endothelial adhesion molecules such as ICAM-1, VCAM-1 and cyclooxygenase-2 (COX-2) is observed. This is accompanied by changes in ECs' lipid content, leading to an increase in endothelial lipid droplets that contain lipids of unsaturated characteristics⁵⁵. Moreover, these abnormalities in ECs LDs content and characteristics have been recognized as a hallmark of inflammation and pathogenesis in ECs^{56,57}. Novel methods of imaging lipids and LDs within ECs both in their healthy and inflamed conditions represent a vital part of this thesis and its underlying studies.

4.5. Lysosomes

Lysosomes are digestive enzymes containing membrane-bound cellular organelles. They are involved in autophagy (self-eating) resulting in the clearance or recycling of damaged or worn-out cellular organelles and molecules such as proteins and lipids, contributing to cellular homeostasis. In ECs, lysosomes respond to different stimuli such as nutritional starvation, hypoxia, ROS, DNA damage and sheer stress, playing a cytoprotective role aiming at restoring the physiological balance in ECs⁵⁸⁻⁶⁰. However, when uncontrolled autophagy takes over, the role of lysosomes shifts from exerting cytoprotective properties to promoting the development of ED. Although the mechanisms by which autophagy could contribute to ED are not completely understood, the importance of the modulatory effects of lysosomal autophagy and the connection between altered autophagic flux and endothelial pathologies have been shown in multiple studies⁵⁸⁻⁶³.

5. Current methods to study endothelial dysfunction

ECs show extreme heterogeneity in different organs and tissues of the body as they tend to adapt to the surrounding microenvironment and other cell types. The term vascular niche describes these microenvironmental conditions and the interactions around blood vessels to which ECs are subjected. It has been shown that the vascular niche does not only contribute to the ECs heterogeneity but also to the development of ED via different mechanisms ⁶⁴. The vascular endothelium is also substantially complex. ECs participate in an array of processes and carry out multiple functions through various mechanisms, therefore, studying vascular endothelial dysfunction is not a straight forward task. Most studies conducted to investigate ED focus on a single to a few mechanisms of ED development ⁶⁵.

5.1. Molecular markers of endothelial inflammation and endothelial dysfunction

As is the case for ECs themselves being complex and heterogenous, and displaying different features, functions and mechanisms that vary depending on their vascular niche and their surrounding environment, markers of endothelial functions, endothelial activation, inflammation and dysfunction are heterogenous, showing differences in different organs and different vascular beds ⁶⁶. Being divided into circulating soluble biomarkers that could be detected in the blood and extracellular matrix (ECM) and cell component biomarkers that could be detected in the local tissue of interest, markers of endothelial inflammation and dysfunction could provide substantial information on the development and risk of cardiovascular diseases ⁶⁷. Different markers of ED have been identified and studied for their role in disease progression, while researchers are actively on the look for new markers and the quest for an improved understanding of the previously established ones. Key markers of ED are summarized in (Table 5.1).

During cardiovascular incidents, especially during atherogenesis, the process of atherosclerotic plaque formation, proinflammatory cytokines such as TNF- α or acute-

phase proteins such as C-reactive protein (CRP) induce the release of endothelial adhesion molecules (ICAM-1, VCAM-1, E-selectin and P-selectin) ^{66,67}. These endothelial adhesion molecules are produced by ECs in order to recruit circulating leukocytes in response to different stimuli. In the context of endothelial pathology progression, they contribute to atherogenesis and the progression of atherosclerotic lesions ⁶⁸. Elevated expressions of E-selectin and ICAM-1 were associated with the prevalence of coronary heart disease and atherosclerosis, suggesting that E-selectin and ICAM-1 could be utilized as markers for atherosclerosis and coronary heart disease in clinical settings ⁶⁹.

The production of CRP from the liver is shown to be induced as a reaction against inflammatory stimuli with the proinflammatory cytokine IL-6. Expressions of both IL-6 and CRP have been shown to increase during the progression of atherosclerosis ⁷⁰. Moreover, high-sensitivity C-reactive protein (hs-CRP) induced by IL-6 has been viewed as a robust clinical biomarker for cardiovascular diseases ⁷¹. Circulating microparticles are small vesicles ranging from 100 nm to 2 µm in diameter. They originate from endothelial or blood cells and play a role in vascular function and inflammatory response. Increased levels of circulating microparticles have been found in different cardiovascular diseases such as hypertension, diabetes and ischemic stroke ⁷². Furthermore, in patients with myocardial infarction and angina, elevated amounts of endothelial-derived microparticles were associated with increased levels of IL-6 and CRP supporting their potential as endothelial inflammation and cardiovascular risk markers ⁷³.

Other candidates derived from activated ECs have been regarded as biomarkers for ED and cardiometabolic diseases including hypertension and diabetes mellitus. On the top of this list, there are OxLDL, asymmetric dimethylarginine (ADMA) and endocan ⁶⁶. OxLDL is known as a marker of oxidative stress and has been studied for its effects on the development of ED ⁷⁴. OxLDL exerts its effects on ECs via Lectin-like oxidized low-density lipoprotein receptor-1 (LOX-1) triggering EC inflammation via CD40/CD40L signalling pathway ⁷⁵. AMDA is known to be an eNOS inhibitor, thus explaining its contribution to the development of ED as the inhibition of eNOS

results in lower levels of endothelial NO leading the way to ECs activation and to the disruption of endothelium-dependent vasodilation ⁷⁴. Endocan is an emerging immunoinflammatory marker that is released by ECs in different organs and plays a regulatory role in cell adhesion ⁷⁶. High levels of endocan have been linked to ED, and have been observed during different endothelium-related diseases such as hypertension and chronic kidney disease supporting its potential as a marker for ED and cardiovascular risk ^{76,77}.

Selected markers of ED and cardiovascular risk

Markers	Type	Main Source
ICAM-1	Intracellular adhesion molecule (immunoglobulin superfamily)	Activated ECs
VCAM-1	Vascular cell adhesion molecule (immunoglobulin superfamily)	Activated ECs
E-selectin	Cell adhesion molecule (selectin family)	Exclusively from activated ECs
P-selectin	Cell adhesion molecule (selectin family)	Weibel–Palade bodies (WPBs) of ECs
IL-6	Proinflammatory cytokine	Macrophages and monocytes
CRP	Acute-phase protein	Hepatocytes
Endothelial microparticles	Vesicles from ECs membrane	Endothelial and blood cell membranes
LOX-1	Receptor for oxLDL	ECs
CD40L	Member of the TNF superfamily	Activated T cells
ADMA	NOS inhibitor	Activated ECs
Endocan	Proteoglycan	Activated ECs

Table 5.1. Selected markers of endothelial inflammation, dysfunction and cardiovascular risk. The table is reproduced from Ref. [66], covered by CC BY 4.0 license allowing free sharing and adapting.

5.2. *In vitro*, *in vivo* and *ex vivo* models of endothelial pathology

Since they were first cultured in 1973, human umbilical vein endothelial cells (HUVEC) were and still are very popular in endothelium-related research ⁷⁸. Other endothelial cell lines macro and micro-vessels such as human aortic endothelial cells (HAoEC), human coronary artery endothelial cells (HCAEC), and human microvascular endothelial cells (HMEC-1) were developed and gained huge popularity in *in vitro* endothelium-related research settings ⁷⁹. Although being regarded as easier to perform, not requiring animal handling skills, and being less costly, *in vitro* studies of ECs functions and ED are criticized for not representing the natural environment. For instance, in EC culture, most culture media are supplemented with nutrients and growth factors in non-physiological concentrations to allow the proliferation and expansion of ECs, which is necessary for *in vitro* studies but could significantly affect the experimental results, especially in the case of studies on cell proliferation and angiogenesis ⁸⁰. Furthermore, ECs are known to be in close contact with the surrounding cells such as SMC and leucocytes. These interactions are rarely assessed in *in vitro* studies of ED.

In vivo research of the endothelium includes the use of animal models (most commonly rodents) of endothelial-derived pathologies ⁶⁵. There *in vivo* studies offer a possibility to assess different processes of ED that are closer to reality and are directly involved in the progression of certain disorders. However, they have the disadvantages of being demanding, expensive, and more difficult to assess. With the increased attention in the scientific community on animal rights and the three Rs principle (Standing for Replacement of animal models, Reduction of the number of experimental animals used, and Refinement of the welfare of experimental animals), approaches such as *in vitro* co-culture and *ex vivo* studies are on the rise.

On the other hand, *ex vivo* models of ED could present an alternative to *in vitro* and *in vivo* studies that represent the best of both worlds. *Ex vivo* studies of endothelial pathology rely on the isolation of the tissues or organs of interest from the experimental animal, and growing and testing the isolated tissues or organs in the

laboratory. Unlike EC culture, this type of experiment allows for the interactions between the vascular endothelium and the surrounding microenvironment as it contains different types of cells and maintains the tissue structure closer to the *in vivo* environment^{17,81,82}. Moreover, ex vivo studies comply with the three Rs principle allowing the use of fewer animals and omitting some of the harsh treatments used in animal models such as injection with Lipopolysaccharides (LPS) to induce endothelial damage.

6. Spectroscopic imaging techniques to study endothelial cells

There are several spectroscopic imaging techniques that could be applied to assess the state of ECs' health and disease. Some examples of spectroscopic imaging tools that are commonly used for studying ECs include confocal microscopy, which is a widely used imaging technique that uses a laser beam to focus on a single plane of the sample, producing high-resolution, three-dimensional images. This technique is useful for studying the structure and function of ECs, including their morphology and organization, and can also be used for tracking the movement of molecules within these cells ⁸³. Additionally, Infrared (IR) microscopy is another powerful spectroscopic imaging technique that can be used to study the composition of endothelial cells ⁸⁴. This technique is based on the measurement of the absorption of infrared light by molecules within the cell, which can provide information about the chemical composition and structure of the sample.

In the experimental work undertaken for the completion of this thesis, three powerful and reliable spectroscopic imaging techniques are used for subcellular imaging of ECs functionality and dysfunction in a complementary fashion, namely fluorescence microscopy, transient absorption microscopy and Raman microscopy (explained in more detail in the next chapter).

6.1. Fluorescence microscopy

Fluorescence microscopy is a powerful technique that allows for the visualization of biological specimens at high resolution with exceptional specificity. The method is based on the phenomenon of fluorescence, which happens when a molecule's electrons move to a higher energy level after being excited. They then move back to their ground level producing photons with lower energies compared to the absorbed photons ⁸⁵. Fluorescence microscopy involves using fluorophores targeting specific structures in a sample. The emitted light from the fluorophore is measured and used to create an image of the sample.

Fluorescence microscopy has reached the point of becoming an essential tool in biological experiments. It is a powerful technique that allows researchers to study the structure and function of cells with good spatial resolution ⁸⁶. With an array of developed fluorescent probes which offer a high degree of specificity in fluorescence microscopic detection, subcellular structures such as the nucleus, ER, Golgi apparatus, mitochondria, cytoskeleton, LDs, cell membrane and lysosomes, and key biomolecules within cells and tissues including proteins, nucleic acids, lipids, carbohydrates and cell metabolites like glucose could be identified and quantitatively analysed. One specific application of fluorescence microscopy is the study of ECs organelles. By using fluorescence microscopy, insights into the behaviour of ECs organelles, their contribution to the overall health of the cardiovascular system, and the biochemical changes associated with the development of ED and diseases could be identified.

One of the most important uses of fluorescence microscopy in the study of ECs is the visualization of cellular organelles which could be targeted using fluorescence dyes that specifically bind to certain components of the respective organelle. For example, the use of Hoechst or 4',6-diamidino-2-phenylindole (DAPI) to selectively stain cellular DNA and visualize cell nuclei ⁸⁷, as well as using stains such as MitoTracker, ER-Tracker and LysoTracker to selectively target mitochondria, the ER and the lysosomes, respectively ⁸⁸, as MitoTracker targets mitochondrial membrane potential, ER-Tracker bind to its membranes and LysoTracker accumulates in lysosomes' acidic environment. Lipophilic dyes such as BODIPY (boron dipyrromethene), Nile red or Oil red O (ORO) are routinely used to image the distribution of LDs in ECs ⁸⁹.

Another application of fluorescence microscopy in the study of ECs is the use of fluorescence-labelled antibodies to study the distribution and localization of specific proteins within the cells ⁹⁰. This technique, known as immunofluorescence, is particularly useful for studying the distribution of signalling proteins and other important molecules within the cells. One example of this is the immunostaining of surface adhesion molecules such as ICAM-1 to shed the light on EC inflammatory response to various stimulations ⁶⁹. By labelling these proteins with fluorescence-

labelled antibodies, the determination of the distribution of these proteins within the cells and their interactions with other cellular components could be investigated.

In addition to these traditional applications, fluorescence microscopy can also be used to study the dynamic behaviour of cells in real-time. For example, by using techniques such as fluorescence recovery after photobleaching (FRAP) and fluorescence loss in photobleaching (FLIP), the behaviour of organelles and other cellular components as they move and interact with one another could be studied. These techniques allow researchers to gain insights into the dynamic behaviour of cells in real-time, providing valuable information about the interactions between organelles and other cellular components.

Despite its many advantages, fluorescence microscopy is burdened with limitations including a limited overall number of dyes that could be used simultaneously, as usually no more than three dyes could be used in a single cell or tissue sample, restricting the number of cellular organelles or cellular processes to be studied simultaneously. It is also worth noting that some dyes exert cytotoxic properties and so could not be used to image live cells. Additionally, cell permeability is to be considered in this regard, as some dyes require cell permeabilization too. Furthermore, many dyes hold the risk of photobleaching and phototoxicity ⁸⁶.

6.2. Transient absorption microscopy

Transient absorption microscopy is a cutting-edge technique used to study the dynamics of photochemical and photophysical processes in a wide range of materials, including biological systems, polymers, and semiconductors. The method is based on the principle of transient absorption spectroscopy, which involves the measurement of changes in the absorption of light by a sample over time following an excitation pulse ⁹¹.

To perform transient absorption microscopy, a sample is first excited with a short, intense laser pulse, typically in the ultraviolet or visible range. This pulse generates a transient population of excited states within the sample, which can then be probed with

a second laser pulse at a different wavelength and time delay ⁹¹. The resulting changes in the absorption of the probe pulse are then detected using a highly sensitive detector, allowing for the visualization of the spatiotemporal dynamics of the photoexcited sample ⁹².

One of the key advantages of transient absorption microscopy is its high temporal and spatial resolution, which can provide insights into the ultrafast dynamics of energy and charge transfer processes occurring within materials ⁹². The technique can also be used to study the interaction of materials with light, including the absorption and scattering of photons, as well as the formation and evolution of excited states.

However, transient absorption microscopy also presents some challenges, including the need for highly specialized and sensitive instrumentation, as well as the difficulty in accurately interpreting the complex data obtained from the technique. Additionally, the use of high-intensity laser pulses can lead to photodamage of the sample, which must be carefully controlled to avoid damaging biological specimens.

Despite these challenges, transient absorption microscopy is a highly valuable tool for the study of photochemical and photophysical processes in a wide range of materials, with potential applications in chemical and biological assessments of cells and tissues ⁹². As new advances in technology and instrumentation continue to emerge, the potential for transient absorption microscopy to reveal new insights into the dynamics of light-matter interactions will only continue to grow.

7. Raman Spectroscopy

The Raman effect was first theorized by Adolf Smekal and later proven experimentally by C. V. Raman in 1928^{93,94}. Over the past 90 years, Raman spectroscopy has become an increasingly popular field of study, with advancements in technology and instrumentation making it a valuable tool for scientists in many different fields.

The measurement of inelastically scattered photons, originated when a light source interacts with samples' molecular vibrations is the basis of this powerful analytical technique⁹⁵. The resulting scattered photons could have the same energy of the light source, this represents Rayleigh scattering. If the photons' energy is changed, this indicates Raman scattering. There are two types of Raman scattered light: Stokes Raman scattering, which has a lower frequency than the illumination source, and anti-Stokes Raman scattering, which has a higher frequency⁹⁶.

Raman spectra are usually displayed in the wavenumbers scale, also known as the Raman shift. A sample's Raman spectrum could be helpful in identifying many aspects including the sample's chemical composition and structure. Unknown samples can be identified based on their unique Raman spectrum and the intensity of Raman bands can determine sample's concentration⁹⁵.

7.1. Confocal Raman imaging

Confocal Raman microscopy, also known as Raman imaging is a very powerful tool to investigate complex biological samples, such as cells. A Raman spectrometer and a confocal microscope are joined (Figure 7.1), and a CCD camera is usually used to record the Raman spectra from each measured pixel. A microscope lens is used to focus the laser beam onto the sample, resulting in a good imaging special resolution^{37,97}.

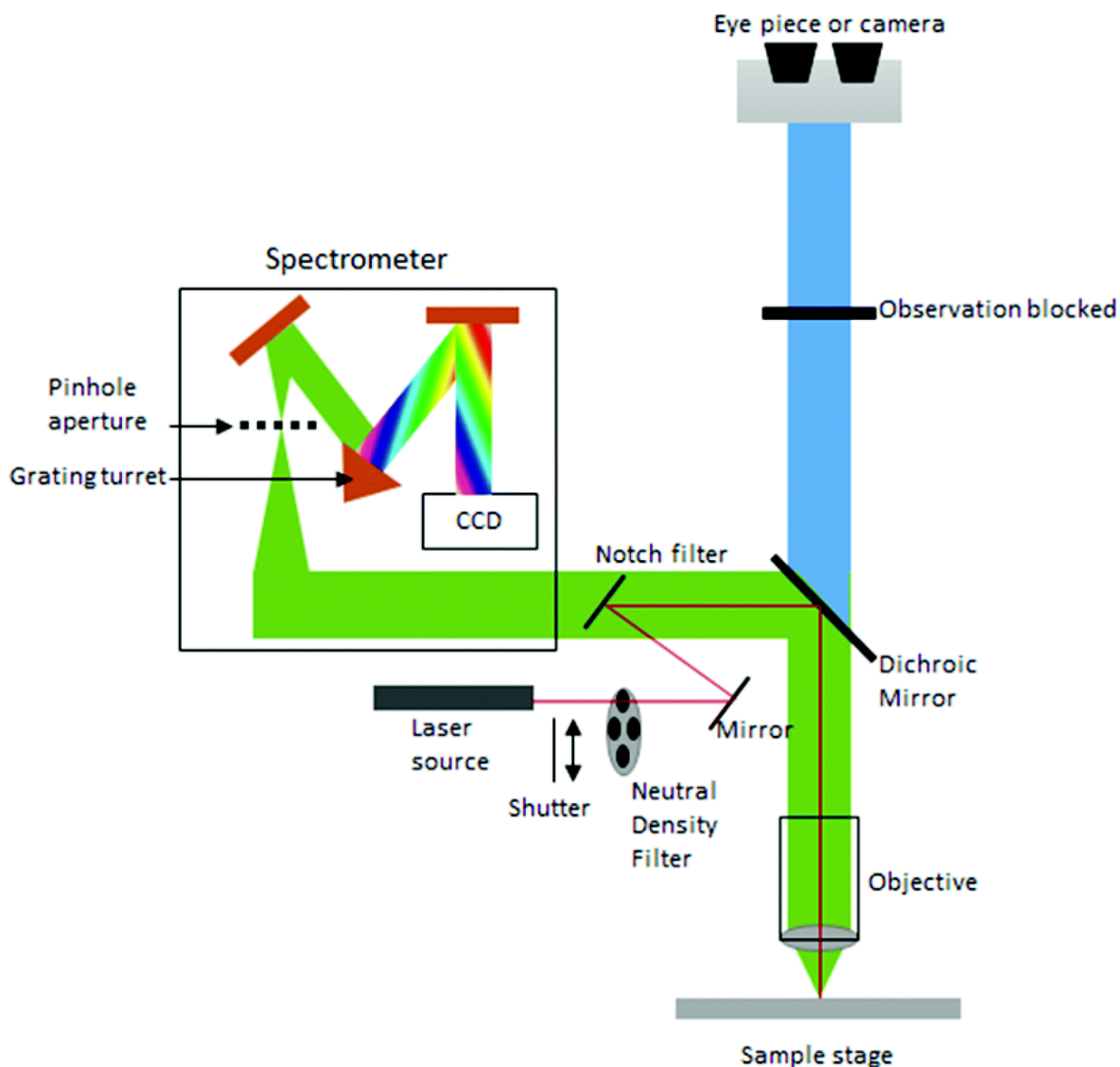


Figure 7.1. Basic setup of a Raman microscope. The figure is adapted from Ref. [37], covered by CC BY 3.0 license allowing free sharing and adapting.

The collected Raman spectra could be integrated at specific spectral bands to computationally produce a pseudo-colour image based on the relative intensity of the selected band or bands at each measured pixel. This method allows for visualizing subcellular compartments and for obtaining vital information on the biochemistry of the cellular organelles of interest. Furthermore, this technique has been used in many of the studies composing the experimental section of this thesis.

The spatial resolution of Raman microscopy can range from several micrometres to several tens of nanometers, depending on the specific instrument and experimental conditions ⁹⁸. In general, the spatial resolution of Raman microscopy is lower than that of some other imaging techniques, such as electron microscopy, but it offers the advantage of the non-destructive, non-invasive analysis of a wide range of samples including biological tissues and cells, without requiring staining or labelling.

A common way to estimate the spatial resolution of a Raman microscope is to use the Rayleigh criterion, which states that the spatial resolution is determined by the distance between the diffraction-limited spots of two-point sources ⁹⁹. In other words, the resolution is limited by the smallest distance between two points that can be distinguished as separate features in the image.

The Rayleigh criterion is expressed mathematically as:

$$\Delta x = 0.61\lambda/NA$$

where Δx is the spatial resolution, λ is the wavelength of the excitation laser, and NA is the numerical aperture of the objective lens. This formula provides an estimate of the minimum distance between two points in the sample that can be resolved by the microscope ⁹⁹.

It is important to note that this formula is a theoretical approximation and does not account for experimental factors such as sample preparation, signal-to-noise ratio, or other sources of noise. In practice, the actual spatial resolution achieved by a Raman microscope may be lower than the theoretical limit due to these factors ⁹⁸.

7.1.1. Label-free Raman imaging of cellular organelles

Imaging of subcellular structures and identifying the underlying chemical properties and the biochemical changes and abnormalities associated with disease development has gained increasing popularity due to their potential in improving our understanding of cellular processes and enhancing the diagnosis and treatment of different conditions ¹⁰⁰. This is true in the case of ECs as identifying biochemical

processes associated with endothelial inflammation and ED at the subcellular level allows for a better understanding of endothelial health and disease and holds the potential for developing novel therapeutic approaches for endothelial-related pathologies. Selected mechanisms of ED and endothelial-related disease progression are discussed in chapter 4.

As a label-free technique, one of the greatest advantages of Raman spectroscopy is that it allows obtaining comprehensive information on samples' biochemical composition without relying on dyes. Imaging cellular organelles with a high spatial resolution is one of the most popular applications of Raman imaging. This is possible due to the possibility of identifying key biological compounds (such as nucleic acids, lipids and proteins) based on their characteristic Raman bands corresponding to the vibrational modes of their respective molecules. Details on the label-free as well as labelled Raman imaging of cellular organelles is discussed in chapter 10.2.

8. Molecular Raman probes

As a label-free technique, Raman imaging could provide key information on the distribution and, in some cases, the concentrations of important biomolecules in the cells and tissues such as nucleic acids, proteins and lipids without relying on dyes. This presents one of the advantages of Raman imaging as it excludes the undesirable effects dyes might have on the samples (including in some cases cytotoxicity), moreover, sample preparation time is cut short as the staining process is not necessary, and the risk of photobleaching is eliminated¹⁰¹. On the other hand, biological samples such as cells are very complex systems with an array of different biomolecules whose characteristic Raman bands could overlap limiting, to some extent, this technique's sensitivity and selectivity in identifying the changes in endothelial subcellular structures associated with the development of ED¹⁰. Increasing the sensitivity and selectivity of Raman microscopy techniques is one of the motivators leading to the popularization of molecular Raman probes.

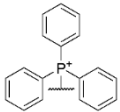
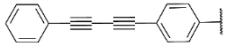
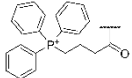
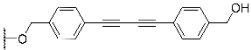
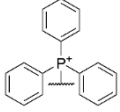
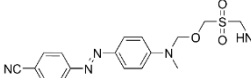
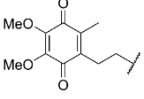
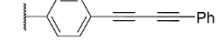
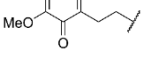



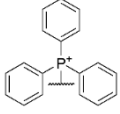

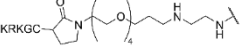
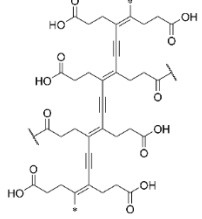
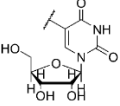

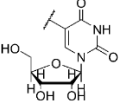

8.1. Concept, advantages and limitations

Molecular Raman probes is a term used to describe usually small molecules that have the ability to target specific cellular organelles or specific molecules and improve their Raman imaging. Raman probes normally contain two main parts; A targeting moiety which contributes to the probes' ability to mark a certain structure specifically, and a Raman reporting moiety which improves the Raman signal from the targeted structure. This signal improvement could be a result of signal enhancements (e.g. providing resonantly enhanced Raman bands when excited with specific wavenumber) or avoiding overlapping with other Raman bands (e.g. providing a band in the Raman biologically silent spectral region [1800 – 2800 cm⁻¹]). Another approach to molecular Raman probes is based on isotopically labelling specific molecules which could help follow specifically interesting cellular mechanisms¹⁰. Indeed, many Raman probes have been shown to significantly improve the sensitivity

and selectivity of subcellular Raman imaging. A selected summary of Raman probes is presented in (Table 8.1).

Ideally, Raman probes should be relatively inert molecules that offer good signal enhancement with minimal effects in the samples. Moreover, it is desirable for Raman probes to have good selectivity and to exert no issues in solubility or cellular uptake. With many molecular Raman probes coming close, none of them is ideal, with some showing limitations related to poor solubility, reduced cellular uptake or photosensitivity^{10,57}.

Selected summary of Raman Probes

Name	Targeting moiety	Raman reporting moiety	Target	Band Position [cm ⁻¹]	Reference
MitoBady			Mitochondria	2220	102
TTP-BDDBPDM				2216	103
MitoAzo				1375	104
AITQ2				2249	105
AltQ4				2258	
AltQ5				2231	
Mito-Carbow2141				2141	106
P3				2120	107
EdU			DNA	2122	105,108-110
Modification of EdU with				2203(C≡C) and 2631 (B-B)	111

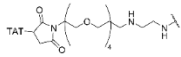
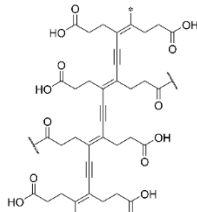
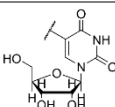
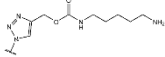
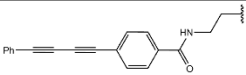
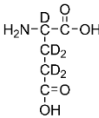
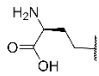

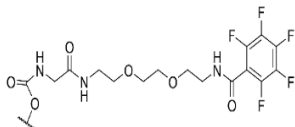
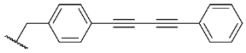
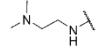
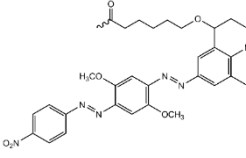
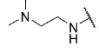
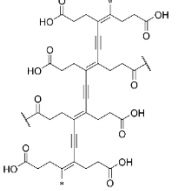
ortho-carborane					
P4	 TAT: CRRRQRRKKR		DNA	2120	107
¹³C EU		¹³ C ≡ ¹³ CH	RNA	2077	108,110,112
Nε-[(2-propynyloxy)carbonyl]-L-lysine				2135	113
D5-Glutamin		C-D	ER	2067	114
L-Homo-propargylglycine (Hpg)				2120	109,112
Carbow 2226 ER				2226	106
BlackBerry Quencher 650 (BBQ-650)-LYSO			Lysosomes	1087–1133	115
PDDA-LYSO				2120	107

Table 8.1. Summary of Raman probes. The table represents the names of Raman probes, the chemical structures of their targeting and Raman reporting moieties, their subcellular targets, their characteristic Raman bands positions, and the references where they were studied. ER: endoplasmic reticulum. The table is reproduced from Ref. [10], covered by CC BY 4.0 license allowing free sharing and adapting.

8.2. Label-free vs labelled Raman imaging of cellular organelles

As previously mentioned, label-free Raman imaging allows visualization of key biological molecules such as nucleic acids, lipids and proteins with a good spatial resolution (Figure 8.1). This would allow localizing of cellular organelles where these molecules are most abundant. For example, following the Raman bands associated with DNA vibrational modes (such as the Raman band at ca. 785 cm^{-1} characteristic for the vibration of phosphodiester bonds in DNA) allows visualizing the cell nucleus. Similarly, imaging other subcellular structures could be accomplished by following the Raman bands arising from the vibrational modes that are characteristic of each cellular organelle (mentioned in detail below).

Alternatively, the use of molecular Raman probes could target specific molecules or subcellular structures allowing their visualization with degrees of sensitivity and selectivity that varies from one Raman probe to another, however, in most cases they have been shown to improve Raman visualization of target structures (discussed in details below).

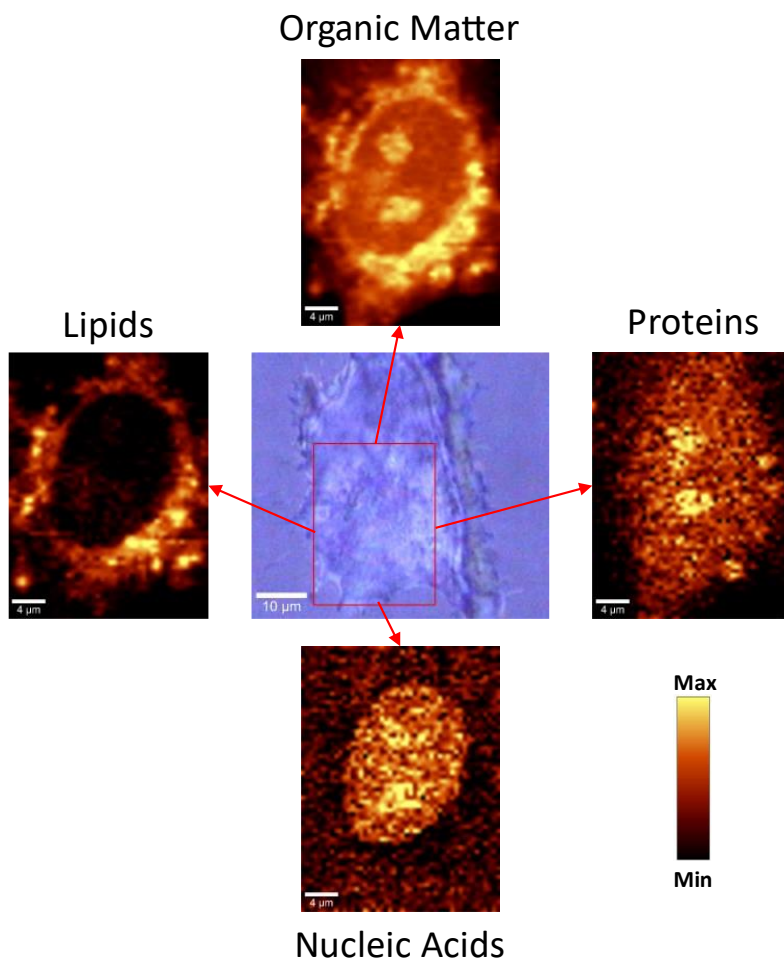


Figure 8.1. Label-free Raman imaging biomolecules. In the middle: a bright field image of a fixed HMEC-1, scale bar equals 10 μm , surrounded by pseudo-colour intensity images (scale bars equal 4 μm) showing the distribution of all organic compounds, lipids, proteins and nucleic acids, constructed by the integration of the Raman spectra at 2800-3030 cm^{-1} , 2830-2900 cm^{-1} , 996-1016 cm^{-1} and 770-810 cm^{-1} , respectively.

8.2.1. Nucleus

Label-free Raman imaging of cell nuclei could be achieved by identifying the Raman bands attributed to the vibrations of nucleotides and sugar–phosphate backbones of DNA and RNA i.e. the Raman bands arising at ca. 785 cm^{-1} and at ca. 813 cm^{-1} attributed to phosphodiester bonds in DNA and RNA, respectively, as well as the band at ca. 1095 cm^{-1} associated with phosphodioxy (PO_2^-) group vibration

^{10,116}. Based on this, Raman visualization of cell nuclei and identification of changes related to various processes could be achieved. For example, in a Raman imaging study of ECs, early apoptosis induced by *in vitro* incubation with Fas ligand (FasL), an increase in the DNA Raman band at ca. 785 cm⁻¹ was observed ¹¹⁷. This effect, studied using label-free Raman imaging, was believed to be due to chromatin condensation in early apoptotic ECs.

There are different molecules that have been used as Raman probes for imaging cell nuclei. Perhaps the most popular one of these is EdU, which is a thymidine analogue with an alkyne tag (chemical structure in Table 8.1) that gets incorporated into newly synthesized DNA ¹¹⁸. In order to fluorescently label EdU, a “copper(I)-catalyzed azide–alkyne [3 + 2] cycloaddition” (CuAAC) reaction, known as “the crown jewel of click chemistry”, is necessary between EdU and a fluorescent azide ^{119,120}. On the other hand, Raman identification of EdU could be achieved without the “click chemistry” reaction (in a “click-free” fashion), due to its characteristic alkyne band at ca. 2122 cm⁻¹ in the spectral silent region ¹⁰⁸. This makes EdU an ideal molecular Raman probe for imaging cell nuclei. However, it specifically probes DNA synthesis (evidenced by the disappearance of the EdU Raman band in EdU-tagged cells incubated with the DNA synthesis inhibitor hydroxyurea ^{109,112}), thus could be employed as a Raman probe for DNA replication and cell proliferation.

Similarly to EdU, 5-Ethynyl uridine (EU) could be used to selectively label RNA ¹²¹. Isotopically edited EdU and EU have been used simultaneously for the SRS-based imaging of DNA and RNA, respectively ¹¹⁰. Both EdU and EU demonstrate two key advantages over label-free Raman imaging of DNA and RNA; 1) the ability to selectively image DNA alone (EdU) and RNA alone (EU), while it is very difficult to isolate the label-free Raman signal of DNA and RNA due to their proximity and possible overlapping in the Raman spectra of cells, and 2) the ability to track DNA or RNA synthesis which gives important information on cellular processes such as cell proliferation, a process that cannot be measured using label-free Raman imaging.

8.2.2. Mitochondria

Label-free Raman imaging of mitochondria could be achieved by the identification of the Raman bands characteristic for the cytochrome complex at ca. 750, 1130, 1310 and 1590 cm^{-1} . However, due to the relatively low mitochondrial content in ECs and the overlapping of cytochrome Raman bands with bands associated with more abundant intracellular proteins and lipids, label-free Raman detection of cytochrome and imaging of ECs mitochondria is limited to resonance Raman conditions (achieved by using a laser with an excitation wavelength below 550 nm)^{122,123}. Moreover, label-free Raman imaging of ECs mitochondria is often limited to live-cell imaging.

For such an important cellular organelle whose label-free Raman imaging is restricted to specific conditions, different mitochondrial labelled Raman imaging approaches have been developed. One of which is based on the Raman probe MitoBADY whose targeting moiety is a triphenylphosphonium cation (TPP^+) capable of targeting mitochondria due to its highly negative transmembrane potential, and whose Raman reporting moiety is bis(aryl)butadiyne (BADY) demonstrating a strong undisturbed Raman band at ca. 2220 cm^{-1} in the silent region^{102,124}. Other Raman probes such as MitoAzo were developed by coupling the mitochondria targeting moiety TPP^+ with an azobenzene-based probe giving a resonantly enhanced Raman band at 1375 cm^{-1} ¹⁰⁴. Moreover, labelled Raman imaging of mitochondria has also been performed using analogues of coenzyme Q (AITQs)¹⁰⁵. Examples of labelled Raman imaging of the mitochondria are presented in (Figure 8.2A).

8.2.3. Lipid droplets

Label-free Raman microscopy is indeed a strong technique for studying lipids and imaging the intracellular distribution of LDs. This is partly due to the existence of long hydrocarbon chains in lipids structures causing a large scattering cross-section.

Thus, lipids could be detected in different Raman spectral regions i.e. 3000 – 2800 cm^{-1} (C–H stretching), 1500 – 1400 cm^{-1} (CH_2 group scissoring), 1300 – 1250 cm^{-1} (CH_3 group twisting) and 1200 – 1050 cm^{-1} (C–C stretching) ^{10,52,125,126}. Furthermore, characteristic chemical changes in LDs composition due to ECs inflammation, resulting in an increased LDs content with unsaturated characteristics, were studied using label-free Raman imaging ¹²⁷.

Label-free Raman imaging of lipids including in ECs is done relatively easily. Nevertheless, specific molecular Raman probes could still offer improvements to lipid detection and the underlying cellular mechanisms relating to lipids in the cells. For example, the use of deuterated cholesterol (such as D-38 cholesterol) has been used to track cholesterol accumulation in LDs with no effects on cellular processes ¹²⁸. Moreover, the use of deuterated or alkylated fatty acids enabled the detection of fatty acids transport and shed the light on their role in some cellular mechanisms ^{129–132}.

Finally, we introduced a new use for the naturally occurring carotenoid astaxanthin as a Raman probe for subcellular lipidic structures in ECs, allowing the detection of lipids with 10 times lower laser power than the one used in label-free Raman imaging (explained in detail in the experimental section).

8.2.4. Lysosomes

Label-free Raman detection of lysosomes and alterations in their structures or distributions is not possible. Therefore, a few approaches to labelled imaging of lysosomes have been introduced. A Raman probe with N,N-dimethylethylenediamine as moiety sensitive to lysosomes, conjugated with BlackBerry Quencher 650 (BBQ-650) was used for Raman imaging of lysosomes benefiting from a signal enhancement based on using a laser with $\lambda = 633 \text{ nm}$, close to the range in which BBQ-650 absorbs light ¹¹⁵. Similarly, poly(deca-4,6-diyneic acid) (PDDA) was used to target lysosomes for SRS imaging applications ¹⁰⁷ (shown in Figure 8.2.C).

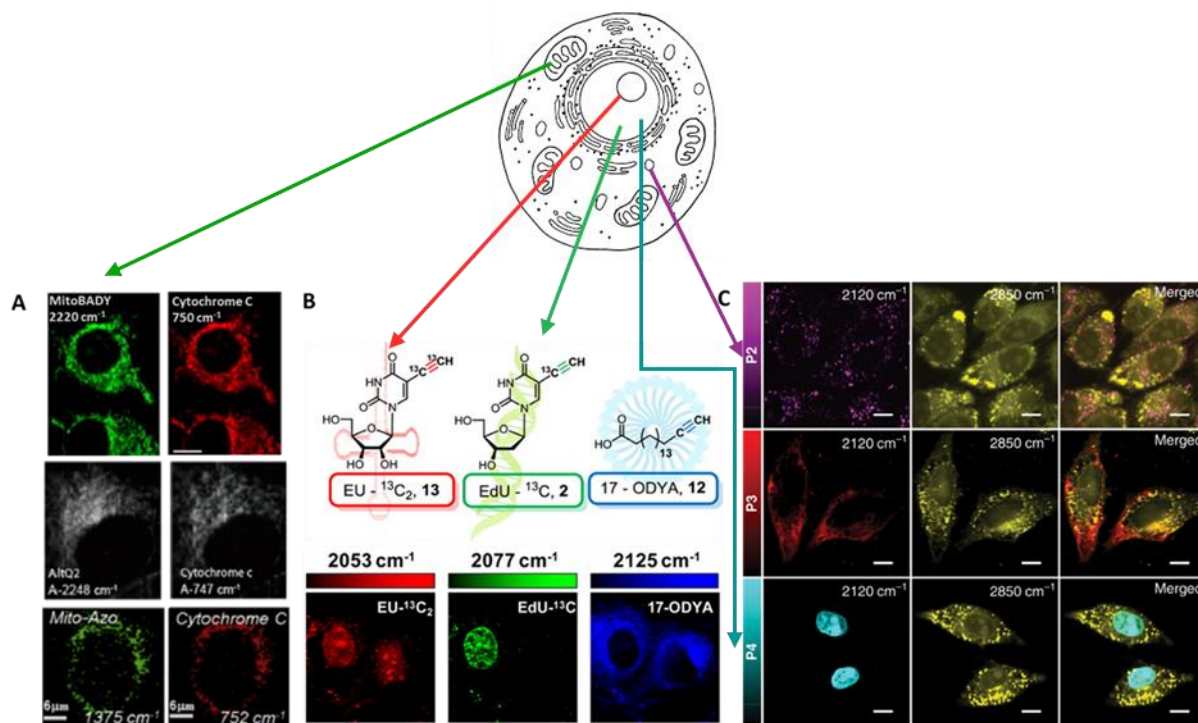


Figure 8.2 Labelled Raman subcellular imaging. (A) Labelled Raman imaging of mitochondria using the Raman probes MitoBADY, AITQ2 and Mito-Azo (left) compared to label-free Raman imaging of cytochrome c (right) in live HeLa cells ^{102,104,105}. (B) Structures of EU- $^{13}\text{C}_2$, EdU- ^{13}C , and 17-ODYA above their corresponding SRS images in live HeLa cells, showing the distributions of RNA, DNA and fatty acids, respectively ¹¹⁰. (C) SRS imaging of lysosomes (P2), mitochondria (P3) and nucleus (p4) based on targeting corresponding PDDA probes overlaid with lipids distribution (2850 cm^{-1}) ¹⁰⁷. Scale bars equal 10 μm . The figure is reproduced from Ref. [10], covered by CC BY 4.0 license allowing free sharing and adapting.

Experimental Section

9. Introduction to the experimental section

The introduction section of the thesis highlighted the importance of the vascular endothelium and the multiple functions that ECs play towards maintaining cardiovascular homeostasis. Consequently, ED holds a great deal of significance regarding the development of multiple diseases, where alterations occurring at the subcellular level of ECs contribute to ED and the progression of various diseases. Therefore, developing new methods of imaging ECs at the subcellular level and understanding the biochemical changes associated with the development of ED is of great importance. With Raman microscopy being one of the best tools to identify biochemical alterations in a complex way within the cell, and the specificity and enhancement that molecular Raman probes could offer in this regard, label-free and labelled Raman imaging complemented with techniques such as fluorescence microscopy and transient absorption (TA) microscopy were used to study *in vitro* and *ex vivo* models of ED.

9.1. A novel approach to image lipids in endothelial cells based on astaxanthin labelling

With ECs activation and inflammatory response being a life-preserving strategy in response aiming to eliminate pathogens and defective cells, prolonged ECs activation and inflammation are interconnected with the development and progression of many endothelium-related pathologies³⁴. Stimulation of ECs with TNF- α is considered one of the most common models to study endothelial inflammation *in vitro*. Upon incubating ECs with TNF- α , cells are activated through the NF- κ B pathway^{127,133}. Consequently, an increased expression of adhesion molecules including ICAM-1, VCAM-1 and COX-2 is observed. Moreover, the resulting ECs inflammation leads to alterations in ECs' lipids content, specifically LDs, where inflamed ECs are shown to possess a higher number of LDs containing lipids of unsaturated characteristics^{10,57,127}.

Carotenoids are natural compounds found in algae, plants and animals. They are structurally tetraterpenoids containing multiple carbon-carbon double bonds

appearing in colours ranging from yellow to red ^{134,135}. AXT is one of the compounds belonging to the xanthophylls classification of the carotenoids group ¹³⁴⁻¹³⁶. AXT is a red pigment widely studied for its antioxidant and anti-inflammatory effects and is suggested to exert anticancer and antidiabetic properties ¹³⁶⁻¹⁴⁰. AXT absorbs the light in the visible range coinciding with the excitation of most lasers used for Raman imaging of cells, thus showing resonantly enhanced Raman bands at ca. 1520, 1159 and 1009 cm^{-1} ^{134,141,142}. AXT has a high affinity towards lipids causing it to accumulate in cells and tissues in specific lipidic structures ¹⁴¹.

A novel method to study the distribution of relatively small amounts of lipids in ECs and identify the changes in ECs' lipid content upon inflammation, relying upon AXT as a molecular Raman probe, is shown here as the first part of the experimental section.

9.2. Assessment of astaxanthin as a Raman probe for endothelial cells lipids, addressing cells heterogeneity.

ECs demonstrate a great deal of heterogeneity across different organs in the body. This heterogeneity allows ECs to carry out specific tasks related to the needs of each organ. After establishing AXT as molecular Raman probe biosensing lipidic structures in ECs, a study was conducted to test the hypothesis that AXT is a universal Raman probe for studying lipids in ECs despite their origins.

With a lot of studies done on its effects on cellular mechanisms and a couple of studies done on its use as a lipid probe, little is known about the excited-state dynamics of AXT in cells. A transient absorption microscopy-based collaborative work with Tingxiang Yang and Prof. Benjamin Dietzek of Leibniz Institute of Photonic Technology (Leibniz-IPHT) was performed in order to shed the light on the excited-state dynamics of AXT in live cells and to clarify whether or not AXT exists in the aggregated form in cells.

9.3. Studying the endothelial cells' uptake of astaxanthin in free and encapsulated forms

Liposomes are nanoscale vesicle structures assembled from non-toxic phospholipids that have found wide application in cargo transport of both lipophilic and lipophobic molecules into cells¹⁴³. Liposomal encapsulation has been used to solubilize, increase bioavailability, and improve the stability of several bioactive molecules and natural products while having the advantages of being customizable for different applications, relatively biocompatible and biodegradable^{143,144}.

Due to its chemical structure that consists of a long polyene chain and two terminal rings, AXT is highly lipophilic, which limits its bioavailability and consequently its use as an antioxidant dietary supplement. Liposomal encapsulation is one of the methods shown to improve AXT bioavailability, antioxidant effect, stability and solubilization. It was reported that both neutral and positively-charged liposomes enhance the efficacy of AXT cytoprotective effects *in vitro*^{145–147}.

The uptake and anti-inflammatory effects on ECs of free and encapsulated AXT (in neutral liposomes and cationic lipoplexes) were investigated using Raman and fluorescence microscopies.

9.4. A novel approach to assay endothelial cells' proliferation and regeneration in *in vitro* and *ex vivo* conditions

The phenotype of ED is usually interconnected with the inability of ECs to regenerate, starting at the impairment of ECs proliferation capacity, resulting in failure to repair ED^{19,148}. Therefore, studying ECs proliferation and their capacity to regenerate is of high importance. Moreover, applications of probing ECs regeneration are especially important in *in vivo* and *ex vivo* conditions where the experimental environments are closer to that of real life and interactions between ECs and other cell types are taken into consideration.

There are different techniques utilized to assay cell proliferation, the majority of which rely on monitoring changes in the number of cell populations over time. For example, cell counting using viability dyes such as trypan blue or Calcein-AM can provide both the rate of proliferation and the percentage of viable cells, Calcein and

PI-DNA can be utilized for simultaneous fluorescence detection of viable and dead cells¹⁴⁹, Carboxyfluorescein succinimidyl ester (CFSE) is used to permanently label cells and study their division based on the decrease in cell fluorescence¹⁵⁰. Metabolic proliferations assays, such as MTT, XTT or WST-1 have been used to assess the metabolic activity of the samples and indirectly assay proliferation. It's also possible to detect cell proliferation by utilizing specific monoclonal antibodies, for example using antibodies against Ki-67 protein^{151,152}.

Nevertheless, DNA synthesis proliferation assays, based on the detection of incorporated labelled molecules into samples' DNA, are usually the methods of choice to probe the proliferation and regeneration of ECs. 3H-thymidine, BrdU and EdU assays are examples of such approaches where a thymidine analogue or an isotope is incorporated into cells' DNA during replication, and proliferation is assayed based on the cell count and the signal intensity from the used probe^{153,154}. In this category, the EdU assay is the most advantageous as it does not rely on radioisotopes (like the 3H-thymidine assay), or antibodies (like the BrdU assay). Moreover, it does not require DNA denaturation and uses relatively low molecular weight dyes.

5-ethynyl-2'-deoxyuridine (EdU) is a thymidine analogue that gets incorporated into newly synthesized DNA and is used to assay cell proliferation after being labelled with an azide fluorescent dye *via* a "click chemistry" reaction^{119,120} (Figure 9.1A). On the other hand, Raman identification of EdU could be done in a "click-free" manner, due to its characteristic alkyne Raman band at ca. 2122 cm^{-1} in the spectral silent region (Figure 9.1B)¹⁰⁸. The advantage of such a Raman imaging-based approach is that it does not rely on non-permeable dyes or the "click chemistry" with the cytotoxic copper, allowing EdU imaging in live ECs. Raman imaging of EdU-labelled cell nuclei was previously reported^{108,155}. However, a Raman imaging-based assay of ECs proliferation *in vitro*, and more importantly of ECs regeneration *ex vivo* was reported for the first time as part of the results obtained during the completion of this PhD thesis.

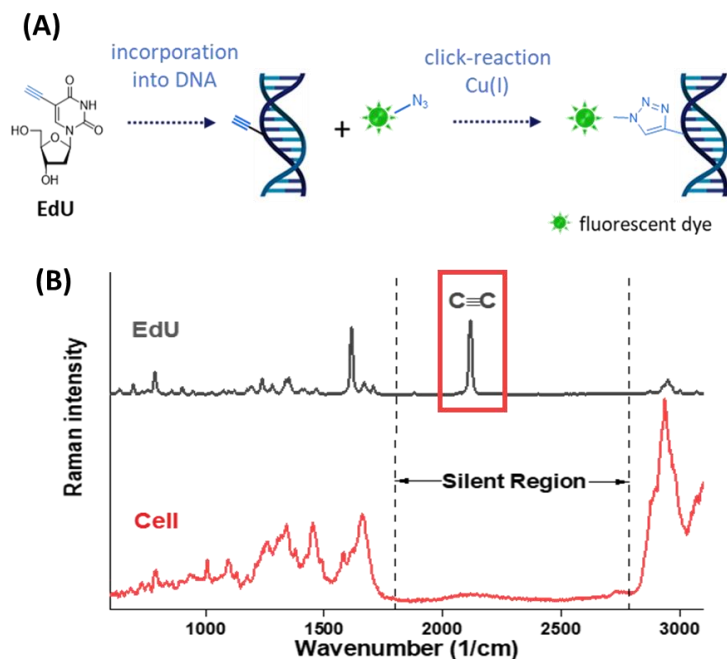


Figure 9.1. Fluorescence “click chemistry” vs Raman “click-free” detection of EdU. (A) Basis of the fluorescence microscopy detection of EdU as EdU incorporates into DNA, then a “click chemistry” reaction is used to fluorescently label it. (B) A Raman spectrum of EdU (black) showing its alkyne (C≡C) Raman band in the cell spectroscopically silent region presented in an averaged cell spectrum (red).

ECs proliferation assay using a Raman imaging-based approach was performed using fluorescence imaging of EdU (after its “click chemistry” reaction with a fluorescent dye) as a reference method. For the *in vitro* assays, ECs treated with cycloheximide (CHX), a widely used protein synthesis inhibitor that inhibits cellular DNA synthesis by stalling replication forks due to protein deprivation^{156,157}, were used as a model for impaired cell proliferation. Another model was used based on Doxorubicin (DOX) treatment. DOX is an anthracycline antibiotic limitedly used in cancer treatment due to its cardiotoxicity that causes inhibition of cell proliferation as well¹⁵⁸. Moreover, ECs regeneration *ex vivo* is studied in isolated murine aorta after induced mechanical injury to the endothelium tagged with EdU.

10. Imaging lipids in endothelial cells based on astaxanthin labelling

Part of the results reported in this chapter, obtained during the completion of the PhD thesis, are already published and are available under Ref. [57] and Ref [101].

“**Radwan, B.**; Adamczyk, A.; Tott, S.; Czamara, K.; Kaminska, K.; Matuszyk, E.; Baranska, M. Labeled vs. Label-Free Raman Imaging of Lipids in Endothelial Cells of Various Origins. *Molecules* **2020**, *25* (23), 5752”.

“Czamara, K.; Adamczyk, A.; Stojak, M.; **Radwan, B.**; Baranska, M. Astaxanthin as a New Raman Probe for Biosensing of Specific Subcellular Lipidic Structures: Can We Detect Lipids in Cells under Resonance Conditions? *Cell. Mol. Life Sci.* **2021**, *78* (7), 3477–3484”.

10.1. Objectives of the study

With the significance and motivation of introducing a new method to study endothelial subcellular lipid-rich structures discussed in previous chapters and the properties of AXT, especially its high affinity towards lipids and its distinct Raman spectrum, the study presented in this chapter was aimed at assessing the potential of AXT to be used as a Raman probe for lipids in ECs. Moreover, this work was aimed at demonstrating the time-dependent accumulation of AXT in lipid-rich cellular organelles, namely LDs and ER, and for the first time the nuclear envelope (which has not been possible until now to be imaged using label-free Raman techniques).

10.2. Materials and methods

10.2.1. Cell culture

For subsequent Raman measurements, HMEC-1 (ATCC® CRL-3243™, USA) were seeded on calcium fluoride (CaF₂) slides, to reach their optimal confluency

after 24h. HMEC-1 were cultivated in a complete MCDB131 medium (Gibco Life Technologies) supplemented with “10 mM L-glutamine (Gibco Life Technologies), 1 μ g/mL hydrocortisone (Sigma Aldrich), 10 mg/mL EGF (Sigma Aldrich), 10% FBS (Gibco Life Technologies) and antibiotic antimycotic solution consisting of 10.000 U penicillin, 10 mg streptomycin and 25 μ g amphotericin B per mL”. HMEC-1 were either pre-treated with 10 ng/ml TNF- α (Sigma Aldrich) or kept in a fresh medium for 24h. Subsequently, the cells were rinsed with PBS and exposed to cell culture media that contained AXT (Sigma Aldrich) at a concentration of 10 μ M for different durations such as 0, 30 minutes, 1h, 3h or 6h. The cells were then fixed using 2.5% glutaraldehyde for 4 minutes and immersed in PBS, after which they were preserved at 4°C until Raman imaging. Alternatively, samples of live cells were pre-treated with TNF- α for 24 hours, cleansed twice with PBS, and then subjected to a 6-hour incubation with AXT. They were subsequently washed and immediately subjected to imaging using the Raman microscope.

10.2.2. Raman imaging

Raman measurements were conducted using a “WITec alpha 300 Confocal Raman Imaging system” from “WITec GmbH in Germany”. The system was equipped with a CCD camera (Andor), a UHTS 300 spectrograph, and a 63x water immersive objective (Zeiss, NA = 1.0). A solid-state laser with an excitation wavelength of $\lambda = 532$ nm was used in all measurements. Each measurement was taken twice, once with a laser power of 3 mW (“low laser power”) and once with a laser power of 30 mW (“high laser power”). The measurements employed 0.5 and 1.0 μ m step sizes in the xy and xz dimensions, respectively, with an integration time of 0.5 s.

10.2.3. Quantification of ICAM-1 overexpression

HMEC-1 were seeded onto 96-well plates and left for 24 h to grow to the full confluency, then the cells were treated with: AXT (10 μ M, 3h), TNF- α (10 ng/mL, 24h), AXT with TNF- α simultaneously or AXT followed by TNF- α . Cells in fresh

MCDB131 medium and DMSO were considered negative controls. HMEC-1 were fixed using 2.5% glutaraldehyde for 4 min, incubated in the dark with mouse anti-human CD54-PE (BD Pharmingen) and stained with Hoechst 33342 (Life Technologies) for 30 minutes. The overexpression of surface ICAM-1 and cell nuclei were imaged by fluorescence microscopy (ScanR screening system). The images were analysed using Columbus 2.4.2 Software (Perkin Elmer).

10.2.4. Data analysis

Raman spectra obtained from all samples were processed by a routine cosmic ray removal and were baseline corrected using auto-polynomial of degree 2 (“WITec Project Plus” software). Pseudo-colour Raman images were obtained by the integration of the intensity of Raman bands in spectral ranges 1545-1495, 2900-3030 and 3030-2830 cm^{-1} corresponding to AXT, lipids and organic matter, respectively. In order to study the time-dependence of AXT accumulation, the intensity of the AXT band at ca. 1520 cm^{-1} was normalized for all the cells as zero value was set for the control (no AXT incubation) and the maximum set for the 6 hours incubation time group.

10.3. Results and discussion

10.3.1. Astaxanthin localization in endothelial cell lipid-rich organelles

Label-free Raman spectrum of a lipid droplet in an EC (Figure 10.1A), demonstrated key characteristic Raman bands for lipids, such as the ones at ca. 3015 cm^{-1} attributed to =C–H stretching, 2850 cm^{-1} for C–H stretching, 1660 cm^{-1} associated with C=C stretching, 1444 cm^{-1} attributed to -CH₂ group scissoring, 1305 cm^{-1} connected with the twisting of the CH₂ and CH₃ groups, and 1250 cm^{-1} characteristic for C–H bending. In order to obtain such spectrum identifying characteristic Raman bands for LDs in ECs, a laser of 532 nm wavelength was used to excite the samples, with a laser power of 30 mW at the cell samples was used.

When the same laser was used to excite the samples but with a laser power of 3 mW (10 times lower than the one used to obtain spectrum A), a spectrum consisting of noise with no identifiable Raman bands appeared (Figure 10.1B).

When ECs were incubated with 3,3'-dihydroxy- β,β' -carotene-4,4'-dione (AXT) (Figure 10.1), and measured using relatively low (3 mW) laser power, characteristic Raman bands of AXT (specifically at ca. 1520, 1159 and 1009 cm^{-1}) were observed at the LDs in cells (Figure 10.1C). This Raman spectrum of an LD of an EC stained with AXT and measured with low laser power correlated ideally with the spectrum of AXT dissolved in castor oil (Figure 10.1D). Unlike the Raman spectrum shown in (Figure 10.1E) of AXT powder which demonstrated a band at 1517 cm^{-1} , slightly shifted compared to the ones of AXT dissolved in castor oil or ECs lipids.

Utilizing relatively lower laser power (3 instead of 30 mW) to acquire the Raman spectrum of AXT is due to the fact that AXT is sensitive to higher laser power and could undergo bleaching. However, this condition comes with great potential for imaging LDs in ECs stained with AXT using lower laser power. This is especially beneficial for more fragile samples such as live ECs.

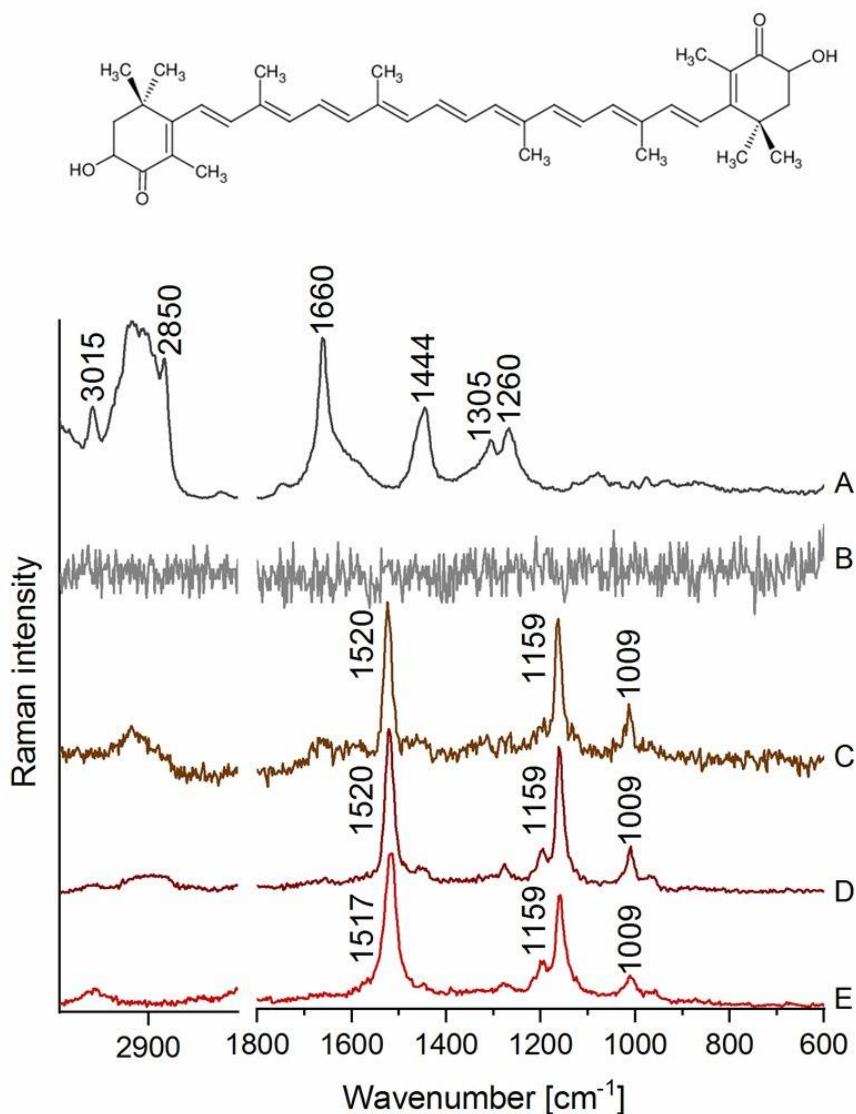


Figure 10.1. Label-free and AXT-labelled Raman spectra of EC lipids. Structure of AXT above (A) Raman spectrum of a lipid droplet (LD) in an EC measured using high (~ 30 mW) laser power. (B) Raman spectrum of an LD in an EC measured using low (~ 3 mW) power. (C) Raman spectrum of an LD in an EC subjected to AXT treatment (for 6h) and measured using low laser power. (D) Raman spectrum of AXT solution in a non-polar solvent (castor oil). (E) Raman spectrum of AXT powder.

The potential of AXT as a Raman probe for imaging lipid-rich cell organelles in ECs was tested in HMEC-1, where cells were incubated with AXT for different

times of incubation. Each cell was measured twice; First with lower laser power (3 mW), and then the same cells were measured with higher (30 mW) laser power, to image the distribution of AXT and lipids, respectively. The Raman spectrum of AXT showed resonantly enhanced Raman bands when excited with a 532 nm laser. The integration of the Raman spectrum of AXT's most intense band around 1520 cm^{-1} allowed for the detection of AXT distribution in ECs, whereas lipids' distribution was imaged by integrating the characteristic bands for lipids due to CH_2 stretching vibrations. AXT was found in the LDs of ECs starting from the 30-minute incubation group, with time-dependent accumulation in lipid-rich organelles. For shorter incubation times of 30 minutes and 1 hour, AXT accumulated in the LDs of ECs. The area of cells occupied by the ER, an organelle rich in phospholipids, showed AXT when incubated for 3 hours. Additionally, longer incubation times of 3 and 6 hours showed a clearer distribution of ECs lipids than the integration of Raman spectra for lipid bands (approximately 2850 cm^{-1}), producing images with enhanced contrast that also showed the nuclear envelope.

Inflammatory conditions induced by pre-incubation with the proinflammatory cytokine $\text{TNF-}\alpha$ led to changes in ECs' lipid content, resulting in an increase in intracellular lipids. AXT was used to image lipids in healthy (untreated) and inflamed ($\text{TNF-}\alpha$ treated) ECs. Figure 10.2 demonstrates increased AXT distribution in inflamed ECs, highlighting AXT's potential to image ECs' lipids and track changes in lipid distribution during pro-inflammatory treatment.

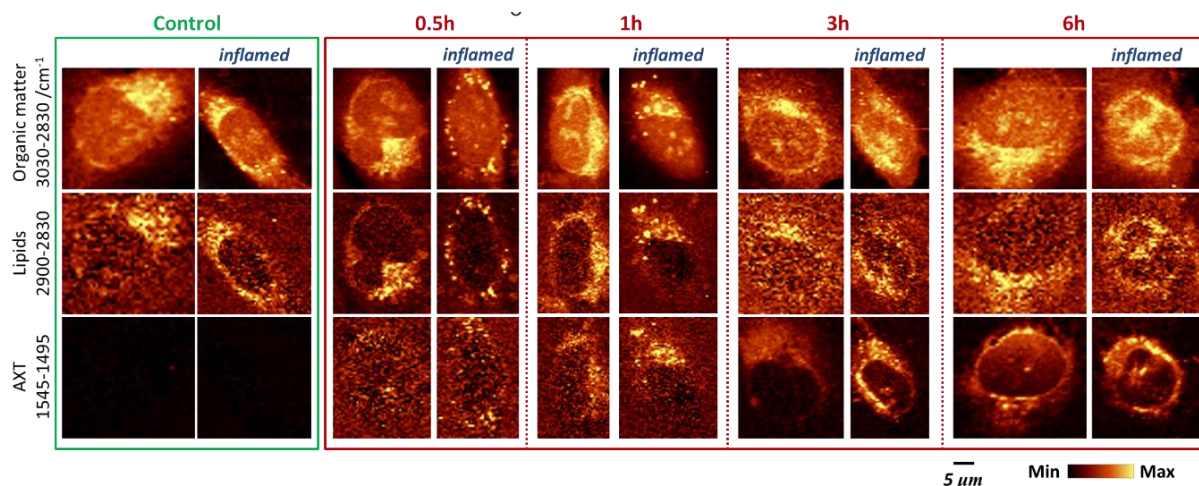


Figure 10.2. Time-dependent AXT accumulation and AXT-labelled Raman imaging in healthy and inflamed HMEC-1. Raman visualization of the distribution of organic matter, lipids, and AXT using high and low laser power (approximately 30 mW and 3 mW, respectively). The integration of Raman spectra obtained from designated regions in the figure was used to image these compounds in both control and AXT-labelled HMEC-1 cells at different time points (30 min, 1h, 3h, and 6h). In addition, a group of cells were pre-incubated with TNF- α for 24h to induce inflammation (labelled inflamed).

The results of the Raman imaging of AXT distribution in ECs lipid droplets are presented in (Figure 10.3). A comparison of images obtained using high and low laser powers revealed the distribution of lipids in the cell only in the image obtained with high laser power (Figure 10.3D). The integration of the Raman spectra in the spectral region associated with lipids ($2900 - 2830 \text{ cm}^{-1}$) measured using low laser power did not allow for the detection of the distribution of lipids in the cell (Figure 10.3B). However, the distribution of AXT (and consequently lipids) was clearly visible in the image obtained with low laser power (Figure 10.3C), but disappeared when measured with high laser power (Figure 10.3E) due to the bleaching of AXT.

These findings support the idea of AXT localization in ECs lipids, as demonstrated by the matching distribution seen in the figure's C and D images showing the distribution of AXT and lipids, respectively. Moreover, Figure 10.3F revealed that AXT accumulated in LDs and was present in the lipid-rich cellular area around the nucleus. Extracted Raman spectra from the same area (an LD) when measured with

low and high laser power demonstrated AXT bands (in the former) and lipids bands (in the latter) (Figure 10.3G).

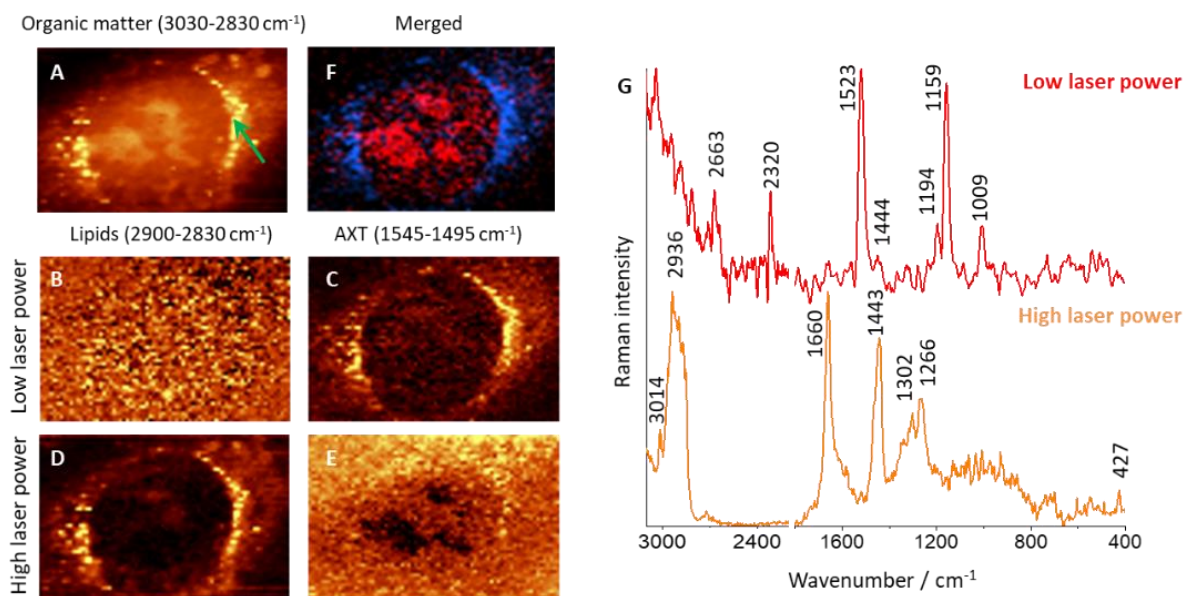


Figure 10.3. AXT shows colocalization with lipids in ECs. (A) Raman images of organic compounds (3030-2830 cm⁻¹) with the arrow indication the area from which the spectra in (G) were obtained. (B and C) Raman images of lipids (2900-2830 cm⁻¹) and AXT (1545-1495 cm⁻¹) were obtained using low (3 mW) laser power. (D and E) Raman images of lipids were obtained using high (30 mW) laser power. (F) merged image showing DNA (800-775 cm⁻¹, red) and AXT (blue) distributions. (G) extracted Raman spectra of an LD obtained using low and high laser power.

10.3.2. Live-cell imaging, the advantage of using low laser power

AXT allows visualization of lipids in ECs using laser power that is 10 times less than the one used for label-free Raman study of lipids. The benefit of using lower laser power appears when samples that are relatively fragile or that could be affected by a higher power laser are considered. Live ECs are an example of such samples which could benefit from being imaged using lower laser power. Live

imaging of AXT-labelled HMEC-1 is shown in (Figure 10.4), where AXT distribution in the cells and hence lipids distribution is displayed with good contrast.

Moreover, live cell imaging is especially beneficial when monitoring cell processes is desired. In this context, AXT holds the potential of labelling lipidic subcellular structures in live cells and monitoring changes in lipids distribution, formation of LDs changes in ER or the integrity of the nuclear envelope (e.g. during apoptosis).

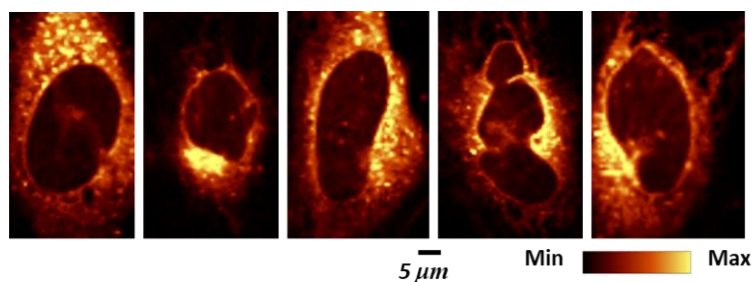


Figure 10.4. AXT allows labelled live cell imaging with low laser power. Raman images of 5 different live HMEC-1 showing the distribution of AXT ($1545\text{-}1495\text{ cm}^{-1}$) obtained using low (3 mW) laser power. Cells were pre-incubated with TNF- α (24h), then treated with AXT for 6h.

10.3.3. Visualizing the nuclear envelope

To confirm that AXT accumulates in the nuclear membrane and allows its visualization, 3D Raman imaging-based depth profiling of AXT-labelled HMEC-1 was carried out. (Figure 10.5) shows 3D Raman imaging of the area around the cell nucleus, where the lipid-rich nuclear membrane is located. The images (Figure 10.5A and B) constructed by the integration of the Raman spectra to show the distribution of AXT indicate that AXT indeed accumulated in the area around the nucleus attributed to the nuclear envelope. While offering a tool for visualizing LDs and ER in EC samples, visualizing the nuclear membrane is another advantage for AXT-labelling, a feature that could not be achieved using label-free Raman imaging techniques.

It is noteworthy that the isolation of the signal of AXT originating from its accumulation in the nuclear envelope, and the ones from LDs or ER is difficult. Figure 10.5C shows the isolated Raman spectrum of the AXT characteristic band at ca. 1520 cm^{-1} from the nuclear envelope and LDs. The signal from the nuclear envelope was slightly wider with shoulders, with its peak at ca. 1522 cm^{-1} . Whereas, the Raman bands extracted from LDs had a peak at ca. 1524 cm^{-1} . Importantly, such distinction requires further investigation such as spectral modelling.

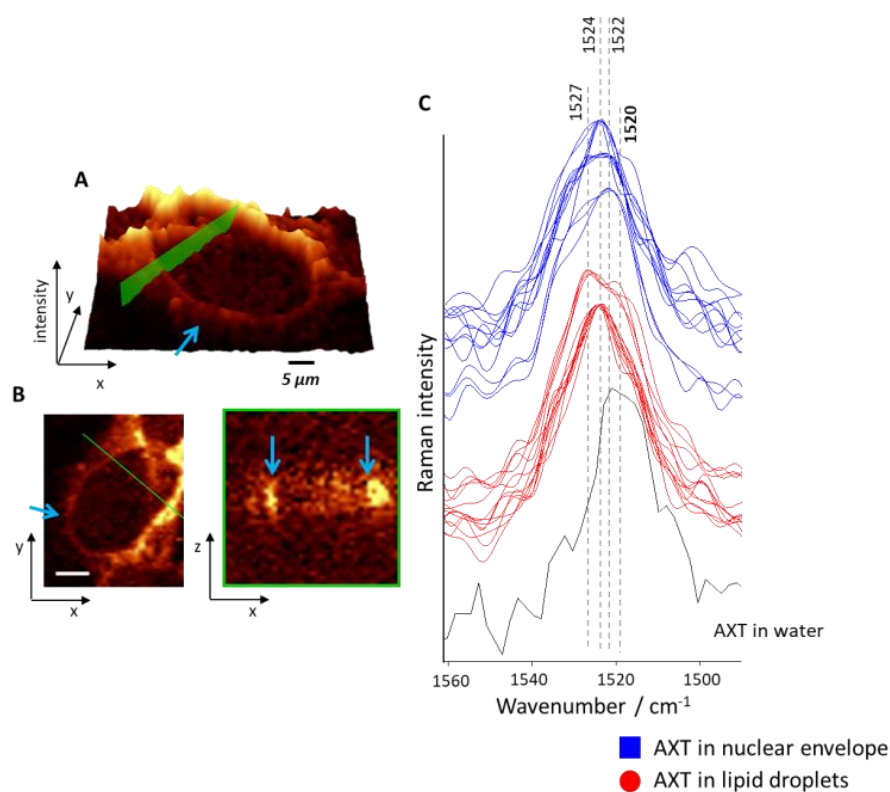


Figure 10.5. AXT allows visualizing the nuclear membrane of ECs, revealed by 3D Raman imaging. (A) Raman images showing intensity projection of AXT marker band at ca. 1520 cm^{-1} in the xy plane of an HMEC-1 pre-incubated with TNF- α (24h) and labelled with AXT (3h). (B) Imaging of the section indicated by the green line constructed from layers in the z-direction with $1\text{ }\mu\text{m}$ step size. (C) Characteristic AXT band at ca. 1520 cm^{-1} from AXT in DMSO and water (grey), LDs (red) and the nuclear envelope (blue).

10.3.4. Astaxanthin as an anti-inflammatory agent

One of the widely used markers used to study ECs inflammation is the overexpression of the intracellular adhesion molecule ICAM-1. To assess whether or not AXT contributes to ECs inflammation, fluorescence microscopy was used to measure ICAM-1 expression in HMEC-1 in the presence or absence of TNF- α pre-treatment. Figure 10.6 shows a significantly higher expression of ICAM-1 in the group of cells incubated with TNF- α for 24h. This pro-inflammatory effect is attenuated when TNF- α incubation is preceded (labelled AXT + TNF- α) or followed by AXT treatment (labelled TNF- α + AXT), with no significant change in the expression of ICAM-1 between these two conditions.

AXT incubation alone did not contribute to ECs inflammation, which is a useful quality when considering a new molecular probe, as it is desirable for it to not exert harmful or proinflammatory effects on the samples. Interestingly, while AXT treatment decreased ICAM-1 expression in ECs, it did not cause significant changes to the LDs content of the cells (results regarding this are presented in Chapter 12).

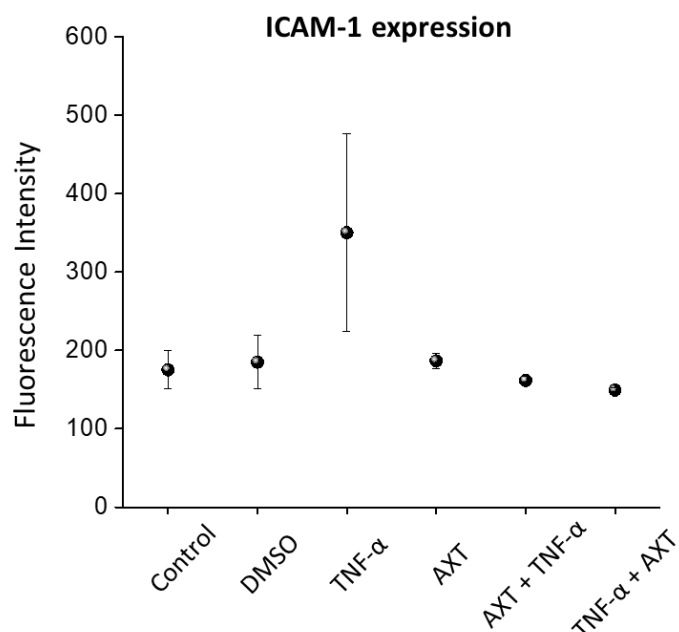


Figure 10.6. AXT anti-inflammatory effect on HMEC-1, a fluorescence microscopy quantification of ICAM-1 expression. ICAM-1 expression per cell in HMEC-1 presented as means \pm SEM for the groups: control (untreated), DMSO (cells incubated with the solvent used for AXT), TNF- α (24h), AXT (3h), and AXT treated groups before and after TNF- α incubation.

10.4. Conclusions

This chapter presented AXT as a novel Raman probe for lipidic subcellular structures in ECs. Specifically, AXT labelling could provide information on the distribution of LDs, ER and the nuclear envelope while using relatively low (3 mW) laser power to excite the samples. This is especially beneficial for live ECs imaging and when imaging biological processes such as LDs formation or changes in the integrity of the nuclear membrane such as during apoptosis. Furthermore, the effects of the pre-incubation with the pro-inflammatory cytokine TNF- α on the distribution of LDs in ECs were studied using AXT labelling.

In both healthy and inflamed ECs, AXT demonstrated a colocalization with areas in the cells attributed to LDs, and ER. Moreover, the accumulation of AXT in the area around the cell nucleus was attributed to the nuclear envelope. AXT showed a time-dependent accumulation in the lipidic structures in the cells where AXT-labelled Raman imaging could be used for the visualization of LDs solely at the shortest incubation time (30 min), LDs and ER after being subjected to AXT labelling for 1h or LDs, ER and the nuclear envelope for longer (3 and 6h) incubation times. Finally, AXT does not contribute to the inflammation of ECs.

Altogether, AXT labelling is a novel approach to Raman imaging of lipids in ECs that proposes an alternative or a complementary technique to label-free Raman imaging of lipids, opening the door for future directions with great potential. An example of that could be benefiting from AXT's resonantly enhanced signal for fast detection of intracellular lipids using techniques such as SRS or CARS.

11. Astaxanthin as a Raman probe for lipids in endothelial cells of different origins.

Part of the results reported in this chapter, obtained during the completion of the PhD thesis, are already published and are available under Ref. [57]

“**Radwan, B.**; Adamczyk, A.; Tott, S.; Czamara, K.; Kaminska, K.; Matuszyk, E.; Baranska, M. Labeled vs. Label-Free Raman Imaging of Lipids in Endothelial Cells of Various Origins. *Molecules* **2020**, *25* (23), 5752”.

Transient absorption microscopy measurements were done in collaboration with researchers from the Leibniz Institute of Photonic Technology (Leibniz-IPHT), under the framework of LogicLab ITN. Results are reported in Ref. [159]

“Yang, T.; Chettri, A.; **Radwan, B.**; Matuszyk, E.; Baranska, M.; Dietzek, B. Monitoring Excited-State Relaxation in a Molecular Marker in Live Cells—a Case Study on Astaxanthin. *Chem. Commun.* **2021**, *57* (52), 6392–6395”.

11.1. Objectives of the study

Although they form a continuous monolayer of cells, ECs are considerably heterogenous, showing differences depending on their local environments and the organs from which they originate. This chapter aims to assess AXT as a universal Raman probe for lipids in ECs of various organelles. Moreover, the label-free Raman imaging of lipids is compared to the previously presented AXT-labelled approach to image lipids in ECs showing the advantages and limitations of each method. Finally, the excited state dynamics of AXT in live cells are studied to determine whether or not AXT exists in a conjugated form within cellular lipids.

11.2. Materials and methods

11.2.1. Cell culture

For this work, three different endothelial cell lines were used; Primary HAoEC, HCAEC and HBEC-5i to represent ECs from three different organs; the aorta, the heart and the brain, respectively.

The HAoEC and HCAEC cell lines were cultured in a complete EGM-2MV medium that contained various supplements, including L-glutamine (10 mM), hydrocortisone (1 $\mu\text{g}/\text{mL}$), EGF (10 mg/mL), FBS (10%), and antibiotics (1%). HBEC-5i cells were cultured in DMEM: F12 medium supplemented with FBS (10%), antibiotics (1%), and endothelial cell growth supplement (40 $\mu\text{g}/\text{ml}$). All cells were incubated in a humidified cell culture incubator at 37°C and 5% CO_2 . For Raman measurements, cells were seeded on CaF_2 slides and allowed to reach optimal confluency overnight. A group of cells was pre-treated with $\text{TNF-}\alpha$ to induce inflammation, while the other cells were incubated with their respective medium. Cells were then treated with AXT for varying durations, fixed using

11.2.2. Raman imaging

Raman imaging was carried out using a “WITec alpha 300 Confocal Raman Imaging system” with a 532 nm excitation laser and a 60x water immersion objective (Nikon Fluor, NA = 1.0). Measurements were done twice with low and high laser powers (similar to the previous chapter), and integration time and step size were set at 0.5 s and 0.5 μm , respectively.

11.2.3. Transient absorption microscopy

MCF-7 cells were incubated in RPMI 1640 medium with FBS (10%) and antibiotics (1%), and treated with AXT for 24h before being washed with PBS. Afterwards, cells were incubated with AXT (10 μM) for 24h and washed with PBS. Cells were

either fixed with 4% formaldehyde (Carl Roth, Germany) or were subjected to transient absorption microscopy measurements directly. The transient absorption spectroscopy instrumentation was demonstrated in detail in Ref [160], and the transient absorption microscopy setup for obtaining the excited-state kinetics of AXT in cells in Ref [161].

11.2.4. Data analysis

Raman spectra obtained from all samples were processed by a routine cosmic ray removal and were baseline corrected using auto-polynomial of degree 3 (“WITec Project Plus” software). Cluster analysis (CA) was performed with the k-means method (k-means cluster analysis, KMCA) using the Manhattan distance was utilized to obtain spectra of the cells. Origin Pro 2020b (OriginLab Corporation) software was used for normalizing and presenting the spectra. Cell spectra were obtained by averaging at least 5 different cells (n=5) from each group and presented with their respective standard deviations (SD).

11.3. Results and discussion

11.3.1. Label-free vs astaxanthin-labelled Raman imaging of endothelial cell lipids

To assess the two approaches to imaging lipids in ECs i.e. label-free Raman imaging of lipids compared to the newly presented AXT labelling-based Raman imaging of lipids in ECs, every cell measurement was done twice; first using low (ca. 3 mW) and then using high (ca. 30 mW) laser power. In the AXT-labelled cell, low laser power provided the distribution of AXT in the cells, based on the relative intensity of AXT marker Raman bant at ca. 1520 cm^{-1} . AXT distribution was used as an indicator of the distribution of different lipidic structures in the cells i.e. LDs, ER and the nuclear envelope. AXT intracellular distribution could be imaged using a laser power which is 10 times lower than the one used for label-free Raman

imaging using the same instrumentation (mentioned in the materials and methods part).

Figure 11.1 demonstrates the two approaches; AXT-labelling allows imaging ECs lipids with relatively low laser power, producing good contrast images and providing information not possible to obtain with label-free technique (imaging the nuclear membrane). Whereas, label-free Raman imaging could provide information on the ECs lipids composition i.e. the unsaturation of lipids in the cell by following the characteristic band for the =C–H stretching vibration at ca. 3015 cm^{-1} .

Since inducing inflammation caused by incubation with the pro-inflammatory cytokines such as TNF- α results in an increase in LDs, especially with unsaturated characteristics, both the distribution of LDs and their degree of unsaturation could be considered key information in determining the inflammatory state of ECs.

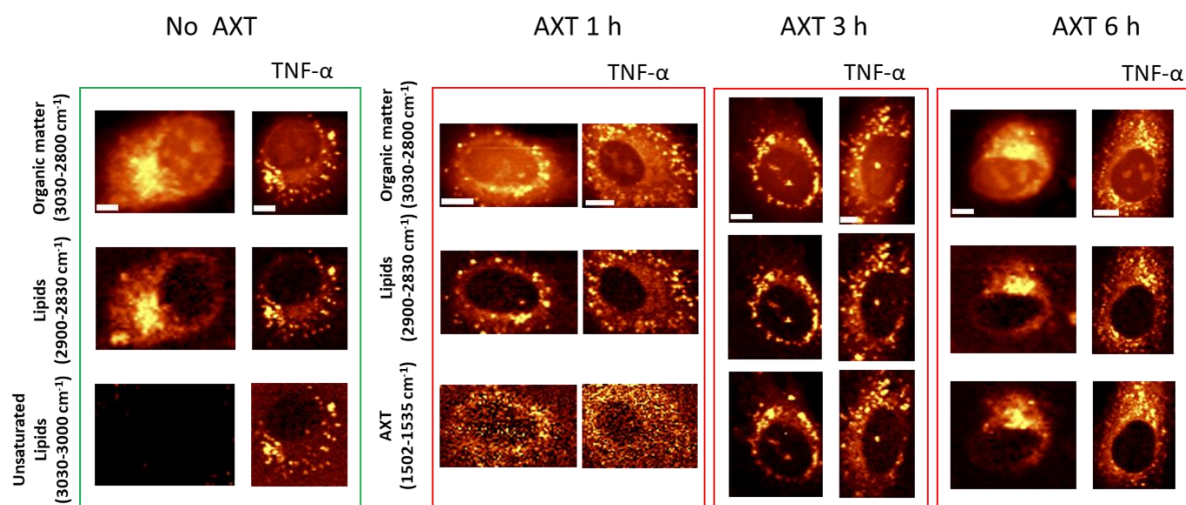


Figure 11.1. Label-free vs AXT-labelled Raman imaging of lipids in ECs. Raman images of HAOEC with and without TNF- α pre-treatment (24h) and incubated with AXT for 0 (no AXT), 1, 3 or 6h, showing the distribution of organic matter, lipids, unsaturated lipids or AXT by Raman spectral integration at the spectral regions mentioned in the figure.

To assess the spectral differences between the normal and inflamed states of ECs from different origins; namely ECs from the aorta (HAoEC), from the heart (HCAEC), and from the brain (HBEC), averaged cell spectra from each group were extracted using K-means cluster analysis (KMCA). The spectra presented in (Figure 11.2) showed that there is not significant difference appearing between the different cell lines. However, cells that were pre-treated with TNF- α for 24 hours showed an increased signal in the marker band for lipids unsaturation at ca. 3015 cm^{-1} . This alteration in the cellular lipids composition was apparent in HAoEC, HCAEC and HBEC similarly.

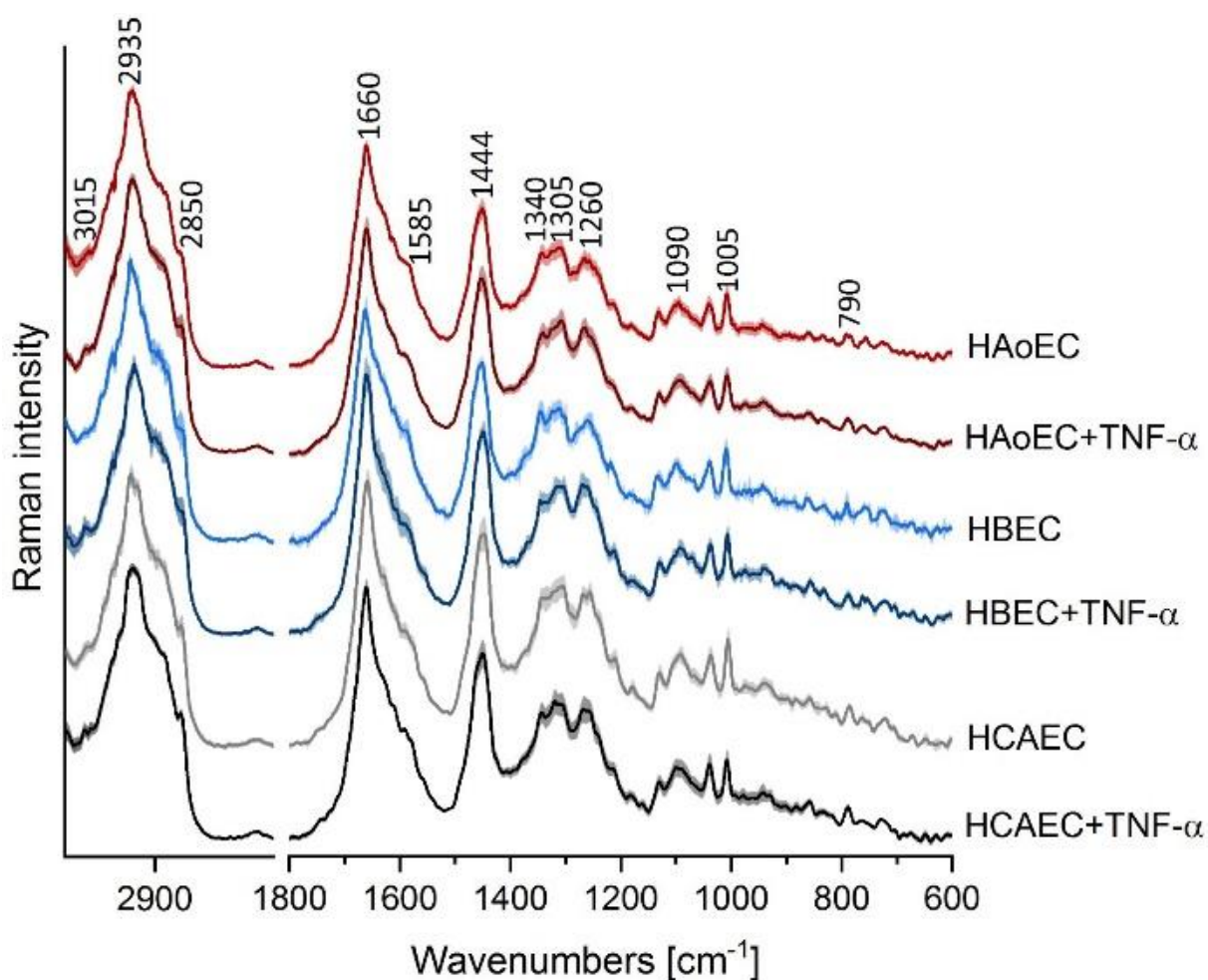


Figure 11.2. Spectral profiling of different ECs in normal and inflamed conditions. Raman spectra (presented as averaged spectra \pm SD) of HAoEC (red), HBEC-5i (blue) and

HCAEC (grey) with the TNF- α treated inflamed cells spectra presented in the respective darker colour.

11.3.2. Astaxanthin visualizing lipids in endothelial cells of different vascular beds

ECs from different organs may present changed uptake or metabolic activities for different molecules based on the high degree of heterogeneity they possess. In the last chapter, AXT was presented as a Raman probe for lipids in HMEC-1, the ECs from human microvasculature. Here, three different cell lines from the aorta, heart and brain (HAoEC, HCAEC and HBEC-5i, respectively) were selected to assess AXT labelling as a Raman probe of lipids in ECs from different organs.

Figure 11.3 presents the distribution of AXT and of cellular lipids after 0 (control), 1, 3 or 6h of being subjected to AXT labelling (incubating cells with AXT in their cell culture media). Cells in their normal conditions (Figure 11.3A) demonstrated an overall lower number of LDs compared to cells pre-treated with TNF- α to induce inflammation (shown in Figure 11.3B). Overall, there are no significant differences in cells' response to pro-inflammatory treatment, with all three cell lines showing increased numbers of LDs after being subjected to TNF- α pre-treatment.

Furthermore, the three different cell lines show similar uptake of AXT. The AXT-labelled Raman imaging of lipids in HAoEC, HCAEC and HBEC followed similar trends such as; AXT accumulated in the lipid-rich area of the cells cytoplasm in a time-dependent manner, demonstrating at first accumulation in LDs (after being treated with AXT for 1h), then less lipidic structures (ER and the nuclear envelope) for longer (3 and 6h) incubation times. Intracellular AXT content appeared to be dependent on cellular lipids content as with increased intracellular lipids (in inflamed cells presented in Figure 11.3B) AXT showed increased accumulation in cells and improved contrast of the intensity images.

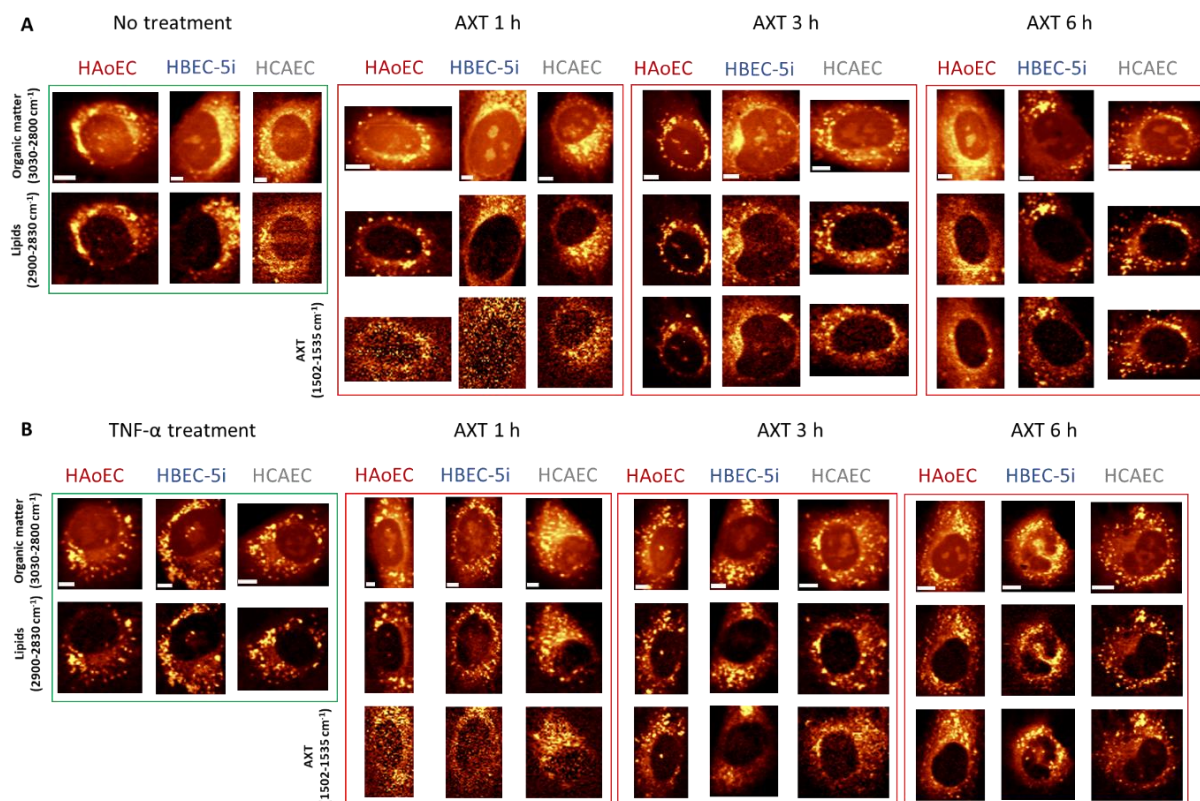


Figure 11.3. Assessment of AXT as a molecular Raman probe for lipids in ECs of various origins. Raman images of normal (A) and inflamed ($\text{TNF-}\alpha$ -pre-treated) cells (B) of HAoEC, HBEC-5i and HCAEC visualizing the distribution of organic matter ($3030\text{--}2800\text{ cm}^{-1}$), lipids ($2900\text{--}2830\text{ cm}^{-1}$) and AXT ($1535\text{--}1502\text{ cm}^{-1}$). Scale bars indicated at each image equal $5\text{ }\mu\text{m}$.

11.3.3. Does astaxanthin exist in isolated or aggregated form in cellular lipids?

Complementary information from transient absorption microscopy

Previously presented Raman data (see Figure 10.1) demonstrated a shift observed in the characteristic Raman band of AXT when it appeared in different environments; i.e. AXT showed a band at 1517 cm^{-1} in the solid state compared to when AXT was dissolved in castor oil or ECs lipid droplets (demonstrated a band at 1520 cm^{-1}). This slight shift observed with Raman spectroscopy could indicate that AXT might exist in the aggregated form in cellular lipids. However, such a conclusion needed to be confirmed or disputed using another technique.

Transient absorption microscopy was used to study the excited state dynamics of AXT in solution (DMSO) as well as in live and fixed cell samples. Firstly, transient absorption spectra of AXT (in DMSO) were collected upon excitation of its S_2 state at 510 nm to determine the suitable conditions for the measurement of the excited-state dynamics of AXT in cells. As shown in (Figure 11.4A), a strong excited-state absorption was detected between 545 and 780 nm, leading to the consideration of the probe-wavelength of 625 nm for the transient absorption microscope measurements in cells.

The intracellular distribution of AXT is shown in (Figure 11.4B), similarly to Raman data (although Raman imaging presented much-improved contrast) AXT is shown to accumulate in the lipid-rich areas around the nucleus. Finally, the S_1 lifetimes of AXT were determined in DMSO, fixed and live cells (Figure 11.4C) to be 5.3, 5.3 and 5.7 ps, respectively. This similarity in the lifetime of AXT in cells and DMSO solution demonstrated that the transient absorption signal of AXT in cells comes from isolated AXT, as AXT aggregates have significantly longer S_1 states^{162,163}.

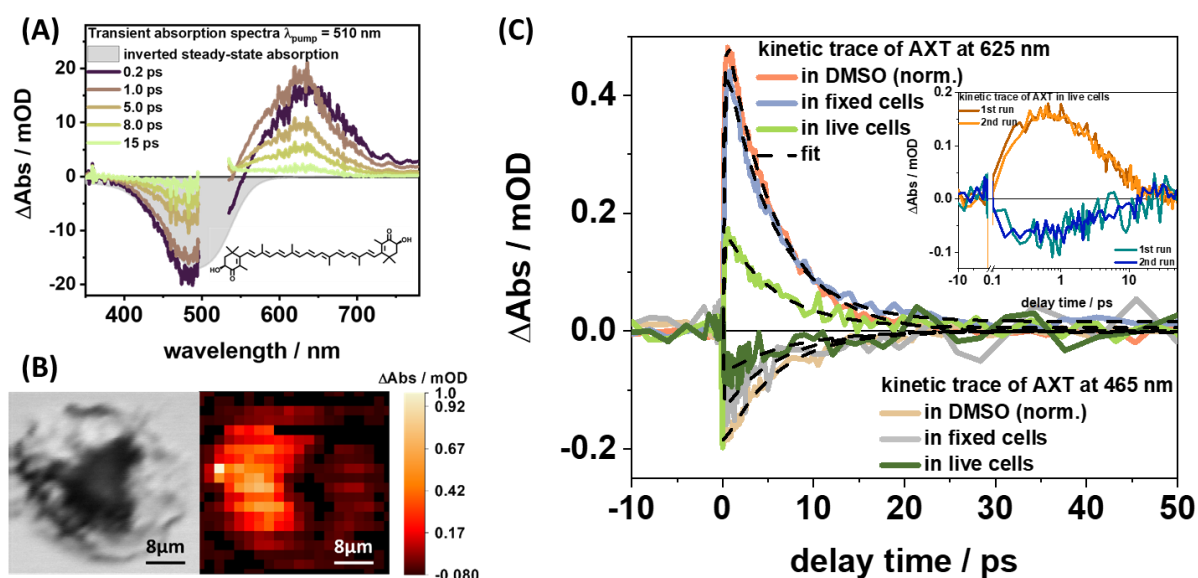


Figure 11.4. Transient absorption microscopy revealed that AXT does not aggregate in cells' lipids. (A) Transient absorption spectra of AXT in DMSO (pump wavelength =

510 nm) at the delay times of (0.2, 1.0, 5.0, 8.0 and 15 ps) with the spectrum of filled and scale-inverted steady-state absorption referencing ground-state bleaching. **(B)** Phase image and transient absorption microscope image (pump and probe wavelengths = 470 and 625, respectively) of an MCF7 cell. **(C)** The kinetic traces of AXT in solvent (DMSO), fixed and live cells with the insert showing the spectra from the first and second runs of the experiment. The figure is adapted from Ref. [159] with the permission of the Royal Society of Chemistry.

11.4. Conclusions

This chapter presented the label-free compared to the AXT-labelled Raman imaging approaches to identify lipids distribution in ECs of various origins. Imaging of lipids using label-free Raman microscopy could shed the light on key biochemical aspects relating to the composition of LDs in the cells, such as the distribution of unsaturated lipids and it allows the acquisition of the spectral profiles of intracellular lipids. Whereas AXT serving as a Raman probe for lipids in ECs allows imaging of lipid-rich subcellular structures (LDs and ER) in a time-dependent manner, moreover, AXT allows the visualization of the nuclear envelope, which is not possible using the label-free approach. It is also worth noting that in cases where higher laser power could negatively affect the samples (for more fragile samples such as live ECs), AXT allows visualization of ECs lipids using laser power 10 times lower than the one used for label-free imaging.

AXT demonstrated similar uptake by ECs from different organs i.e. the aorta, heart and brain (HAoEC, HCAEC and HBEC-5i, respectively). AXT accumulated in the lipids of ECs from different organs in a time-dependent manner. Moreover, AXT showed an increased accumulation when the intracellular lipid content increased i.e. in inflamed ECs where an increase in the number of LDs is observed due to altered lipids content. These results show the great potential of AXT to be considered as a universal Raman probe for ECs lipids regardless of their origins.

Finally, the transient absorption microscopy data clarified that AXT existed in the isolated form as opposed to forming aggregates in the lipids of cells, complementing the Raman imaging information on the state in which AXT is situated in cells.

12. Astaxanthin uptake by endothelial cells in free and encapsulated conditions

The results reported in this chapter have not been previously published elsewhere, however, a manuscript presenting part of the results is already submitted to the journal.

Radwan, B.; Prabhakaran, A.; Rocchetti, S.; Matuszyk, E.; Keyes, T. E.; Baranska, M. Uptake and anti-inflammatory effect of liposomal astaxanthin on endothelial cells studied by Raman imaging (Submitted to *Chemical Communications*, Elsevier)

Part of the results reported in this chapter, obtained during the completion of the PhD thesis, was presented in an international conference Ref. [164]

“**Radwan, B.;** Matuszyk, E.; Rocchetti, S.; Prabhakaran, A.; Keyes, T. E.; Baranska, M. Multimodal Imaging of Endothelial Pathology Models in Vitro and Ex Vivo. In *the 7th International Conference on Molecular Sensors and Molecular Logic Gates (MSMLG 2022)*; Dublin, Ireland, **2022**”.

12.1. Objectives of this study

In this chapter, the aim is to follow ECs uptake of free and encapsulated AXT using Raman microscopy. Furthermore, this study aims to investigate the effects of AXT and AXT-loaded neutral liposomes, and cationic lipoplexes on inflammatory ECs and the resulting alterations in lipids distribution and composition. This would ideally shed the light on the potential of bimodal (Raman and fluorescence) imaging to investigate cellular uptake and anti-inflammatory effects of relatively small molecules, specifically the newly established Raman probe for lipids AXT, in its free and encapsulated forms.

12.2. Materials and methods

12.2.1. Preparation of astaxanthin-loaded liposomes and lipoplexes

Liposomes and lipoplexes were prepared by the hydration extrusion method followed by the reconstitution of AXT. DPPC (1,2-dipalmitoyl-sn-glycero-3-phosphocholine) lipid was used for the preparation of liposomes and a mixture of DOPE/DOTAP (1,2-dioleoyl-sn-glycero-3-phosphoethanolamine and 1,2-dioleoyl-3-trimethylammonium-propane) was used for lipoplex preparation. The chloroform solution of the lipid was dried under nitrogen flow to get a lipid film in a 1.5 mL glass vial and it was kept under a high vacuum for 30 min to ensure the complete removal of the solvent. The lipid film was hydrated with 1 mL phosphate buffer saline of pH 7.4 and vortexed for 60 s to get the suspension of lipid in the buffer. This suspension was extruded at least 11 times through a polycarbonate membrane of 100 nm. 10 μ M AXT was reconstituted into the liposomes/lipoplexes by 30 min incubation. Any unbound AXT was removed by 5 hours of dialysis using a pur-A-lyzer kit. DPPC was extruded at 45 °C, above the phase transition temperature.

The hydrodynamic diameters of the samples were measured using dynamic light scattering (DLS) on Malvern Zetasizer Ultra. UV-vis spectra were measured using Jasco V670 UV/Vis spectrophotometer, and fluorescence was measured in quartz cuvettes of 1 cm pathlength (Varian Cary Eclipse spectrophotometer).

12.2.2. Cell culture

For subsequent Raman measurements, primary HAoEC were seeded on CaF₂ slides, and for fluorescence imaging, cells were seeded on glass-bottom 96-well plates to reach their optimal confluency after 24h. HAoEC were cultured in a complete EGM-2MV medium (Lonza, Basel, Switzerland) that had the following

supplementations: “10 mM L-glutamine (Gibco Life Technologies), 1 μ g/mL hydrocortisone (Sigma Aldrich), 10 mg/mL EGF (Sigma Aldrich), 10% FBS (Gibco Life Technologies) and 1% of antibiotics (streptomycin, penicillin and fungison, Gibco Life Technologies)”. Cells were either pre-treated with 10 ng/ml TNF- α (Sigma Aldrich) or kept in a fresh medium for 24h. Afterwards, cells (except for the control group) were treated with cell culture media containing 1 μ M AXT (Sigma Aldrich), dilution of liposomes or lipoplexes solutions (to reach the same AXT final concentration, 1 μ M) for 30 minutes, 1h, 3h or 24h. After AXT treatment, cells were fixed either with 2.5% glutaraldehyde for 4 minutes, kept in PBS (Gibco Life Technologies) at 4°C until Raman imaging, or fixed with 4% paraformaldehyde for 10 minutes and underwent the staining process prior to fluorescence imaging.

12.2.3. Raman imaging

Raman imaging was carried out using a “WITec alpha 300 Confocal Raman Imaging system” with a 532 nm excitation laser and a 60x water immersion objective (Nikon Fluor, NA = 1.0). An excitation $\lambda = 532$ nm using a solid-state laser was implemented in all the measurements. Each measurement was done twice; once with a laser power of 3 mW “low laser power” and once with a laser power of 30 mW “high laser power”. Low laser power measurements were done using a 0.5 s integration time and high laser power measurements were done using a 0.2 s integration time, a 0.5 μ m step size was used for both.

12.2.4. Staining and fluorescence imaging

Fixed HAoEC were permeabilized using 0.1% Triton-X 100 solution in PBS for 5 min, washed with PBS and blocked using 5% Normal Goat Serum. Afterwards, samples were incubated with ICAM-1 Monoclonal Antibody (Invitrogen, 1:250) at 4°C overnight. Then, samples were washed with PBS and stained with Alexa Fluor 647 goat-anti-mouse (Immunoresearch Laboratories, 2:600) in the dark at room

temperature for 30 minutes and then, washed with PBS. BODIPY 493/503 (Invitrogen) was used according to the manufacturer's instructions to stain neutral lipids. Finally, Hoechst 33342 (Thermo Scientific, 1:1000) was used to stain cell nuclei for 10 minutes in the dark. After washing, cells were kept in PBS and imaged immediately. The Confocal Quantitative image cytometer (CQ1, Yokogawa) was used for fluorescence imaging.

12.2.5. Data analysis

Pre-processing of all the Raman spectra was carried out using the "WITec Project Plus" software including the removal of the cosmic spikes and background correction. Afterwards, K-means clustering was done using the Manhattan distance in the same software to obtain averaged spectra of the lipids classes in each cell sample. Finally, spectra were extracted, normalized and presented using Origin 2022b Pro software.

Fluorescence images acquired after staining against ECs nuclei, neutral lipids and ICAM-1, were analysed using ImageJ (National Institutes of Health; <http://rsbweb.nih.gov/ij/>) and Columbus software. Counting the cells was based on the Hoechst signal from their respective nuclei. LDs count based on BODIPY staining and the intensity of ICAM-1 signal were calculated. Statistical significance determination was carried out using two-sample t-tests on Origin 2022b Pro software.

12.3. Results and discussion

12.3.1. Astaxanthin-loaded liposomes characterized by Raman spectroscopy

In this study, two different types of large unilamellar vesicles (LUVs) of diameter 100 nm were used; neutral liposomes of DPPC lipid (1.3623 mM in PBS, and

cationic lipoplexes of DOTAP (0.2719 mM) and DOPE (0.27726 mM in PBS). Both types of LUVs were loaded with AXT at the same concentration (10 μM). It has been previously shown that there is a slight shift in the C=C stretching Raman band of AXT from ca. 1516 cm^{-1} for the solid state to ca. 1520 cm^{-1} for AXT dissolved in lipids⁵⁷. The Raman spectra in (Figure 12.1A) demonstrate a similar shift in the mentioned band between AXT powder and when it is encapsulated in DPPC liposomes. As shown in (Figure 12.1B), AXT absorbs light in the visible range coinciding with the 532 nm laser, which is usually used for cell measurements, and thus offers pre-resonance enhancement noticeable in the Raman spectrum of AXT. Specifically, resonantly enhanced Raman bands of AXT are observed at ca. 1009, 1159 and 1520 cm^{-1} corresponding to CH_3 group wagging, C–C stretching and C=C stretching vibrations, respectively.

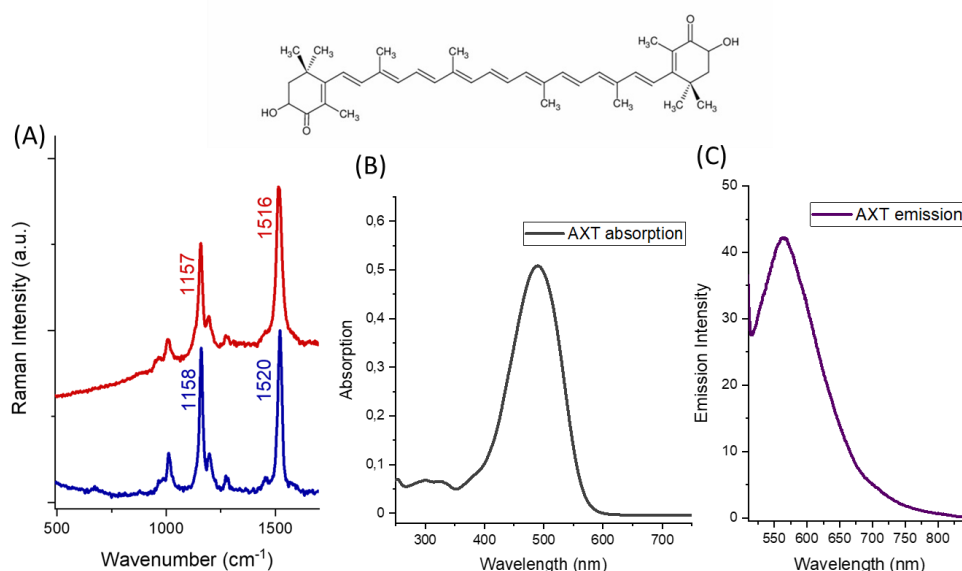


Figure 12.1. Characterization of astaxanthin-loaded liposomes. Structure of AXT and (A) Raman spectra of AXT powder (red) and in DPPC liposomes (blue). (B) The absorption spectrum of AXT in CH_3Cl . (C) The emission spectrum of AXT in CH_3Cl .

12.3.2. Time-dependent uptake of astaxanthin and astaxanthin-loaded liposomes by endothelial cells

After ECs incubation with AXT and AXT-loaded liposomes and lipoplexes using different incubation times, Raman spectra from AXT within the cells were visible only after 30 mins of incubation. As expected, AXT was present in the cytoplasm of cells, specifically in the lipid-rich cellular organelles i.e. LDs, ER and the nuclear envelope. As shown in (Figure 12.2), AXT accumulation in cellular lipids was time-dependent. At shorter incubation times (30 and 60 minutes), AXT was found in lipid-rich areas in the cytoplasm. Starting from 3h of incubation, AXT distribution demonstrates a clear colocalization with lipids in ECs, determined by comparing the Raman maps of AXT (integration of the Raman spectra around 1520 cm^{-1}) and lipids (integration of the Raman spectra around 2865 cm^{-1}).

While the uptake and distribution of free AXT did not differ much from that of encapsulated AXT, it was noticeable that positively charged lipoplexes showed an enhanced uptake by HAoEC, demonstrated by a higher intensity of AXT marker bands, compared to neutral liposomes. A similar effect has been previously reported in human corneal epithelial cells (HCECs) ¹⁴⁶.

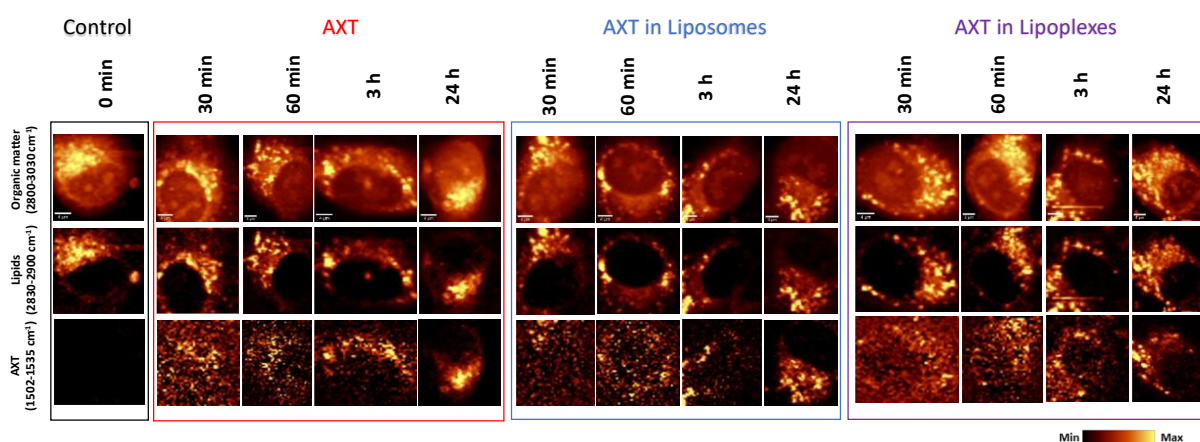


Figure 12.2. ECs uptake of AXT-loaded liposomes studied by Raman imaging. Representative images of HAoEC, control and cells incubated with AXT, AXT-loaded liposomes or lipoplexes (for 30 minutes, 1, 3 and 24 hours) constructed by integrating the Raman bands in the following spectral regions: $3030\text{-}2800\text{ cm}^{-1}$ (C-H stretching), 2900-

2830 cm^{-1} (lipids), and 1535-1502 cm^{-1} (AXT). Raman imaging was carried out once with low laser power (3 mW) to detect AXT Raman bands and once with high laser power (30 mW) to detect bands associated with lipids. Scale bars indicated on the first image of each group (3 - 5 μm).

12.3.3. Effects of liposomal encapsulation on astaxanthin anti-inflammatory activity in endothelial cells

Both the number and the composition of LDs in EC have been previously shown to change when ECs are activated using TNF- α ¹²⁷. This same effect can be seen in (Figure 12.3A); when control HAoEC is compared with TNF- α pre-treated group, a higher number of LDs are observed. Moreover, LDs in the TNF- α pre-treated group consist mostly of unsaturated lipids, evidenced by a higher intensity of the Raman band at ca. 3015 cm^{-1} (associated with the stretching modes of =C-H), which is characteristic of unsaturated lipids.

Following ECs activation, cells were incubated with AXT, AXT-loaded liposomes or AXT-loaded lipoplexes for different durations. Compared to the control, cells that were pre-incubated with TNF- α for 24h contained more LDs rich in unsaturated lipids, as shown in the third row of (Figure 12.3A). The prevalence of unsaturated LDs in inflamed cells that were later treated with AXT, either free or encapsulated, is shown to decrease, highlighting the effect of AXT in both free and encapsulated forms to attenuate the impact of TNF- α pre-treatment on ECs. Furthermore, encapsulated AXT in liposomes or lipoplexes shows a stronger effect compared to free AXT. KMCA was utilized to extract the spectra of the class of lipids in each cell. By comparing the averaged lipid spectra of each group, shown in (Figure 12.3B), a twofold increase in the intensity of the unsaturated lipids band at ca. 3015 cm^{-1} in the group of cells subjected to TNF- α pre-treatment was observed. This band is shown to decrease to the control level following incubation with AXT and AXT-loaded liposomes and lipoplexes, showcasing the capability of Raman imaging to detect AXT accumulation and the uptake of free and encapsulated AXT. Moreover,

the data indicate changes in the lipid composition of the ECs in the cases of inflammation and anti-inflammatory treatment.

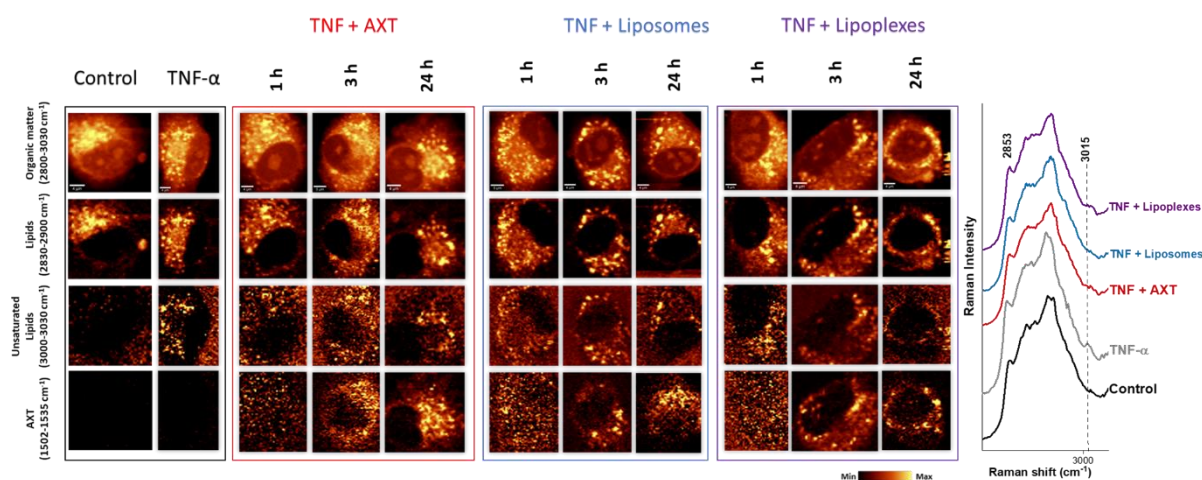


Figure 12.3. The effects of free and encapsulated AXT on activated ECs lipids, studied by Raman imaging. (A) Raman images of HAoEC, other than the control group, all the presented groups were pre-incubated with TNF- α for 24h and then incubated with AXT, AXT-loaded liposomes or lipoplexes (for 1, 3 or 24h). Pseudocolour images constructed based on the relative intensities of the Raman bands at 2800-3030 cm⁻¹, 2830-2900 cm⁻¹, 3000- 3030 cm⁻¹ and 1502-1535 cm⁻¹ (AXT), corresponding to organic matter, lipids, unsaturated lipids and AXT, respectively. Imaging was carried out once with low laser power (3 mW) to detect AXT Raman bands and once with high laser power (30 mW) to detect bands associated with lipids. Scale bar indicated on the first image of each group (3 - 5 μ m). (B) Averaged Raman spectra (high wavenumber range) of the lipids cluster of the control (black), TNF- α pre-treated group (grey), TNF- α pre-treated then incubated with AXT (red), AXT-loaded liposomes (blue) and lipoplexes (purple). n = 6 cells in each group, 3 independent experiments were performed.

To quantify the anti-inflammatory effect and changes in LDs content induced in activated ECs by AXT, AXT-loaded liposomes and lipoplexes, fluorescence imaging was utilized as a reference method. Expression of ICAM-1, a well-known marker of EC inflammation, was compared among the different groups. A significant ICAM-1 overexpression was seen following activation with TNF- α compared to control, reflected in the relative ICAM-1 expression of the TNF- α pre-treated cells which was $119.2 \pm 4.6\%$ of the control (Figure 12.4A). This

overexpression was significantly decreased to the control level when cells were treated with free or encapsulated AXT. Moreover, this anti-inflammatory effect is stronger in cells treated with AXT-loaded liposomes and lipoplexes, as the relative ICAM-1 expressions of activated EC treated with free AXT, AXT in liposomes and AXT in lipoplexes were $106.6 \pm 2.4\%$, $99.9 \pm 1.8\%$ and $100.5 \pm 2.6\%$ of the control respectively.

A significant increase in the number of LDs per cell in the group of cells incubated with TNF- α was observed (Figure 12.4B). While the number of LDs decreased after treatment with free AXT, this effect was not significant. On the other hand, when activated ECs were treated with encapsulated AXT in liposomes or lipoplexes, the number of LDs per cell decreased by 22% and 24% respectively compared to TNF- α incubated cells that were not subjected to anti-inflammatory treatment.

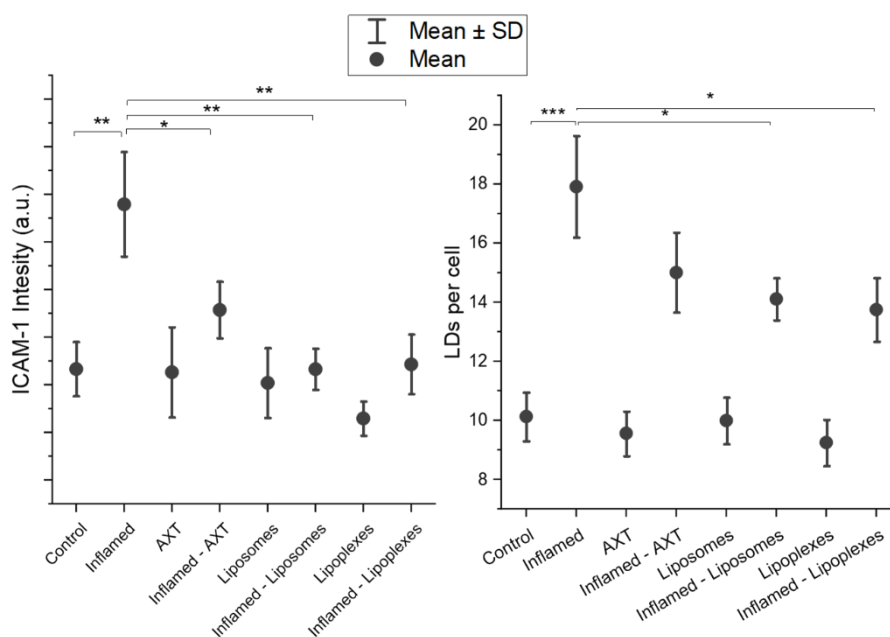


Figure 12.4. Fluorescence-based quantification of free and encapsulated AXT anti-inflammatory effects. (A) ICAM-1 expression, and (B) lipid droplets (LDs) per cell; of control, and TNF- α pre-treated groups (labelled as inflamed), that were later treated with AXT, AXT-loaded liposomes or AXT-loaded lipoplexes. The circles and whiskers represent means + SD from 3 independent experiments, * $P < 0.05$, ** $P < 0.01$ and *** $P < 0.001$.

12.4. Conclusions

The results of two complementary methods, Raman and fluorescence microscopies, clearly indicate that the anti-inflammatory effects of AXT on ECs can be enhanced by encapsulating AXT both in neutral and positively charged liposomes. Interestingly, while free AXT did indeed significantly lower ICAM-1 expression in inflamed ECs, AXT treatment did not significantly affect the number of LDs in the cells. This shows one more advantage of AXT as a Raman probe for lipids in ECs, as it attenuates the anti-inflammatory effects without significantly changing the number of LDs in cells.

This study examined the uptake of AXT encapsulated in neutral liposomes and positively charged lipoplexes by Raman microscopy with the support of fluorescence microscopy. Raman imaging provided insight into the uptake of free and encapsulated AXT by ECs in healthy and inflamed states. ECs incubated with TNF- α showed alterations in LDs composition towards more unsaturated lipids, a feature previously linked to ECs inflammation. Moreover, the anti-inflammatory effect of AXT-loaded liposomes and lipoplexes has been demonstrated by Raman imaging, highlighting a decrease in the unsaturated lipids content in activated ECs subjected to anti-inflammatory treatment.

Similarly, fluorescence imaging showed a significant anti-inflammatory effect of AXT-loaded liposomes and lipoplexes on activated ECs, manifested by a substantial decrease in ICAM-1 overexpression and the number of LDs per cell. While free AXT treatment resulted in a significant decrease of ICAM-1 expression, it did not have as significant an effect on LDs as encapsulated AXT.

In conclusion, Raman imaging provided information on AXT uptake and accumulation and changes in ECs lipid composition, whereas fluorescence imaging allowed quantification of the anti-inflammatory effects of encapsulated AXT.

13. Imaging endothelial cell proliferation and regeneration: a novel approach based on Raman imaging

Part of the results reported in this chapter, obtained during the completion of the PhD thesis, was already published and are available under Ref. [148]

“**Radwan, B.**; Rocchetti, S.; Matuszyk, E.; Sternak, M.; Stodulski, M.; Pawlowski, R.; Mlynarski, J.; Brzozowski, K.; Chlopicki, S.; Baranska, M. EdU Sensing: The Raman Way of Following Endothelial Cell Proliferation in Vitro and Ex Vivo. *Biosens. Bioelectron.* **2022**, *216* (August), 114624”.

13.1. Objectives of the study

An important aspect of ECs' function is their ability to regenerate when they are subjected to damage or injury to repair the resulting dysfunction. ED is often linked to alterations in the capacity of ECs to regenerate resulting in their inability to heal and recover. Therefore, imaging of ECs proliferation and regeneration in both in vitro and ex vivo conditions holds great importance. EdU click chemistry-based cell proliferation assay is usually the method of choice to study ECs proliferation due to its great advantages of not relying on antibodies and not requiring the vigorous step of DNA denaturation. However, it still requires the use of a copper catalyst (which is cytotoxic) and relies on fluorescent dyes that are usually not cell membrane permeable, thus requiring cell fixation and permeabilization. Alternatively, Raman detection of EdU is done in a “click-free” manner allowing live cell imaging of cell proliferation.

This chapter presents a novel Raman imaging-based approach to EdU cell proliferation assay *in vitro*, using two models of impaired cell proliferation; incubation of ECs with cycloheximide (CHX) or doxorubicin (DOX). Fluorescence imaging of EdU (stained with Alexa Fluor azide dyes) was used as a reference

method. Finally, this approach was applied to image ECs and SMC regeneration *ex vivo* in isolated mice aorta after being subjected to mechanical injury.

13.2. Materials and methods

13.2.1. Cell culture

For the *in vitro* ECs proliferation assay done using Raman and fluorescence microscopies, HMEC-1 was chosen. HMEC-1 cells were grown in a complete MCDB131 medium supplemented with 10 mM L-glutamine, 1 µg/mL hydrocortisone, 10 mg/mL EGF, 10% FBS, and an antibiotic antimycotic solution. For Raman imaging, HMEC-1, HAoEC, and HCAEC were seeded on CaF₂ slides and incubated overnight to reach optimal confluency. For fluorescence imaging, cells were cultured in 96-well plates. EdU labelling was performed by incubating cells with EdU (20 µM) for 3 or 24 hours. Cells were either subjected to live cell imaging in warmed-up PBS or fixed using 2.5% glutaraldehyde for 4 minutes and stored at 4°C before Raman imaging. To assess cell proliferation, HMEC-1 cells were preincubated with CHX in 1 or 10 µg/mL for 1 hour or incubated in fresh medium as a control. Additionally, cells were treated with DOX (0.1 – 1 µM) for 24 hours. Cells were then washed and incubated with EdU (10 – 20 µM) for 1, 3, or 24 hours. HMEC-1 cells were then washed and fixed using 2.5% glutaraldehyde for 4 minutes for Raman measurements or 4% paraformaldehyde for 10 minutes for fluorescence imaging.

EdU-labelled Raman imaging of ECs DNA was also performed in two other ECs, Primary HAoEC and HCAEC, which were both independently cultured in a complete EGM-2MV medium supplemented with 10 mM L-glutamine, 1 µg/mL hydrocortisone, 10 mg/mL EGF, 10% FBS, and 1% antibiotics. All cells were incubated in a cell culture incubator at 37 °C with 5% CO₂/95% air.

13.2.2. Aortic rings sample preparation

All experiments performed on animals mentioned in this chapter had the approval of the “Local Jagiellonian University Ethical Committee on Animal Experiments” in agreement with the “Guidelines for Animal Care and Treatment of the European Community”.

Wild type male mice (C57Bl/6) between 8 and 12 weeks were selected for this experiment. Animals were subjected to intraperitoneal injections of EdU at the dose of 150 mg/kg three times in a span of a week (every 48h). Before aortae isolation, animals were anaesthetized using xylazine and ketamine 10 mg/kg and 100 mg/kg, respectively applied intraperitoneally. The thoracic aortae samples were isolated and then moved to a Krebs–Henseleit buffer. They were cleaned from the surrounding tissue before being cut into rings of 1 to 2 mm. While the control group was left intact, a sharp object was used to induce injury to the endothelium layer in the “injured group”. Afterwards, isolated aortic rings were incubated *ex vivo* in MEM with the supplementations of “20% FBS, 1% MEM vitamins, 1% antibiotics mixture of penicillin 10,000 U/mL and streptomycin 10,000 µg/mL, and 1% non-essential amino acids” in the presence or absence of VEGF for 48h. Aortic rings were then cut open and glued to glass (for later fluorescence microscopy) or CaF₂ windows (for later Raman microscopy) measurements. Cell-Tak® was used to fix the aortic rings into the slides. Aortic rings were subjected to fixation with 4% formalin or 4% paraformaldehyde. For subsequent Raman imaging, washing with PBS after fixation and storing at 4°C was sufficient without the need for staining, while the aortic rings meant for fluorescence imaging were subjected to a staining process beforehand.

For subsequent fluorescence imaging, aortic rings were subjected to the process of immunostaining, starting with blocking with TNB blocking buffer “0.1 M Tris-HCl pH 7.5, 0.15 M NaCl, and 0.5% (w/v) blocking reagent, PerkinElmer FP1020” for 4h. Then, *en face* aortae were subjected to permeabilization with “0.5% Triton-X 100”, washed with PBS, and were subjected to the “click chemistry” reaction with Alexa Fluor® 555 azide for fluorescently labelling EdU.

After a few steps of washing with PBS, samples were subjected to incubation with anti-CD31 antibody (Abcam) in TNB blocking buffer and left at 4°C for the night. Afterwards, samples were washed with PBS and incubated with Alexa Fluor 647 goat-anti-rabbit (Immunoresearch Laboratories, 1:200) at 24°C protected from the light for 3h. Finally, Hoechst 33258 (Sigma Aldrich; 1:1000) was used to label samples' nuclei. *En face* aortae samples were covered with glass coverslips, kept away from direct light, and were imaged using CQ1 Confocal Quantitative Image Cytometer (Yokogawa). The process of the animal experiment is simplified in (Figure 13.1).

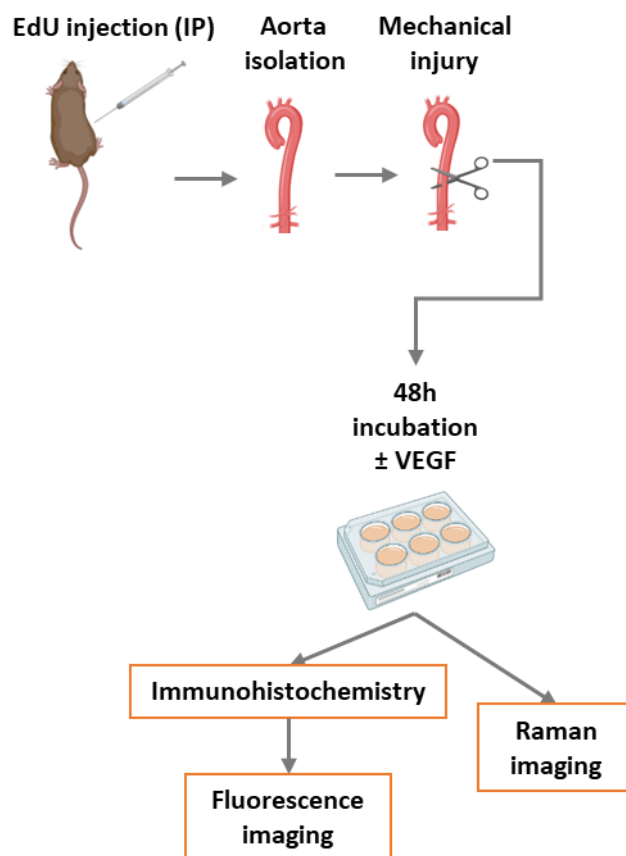


Figure 13.1. The method used for studying *ex vivo* regeneration of ECs.

13.2.3. Raman imaging

Raman measurements were conducted using a “WITec alpha 300 Confocal Raman Imaging system”. The microscope was equipped with a UHTS 300 spectrograph, a CCD camera (Andor), and a Nikon Fluor water immersive objective with an NA of 1.0. For all measurements except for those done on DOX-treated ECs, a solid-state laser with an excitation wavelength of 532 nm was used. For DOX-treated ECs, a 488 nm laser was implemented. The measurements had an integration time of 0.5 s and a step size of 0.5 μm .

To perform Raman imaging-based cell proliferation assays on a larger area, a Zeiss water immersion objective with an NA of 1.0 and a 40 \times magnification was utilized with an integration time of 0.3 s and a sampling density of 2 μm . *En face* aortae imaging was also done using the same spectrometer and a 60 \times objective with an integration time of 0.3 s.

13.2.4. EdU fluorescence labelling

To visualize the incorporation of EdU, HMEC-1 cells were incubated with the compound and then subjected to a "click chemistry" reaction, which uses fluorescent dyes to stain and image the cells. After fixing the cells, they were washed with a solution containing 3% BSA in PBS and permeabilized with 0.5% Triton-X 100, followed by additional washing with PBS. The cells were then treated with Alexa Fluor® 488 azide, CuSO_4 and Na ascorbate for 30 minutes to perform the "click chemistry" reaction, protected from light. After thoroughly washing the cells with PBS, they were stained with Hoechst 33342 to visualize the nuclei, and then washed and left in PBS for fluorescence imaging using the same cytometer as mentioned before.

13.2.5. Data analysis

To prepare the Raman spectra for analysis, pre-processing was performed using the "WITec Project Plus" software, including the removal of cosmic spikes and background correction. Afterwards, K-means clustering was done using the

Manhattan distance in the same software to obtain averaged spectra of the nuclei classes in each cell sample. Finally, spectra were extracted, normalized and presented using Origin 2022b Pro software. To assay EC proliferation based on the Raman microscopy approach, EdU-positive ECs were determined based on the presence of a band at ca. 2120 cm^{-1} , while the total number of cells was determined by Raman imaging of the DNA characteristic band at ca. 785 cm^{-1} .

Fluorescence images acquired after staining against ECs nuclei, neutral lipids and ICAM-1, were analysed using ImageJ (National Institutes of Health; <http://rsbweb.nih.gov/ij/>) and Columbus software. Counting the cells was based on the Hoechst signal from their respective nuclei. The EdU-positive cell population was determined based on Alexa Fluor-labelled EdU. Statistical significance determination was carried out using two-sample t-tests on Origin 2022b Pro software.

13.3. Results and discussion

13.3.1. EdU-labelled Raman imaging of endothelial cell DNA

Labelling ECs DNA and Raman imaging of ECs nuclei based on the detection of the most intense Raman band of EdU (its band associated with the CC vibration) presented in the spectroscopically silent region at ca. 2122 cm^{-1} (Figure 13.2A) was possible after incubation with EdU for 3h. Increased intensity of EdU characteristic Raman band and improved Raman imaging was possible upon incubation with EdU for 24h (Figure 13.2B).

Addressing the heterogeneity of ECs^{165,166}, besides ECs from microvascular ECs (HMEC-1), ECs from the aorta and coronary artery (HAoEC and HCAEC) were used. As shown in (Figure 13.2B), EdU labelling improved the Raman imaging of ECs nuclei resulting in nucleus images with better contrast compared to the Raman imaging based on the label-free detection of the DNA Raman band at ca. 788 cm^{-1} .

EdU-labelling improved Raman imaging of cell nuclei for HMEC-1, HAoEC and HCAEC independently.

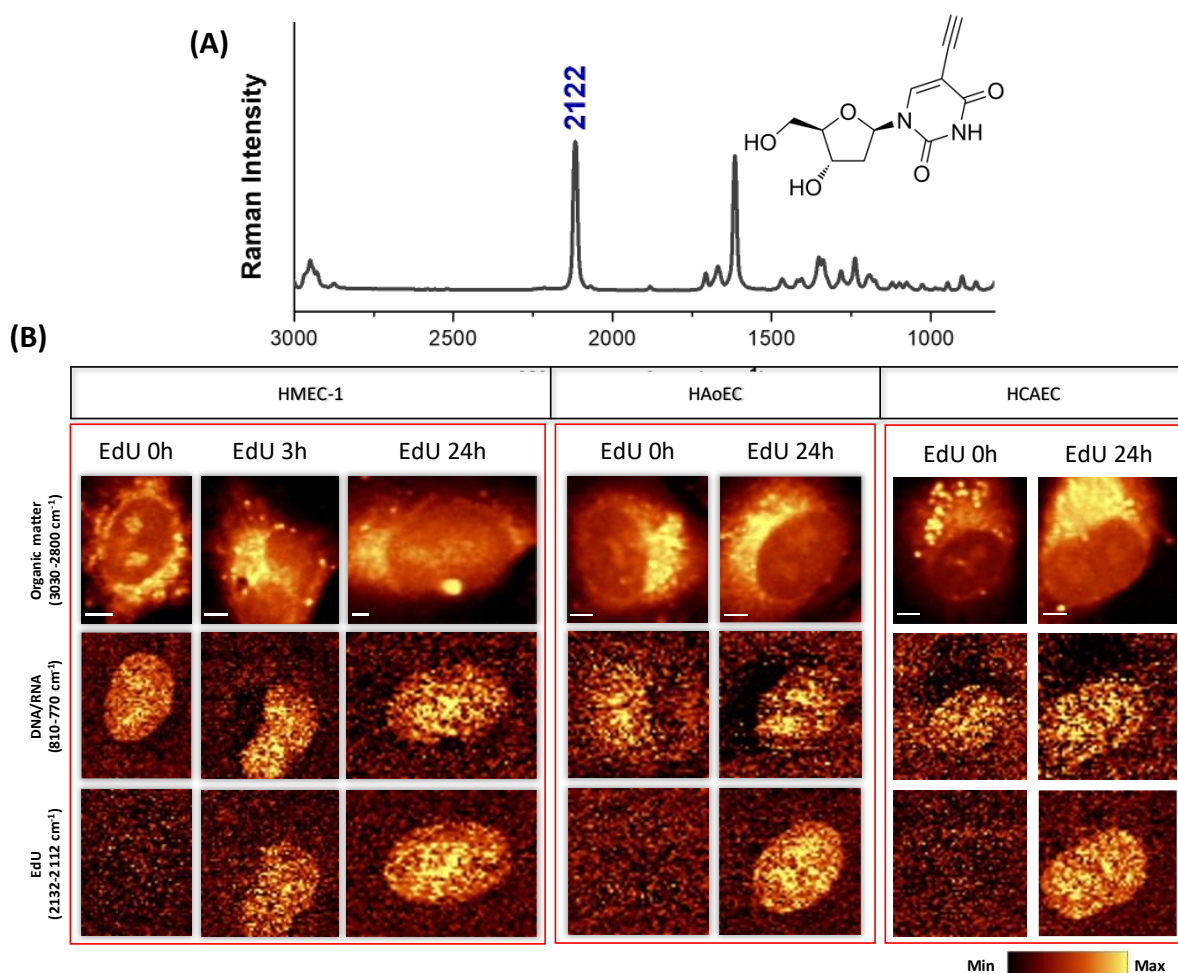


Figure 13.2. EdU-labelling improves Raman imaging of nuclei in ECs of different origins. (A) EdU's chemical structure and Raman spectrum of the pure compound. (B) Raman images of HMEC-1, HAoEC and HCAEC showing the distribution of organic matter (3030-2800 cm^{-1}), nuclei acids (810-770 cm^{-1}) and EdU (2132-2112 cm^{-1}) in ECs labelled with EdU for 0, 3 or 24h.

13.3.2. Live cell imaging, the advantage of the Raman imaging approach

As imaging live ECs presents the potential for studying underlying cellular processes associated with the development and progression of ED. Fluorescently

labelling EdU-tagged cells usually requires cell fixation to allow for the click chemistry reaction catalysed by the cytotoxic copper. However, as seen in (Figure 13.2) Raman detection of EdU could be done in a click-free manner, thus it could permit live ECs imaging. It is worth noting that fixation also causes a decrease in several Raman bands reducing the contrast of obtained images. For instance, glutaraldehyde fixation caused a decrease in the intensity of the characteristic nucleic acid bands at ca. 785 cm^{-1} and ca. 1096 cm^{-1} ¹⁶⁷. Live ECs Raman imaging was performed in HMEC-1 (Figure 13.3). EdU-labelling provided an improved image of EC nuclei (Figure 13.3A). The alkyne band of EdU localized in cell nuclei was easily detectable in the silent region of the Raman spectrum of the cell (Figure 13.3B).

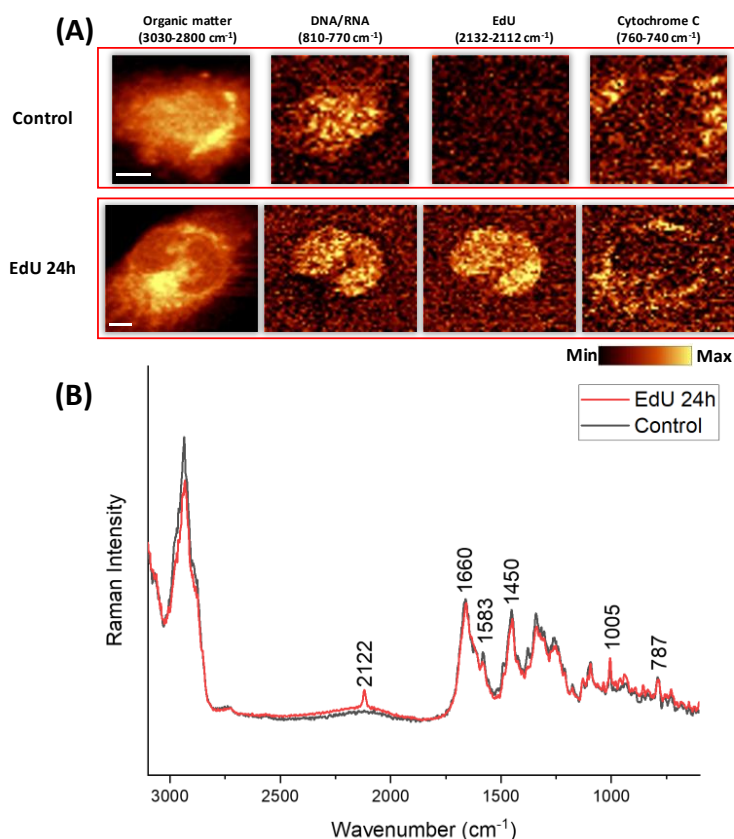


Figure 13.3. Raman-based EdU imaging could be done in live ECs. (A) Live HMEC-1 images with and without EdU labelling, showing the distribution of all organic matter, nucleic acids, EdU and cytochrome c by the integration of the

Raman spectra at the respective spectral regions presented in the figure. **(B)** Averaged Raman spectra of the nucleus of EdU-labelled (red) and control cell (grey) showing the alkyne band at 2122 cm^{-1} .

13.3.3. Endothelial cell proliferation assay based on Raman imaging, and fluorescence imaging as a reference method

To evaluate the utilization of the Raman imaging-based approach to detect changes in ECs proliferation based on EdU signal, an *in vitro* model for inhibited DNA synthesis based on pre-incubating HMEC-1 with CHX was used. CHX-treated cells have been shown to demonstrate a lower number of EdU-positive cells due to CHX inhibition of cell proliferation¹⁵⁶. Here, cells (except the control) were incubated with CHX (1 or 10 $\mu\text{g/ml}$) for 1h prior to their incubation with EdU (20 μM) for 24h. Raman images of control cells showed an apparent localization of EdU in ECs nuclei based on EdU characteristic alkyne band at ca. 2122 cm^{-1} (Figure 13.4A). A decrease in the intensity of the EdU Raman band was apparent in the groups of cells that received CHX pre-treatment, especially in the group of cells pre-treated with a higher CHX concentration (10 $\mu\text{g/ml}$) where some of the cells did not display EdU signal at all (Figure 13.4A).

Through cluster analysis with KMCA, averaged spectra from cell nuclei belonging to different groups were extracted. As presented in (Figure 13.4B) a decreased intensity of the EdU marker band at ca. 2122 cm^{-1} was apparent in the groups of cells incubated with CHX. This decrease was concentration-dependent with the group of cells that received treatment with a higher concentration of CHX (10 $\mu\text{g/ml}$) showing a greater decrease in EdU signal. Interestingly, label-free characteristic Raman bands for DNA, such as the one at ca. 788 cm^{-1} did not change with CHX treatment, thus this DNA synthesis inhibition effect exerted by CHX treatment was only detectable using the EdU-labelling approach.

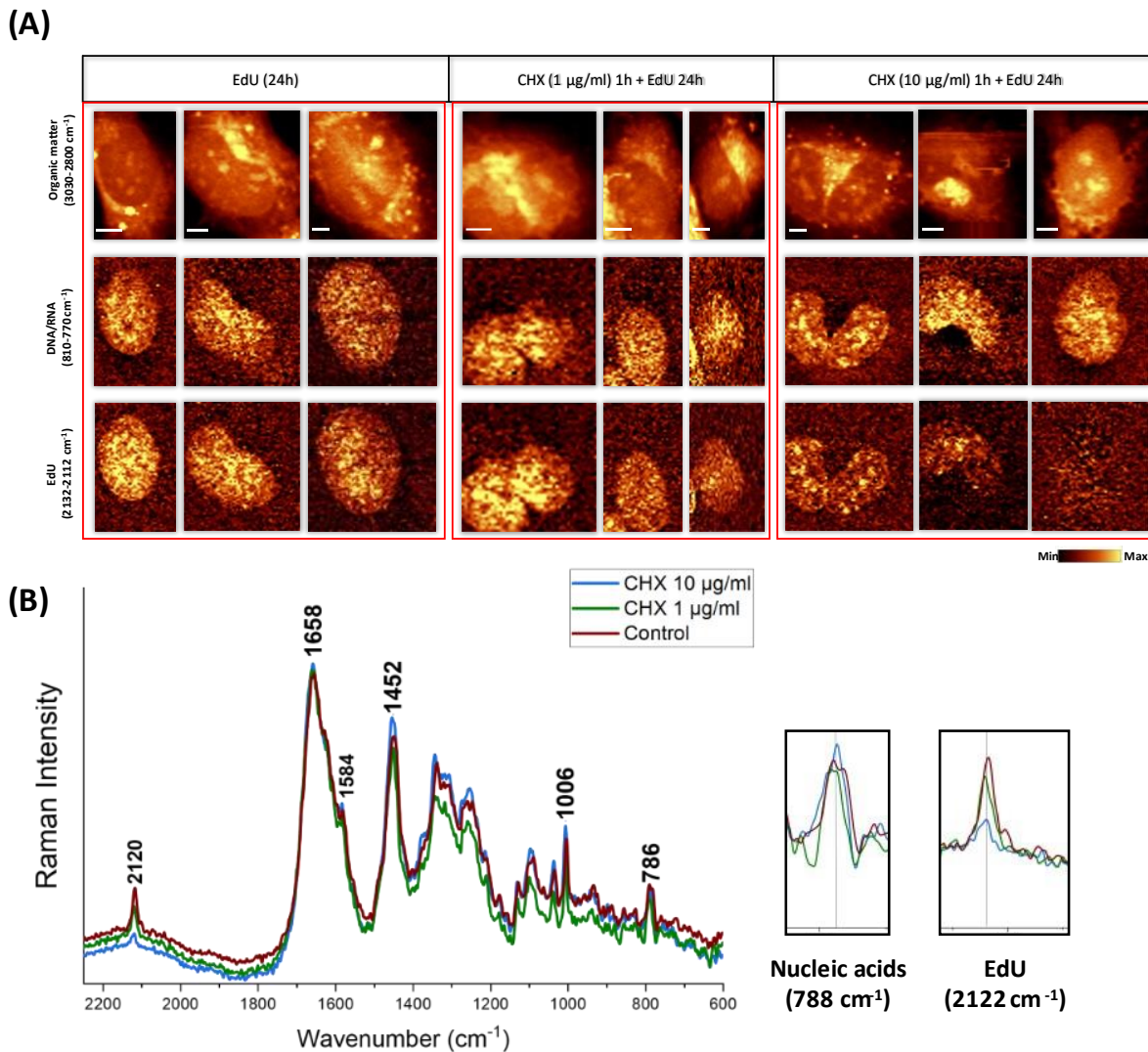


Figure 13.4. CHX pre-treatment effects on HMEC-1 studied by EdU-labelled Raman imaging (A) Raman imaging of HMEC-1 tagged with EdU that either did not receive (control) or received CHX pre-treatment at lower (1 $\mu\text{g/ml}$) and higher (10 $\mu\text{g/ml}$) concentrations, showing the distribution of all organic matter, nucleic acids, and EdU. (B) averaged spectra of the HMEC-1 nuclei class from each group. Inserts showing the DNA band at 788 cm^{-1} and the EdU band at 2122 cm^{-1} .

To apply the novel approach of EdU-labelling Raman imaging-based EC proliferation assay, quantification of the EdU-positive and EdU-negative cell population was carried out. This was performed by imaging a larger area of the cells

and judging each cell for the presence or absence of EdU signal (ca. 2122 cm^{-1}) from their respective nuclei (Figure 13.5). The characteristic DNA band that appeared in all cells despite the presence or absence of EdU was used as a reference to quantify the total number of cells. By analysing the Raman spectra and the corresponding Raman images of EdU-labelled ECs, a significant decrease in the number of EdU-positive cells was detectable in the group pre-treated with a higher concentration of CHX (10 $\mu\text{g/ml}$). Whereas, cells that received a lower concentration CHX treatment (1 $\mu\text{g/ml}$) presented a lower percentage of EdU-positive cells compared to the control but the effect was not as prominent. These results, presented in (Figure 13.5B) demonstrated that Raman imaging-based EC proliferation assay based on EdU sensing was sensitive to antiproliferative effects caused by CHX.

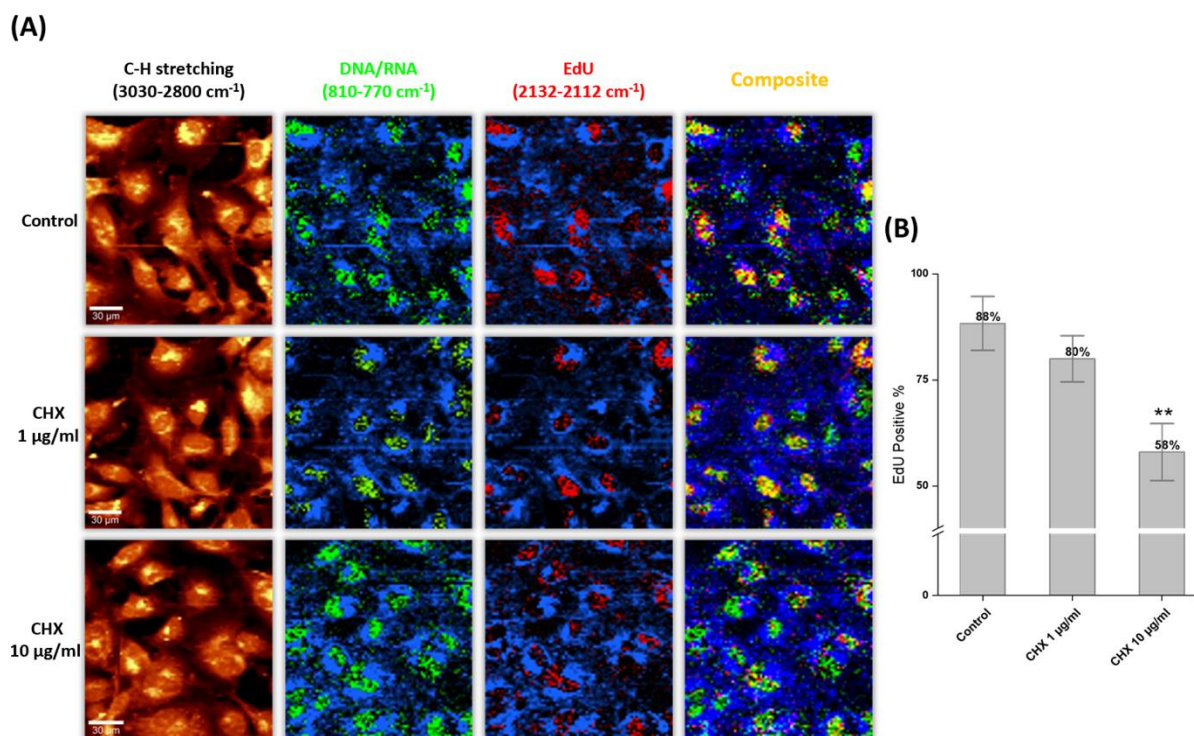


Figure 13.5. Raman imaging-based ECs proliferation assay based on EdU sensing. (A) Raman imaging of HMEC-1 labelled with EdU, that received CHX pre-treatment at 0 (control), 1 or 10 $\mu\text{g/ml}$. The images show the distributions of organic matter (blue), nucleic acids (green), EdU (red) and composite images (overlapped EdU and DNA signal in yellow), Scale bars = 30 μm . (B) EdU-positive cells (ECs expressing a band at ca. 2122

cm⁻¹) compared to all ECs (based on the label-free DNA band at ca. 788 cm⁻¹) shown as percentages (means ± SD) obtained in 3 independent experiments, n= 50 cells per group. ** P < 0.01 vs. control.

To confirm the results obtained using the presented novel approach for assaying ECs proliferation using Raman imaging, fluorescence imaging of Alexa fluor® 488-stained EdU was used in the same conditions as described earlier. Hoechst staining of all cell nuclei was used to quantify the total number of cells while the EdU-positive cell population was counted based on Alexa fluor® 488 signal. Figure 13.6A demonstrates a decrease in the EdU-positive cell population with CHX treatment, while the total number of cells is not affected. Declines in both the percentage of EdU-positive cells and the intensity of EdU (Alexa fluor® 488) were observed (Figure 13.6A and B). The decline in both signal intensity and the percentage of EdU-positive cells were significant in HMEC-1 pre-treated with the higher concentration of CHX (10 µg/ml). These results of fluorescence microscopy are in line with the results obtained from Raman microscopy based on the click-free detection of EdU.

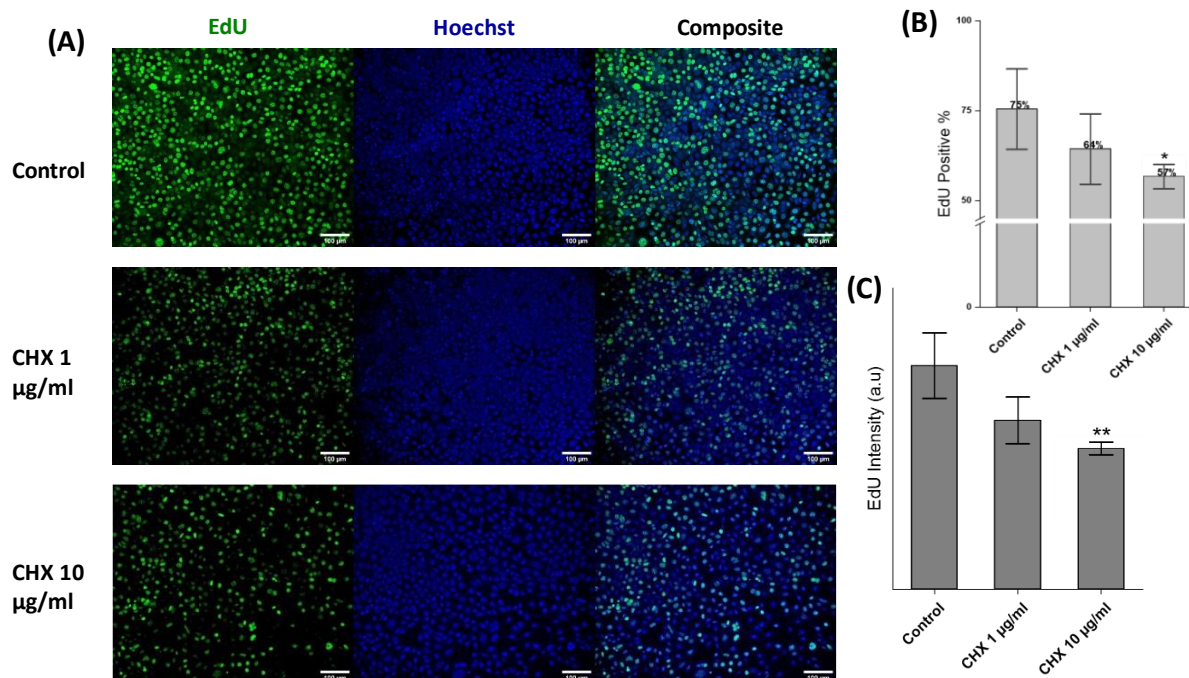


Figure 13.6. Fluorescence imaging of EdU confirms the Raman imaging results. (A) Fluorescence images showing EdU-positive HMEC-1 nuclei (green), all cell nuclei based on Hoechst staining (blue), and composite images of EdU-labelled cells that received CHX pre-treatment at 0 (control), 1 or 10 µg/ml. Scale bars = 100 µm **(B)** EdU-positive ECs percentage. **(C)** Averaged fluorescence signal intensity from Alexa fluor® 488-stained EdU. Results are presented as means ± SD, experiments were repeated 3 times, * P < 0.05, ** P < 0.01 vs. control.

13.3.4. EdU labelled Raman-based detection of doxorubicin effects on endothelial cells

Doxorubicin (DOX) has been shown to exert cytotoxic effects on ECs at the nuclear, cytosolic and membrane levels^{168–170}. A prominent feature of doxorubicin endothelial toxicity was presented in DOX accumulation in ECs nuclei causing increased nuclear area. The effect of the increased nuclear area caused by DOX accumulation in the cells could be detected using label-free Raman imaging of the nucleus (based on the DNA band at ca. 788 cm⁻¹) and by detecting the elevation of background in the high wavenumber range of the Raman spectra (ca. 4200 – 3800

cm^{-1}) caused by DOX treatment. As shown in (Figure 13.7), these effects were detectable in HMEC-1 labelled with EdU. Moreover, the effect of DOX on ECs proliferation is also presented in (Figure 13.7C). Raman imaging of EdU-labelled ECs after DOX treatment demonstrated a partial inhibition of cell proliferation when a lower concentration of DOX ($0.1 \mu\text{M}$) was used, while a complete block of cell proliferation was detected in cells treated with the higher DOX concentration ($1 \mu\text{M}$).

Interestingly, in control ECs and in ECs treated with the lower concentration of DOX ($0.1 \mu\text{M}$), EdU-labelling resulted in clear imaging of cell nuclei based on the integration of the Raman spectra around 2122 cm^{-1} , while higher DOX concentration ($1 \mu\text{M}$) impaired the signal detection due to its pronounced cytotoxicity. These results suggest that EdU-labelled Raman imaging could allow studying morphological changes in ECs nuclei as well as the detection of altered cell proliferation.

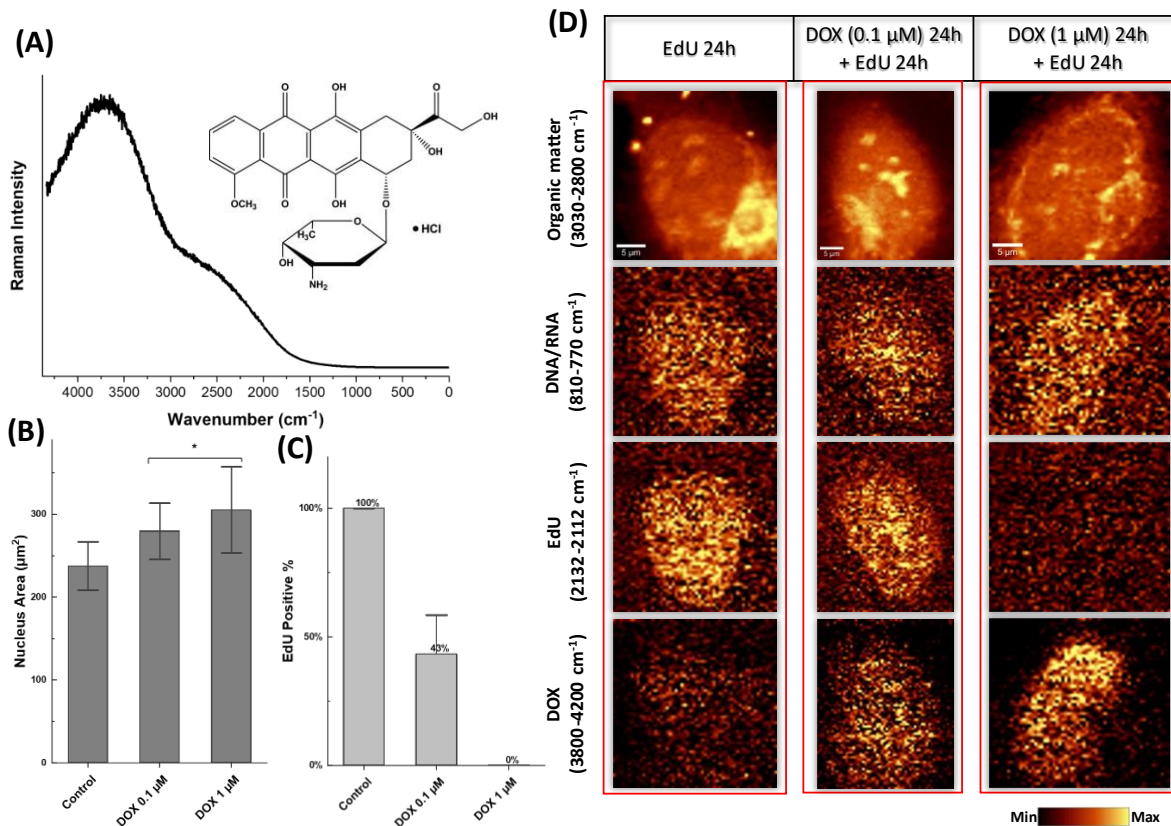


Figure 13.7. EdU-labelled Raman imaging is sensitive to Doxorubicin-induced effects on ECs. (A) Raman spectrum of DOX and its chemical structure. (B) Averaged area of the HMEC-1 nuclei in different conditions, presented as means ±SD * P < 0.05 vs. control. (C) EdU-positive HMEC-1 percentage. (D) Raman imaging of EdU-labelled control and DOX pre-treated (0.1 and 1 μM, 24h) HMEC-1 showing the distribution of organic matter, nucleic acids, EdU, and DOX (presented by an elevated spectral background in the range of 4200 – 3800 cm⁻¹). Scale bars = 5 μm.

13.3.5. *Ex vivo* imaging of endothelial cells and smooth muscle cells regeneration in the isolated murine aorta

The applicability of the Raman and fluorescence imaging-based detection of ECs regeneration, *in situ* aortic rings from isolated murine aorta were subjected to mechanical injury or left intact (control). Afterwards, aortic ring samples were incubated *ex vivo* in the presence or absence of VEGF. Following 48h of incubation with EdU, aortae samples were prepared for Raman or fluorescence imaging to

detect EdU signal and consequently ECs proliferation and regeneration following the induced mechanical injury.

As presented in (Figure 13.8A), aortic ring samples which were incubated without VEGF did not show significant EdU incorporation. Whereas, samples in VEGF-supplemented media showed a noticeable EdU signal. EdU-positive cells were mostly detected in aortic rings subjected to mechanical injury, however, they were also detected to a lesser degree in the non-injured group with VEGF supplementation. To detect if the EdU signal originated from the endothelium or the from underlying cells (e.g. smooth muscle cells, SMC), PECAM-1 (“platelet/endothelial cell adhesion molecule-1”, CD-31) immunostaining, which is widely used for ECs differentiation, was used. EdU-positive cell population constituted of both CD-31-positive cells and CD-31-negative cells that had the morphological characteristics of SMC. Therefore, both the regeneration of ECs and SMC were detected.

Raman imaging of *en face* aortae demonstrated a small number of EdU-positive cells without the need for additional staining (Figure 13.7B). Imaging of *en face* aortic rings using Raman imaging was previously demonstrated. However, the differentiation between proliferating and non-proliferating cells and studying the regenerative ability of cells in isolated aortae was only detectable by the presented EdU-labelling approach.

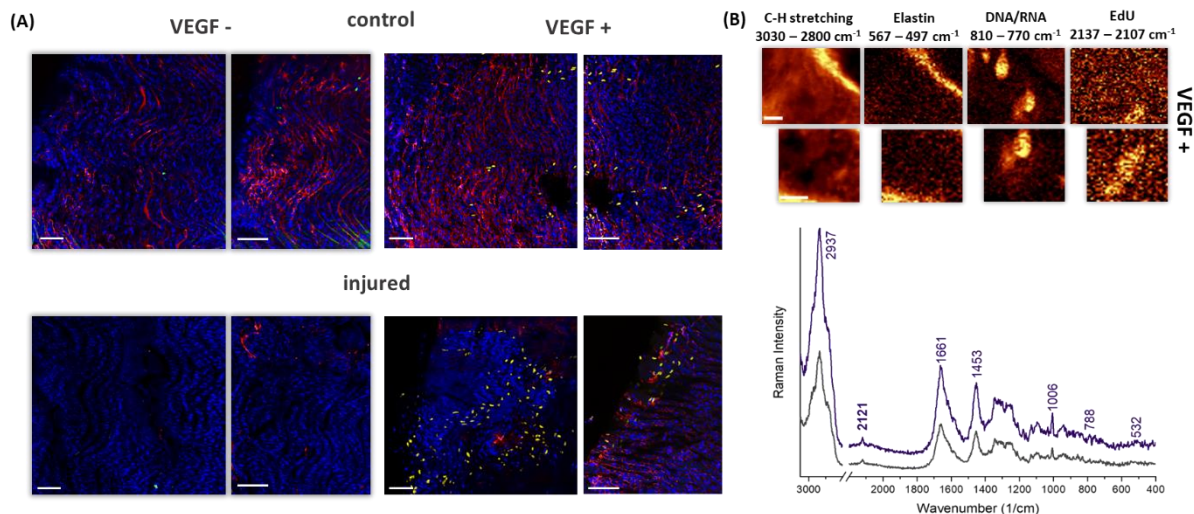


Figure 13.8. ECs regeneration in intact and injured *en face* murine aorta studied by Raman and fluorescence microscopies. (A) Fluorescence microscopy of isolated mice aortae samples with intact (control) or injured endothelium, with or without the supplementation of VEGF. Images show staining against CD31 marker for ECs (red), Hoechst (blue) and EdU (yellow). (B) Raman images of EdU-labelled *en face* aorta demonstrating the distributions of organic matter, elastin, nucleic acids and EdU (spectral regions indicated in the figure). The averaged spectra of two cells exhibiting EdU bands are shown below.

13.4. Conclusions

The results presented in this chapter demonstrate a novel approach to assay ECs proliferation using EdU-labelled Raman imaging. This presented method allowed obtaining comprehensive information on EdU incorporation into ECs DNA signalling cell proliferation. It was possible to investigate alterations in ECs' proliferative capacity when they received antiproliferative treatment with (CHX or DOX). The results obtained from the Raman imaging approach to EdU sensing and assaying ECs proliferation were confirmed using the already established method based on fluorescence detection of EdU after its “click chemistry” with a fluorescent azide. Moreover, the Raman imaging-based approach allowed for EdU detection in a click-free manner, permitting live cell imaging of proliferative ECs, showing an advantage over the fluorescence microscopy-based method as it usually requires sample fixation and permeabilization.

Raman and fluorescence imaging of EdU-labelled nuclei was shown to be applied to the *ex vivo* murine aortae model of injured endothelium. In this context, Raman imaging of EdU-labelled aortae samples was done for the first time, however, the sensitivity of this technique is relatively weak and in need of optimization. One approach (presented in more detail in the later chapter) is to utilize new Raman probes offering enhanced signal based on the click chemistry with EdU-tagged DNA.

14. Summary and final conclusions

In this thesis, two novel approaches were presented; one to study ECs lipid-rich cellular organelles (LDs, ER and the nuclear membrane) based on Raman detection of AXT, and the other to study ECs proliferation and regeneration based on EdU Raman sensing. The presented novel demonstrated several enhancements over the previously established approaches to study certain processes in the endothelium in both *in vitro* and *ex vivo* conditions. Furthermore, the results of the labelled Raman imaging approaches presented here were always complemented with other microscopy techniques such as label-free Raman imaging, fluorescence imaging and transient absorption microscopy.

AXT labelled Raman imaging of lipids allowed visualization of lipidic substructures in ECs using a laser power 10 folds lower than the one usually used for label-free Raman microscopy of ECs (3 mW instead of 30 mW). Furthermore, due to the pre-resonance enhancement of the AXT Raman signal when excited with a 532nm laser, clear images with enhanced contrast of the distribution of the lipids in cells could be acquired, thus improving Raman imaging of lipids. Moreover, AXT allowed visualization of the area around the nucleus, attributed to AXT accumulation in the lipidic nuclear envelope. Visualization of the nuclear envelope is not possible using the label-free Raman imaging approach, presenting an advantage in the AXT-labelled approach to Raman imaging of ECs lipids.

Alterations in lipids distribution due to the pro-inflammatory phenotype of ECs were detectable using both label-free and AXT-labelled Raman imaging in a complementary manner. AXT was demonstrated to be a universal Raman probe for subcellular lipidic structure in ECs of various organs as it was tested in ECs from the microvasculature, the aorta, the heart and the brain giving similarly enhanced imaging of cellular lipids in control and inflamed ECs. Transient absorption microscopy results revealed that AXT presented itself in the isolated form rather than forming aggregates in the intracellular lipids.

Raman and fluorescence microscopies were used to assess free and liposomal AXT uptake by ECs, and their respective anti-inflammatory effects. It was shown that both cellular uptake and the anti-inflammatory effects of AXT could be improved by encapsulation in neutral or cationic liposomes and lipoplexes. AXT in its free form exerted its anti-inflammatory effects on ECs by reducing the expression of the surface adhesion molecule ICAM-1 without causing significant changes in ECs lipids content, adding to its list of benefits.

The work done on AXT reviewed its potential as a molecular Raman probe providing resonance or pre-resonance enhancement to detect lipids in ECs in the forms of LDs, ER and the nuclear envelope in ECs of various origins. It showed that AXT uptake and its therapeutic potential against ECs inflammation could be improved through liposomal encapsulation.

EdU was utilized for a novel approach based on Raman imaging to assay ECs proliferation and regeneration in *in vitro* and *ex vivo* conditions. The Raman imaging-based approach does not depend on the “click chemistry” reaction to label EdU with any dye (it could be achieved in a “click-free” manner), permitting live cell EdU detection in ECs. Following the EdU signal in the spectroscopically silent region due to its Raman band at ca. 2122 cm^{-1} , presented a clear visualization of ECs nuclei in different ECs (from the microvasculature, the aorta and the heart) presenting an advantage over label-free Raman imaging of cell nuclei done by following the characteristic DNA band at ca. 788 cm^{-1} which is prone to signal interference.

The newly presented Raman approach to study the proliferation of ECs was sensitive to the antiproliferative treatment of CHX, allowing quantitative analysis of the resulting decrease in EdU signal and in the number of proliferative ECs. These results were confirmed using fluorescence imaging of EdU labelled with Alexa fluor® azide dyes via click chemistry. Moreover, Raman imaging of EdU-labelled DNA in ECs subjected to the cytotoxic effects of DOX allowed the detection of both morphological and antiproliferative effects of DOX presented in an increased nuclear area and a decreased EdU signal, respectively. Studying the antiproliferative effects and the state of newly

synthesized DNA in ECs is not possible using label-free Raman imaging techniques, demonstrating the advantage of the presented approach.

Finally, Raman and fluorescence imaging of EdU-labelled ECs and SMC in isolated murine aorta revealed the applicability of the presented approach to study cell regeneration *ex vivo*. ECs and SMC have been shown to regenerate in *ex vivo* conditions to repair and restore the endothelium layer after induced mechanical injury. Raman imaging of EdU was utilized to detect cell proliferation in isolated aortae samples for the first time.

The presented EdU-labelling approach could benefit from signal enhancement of the characteristic EdU Raman band. One example of such future direction could be the development of azide Raman probes with enhanced Raman spectra for click chemistry applications with EdU, improving its Raman imaging in cells and tissues.

15. Limitations

It is worth noting that the presented techniques have their limitations that should be taken into consideration while utilizing one of them. For instance, it is already known that fluorescence microscopy is burdened with the restriction of the overall number of dyes to be used simultaneously, as usually no more than three dyes could be used in a single cell or tissue sample, limiting the number of cellular organelles or cellular processes to be studied. It is also worth noting that some dyes exert cytotoxic properties and so could not be used to image live cells. Additionally, cell permeability is to be considered in this regard, as some dyes require cell permeabilization too. Furthermore, many dyes hold the risk of photobleaching and require special treatment with the samples such as working in the dark at all times.

Label-free Raman imaging is a powerful technique to study biological samples without the need for introducing dyes. However, it holds some limiting properties as well. For instance, the acquisition of the Raman image requires scanning the sample in a time-consuming fashion (most presented Raman images of a single cell take around 30 min each), which makes it difficult to acquire a big number of measurements. Moreover, Raman bands attributed to specific cellular structures or molecules in complex samples often overlap with one another causing difficulties in interpreting some information.

AXT-labelled Raman imaging approach presents various improvements over the label-free technique, however, it is not possible to differentiate the different types of lipids in the cells relying solely on AXT images, as AXT accumulates in all lipids species in ECs. For instance, Raman imaging of AXT could be used to visualize the nuclear envelope, however, it is not possible to image the nuclear envelope alone using AXT labelling, as AXT would be always also present in LDs and the ER. Due to the resonance effect of AXT, it is challenging to accurately quantify the cell content of lipids or their composition using the Raman spectra dominated with AXT resonance bands. Using AXT-labelled and label-free Raman imaging in a complementary manner to study lipids in ECs is a great workaround to detect cellular lipids content and

composition, however, it is a time-consuming approach requiring every cell to be measured twice; Once with low and once high laser powers.

The Raman-based approach to assay ECs proliferation based on the detection of EdU has proven to be time-consuming, with Raman imaging allowing measurement of multiple cells at once but with lower image contrast or longer acquisition times, and the need to image a substantial number of cells to allow their statistical analysis. There have also been reports of EdU-induced cytotoxic and mutagenic effects, especially when used with high concentrations or long incubation times^{171,172}. Finally, EdU signal while being easily detected in the Raman spectra of cells and allowing enhanced imaging of cell nuclei, EdU detection in isolated aortae samples is challenging and would benefit from enhancement of the EdU signal.

16. Future directions

ECs uptake of AXT was demonstrated here to be improved through encapsulation in liposomes or lipoplexes. This liposomal encapsulation allowed AXT to increase its uptake to ECs and improve its anti-inflammatory effects. AXT-loaded liposomes could be used as an alternative to free AXT when an increased uptake is desired or when lower concentrations of AXT are needed to be used.

16.1. Non-linear Raman imaging techniques

Addressing the time-consuming properties of the Raman imaging techniques presented in this thesis, benefiting from faster Raman imaging-based techniques such as stimulated Raman scattering (SRS) microscopy or coherent anti-stokes Raman scattering (CARS) microscopy could offer the advantages of Raman microscopy without the need to spend longer times for image acquisition. SRS or CARS could be utilized for the presented labelled Raman imaging techniques to study ECs lipids or ECs proliferation based on the detection of AXT or EdU, respectively.

Although being considered a strong tool to investigate biological samples and provide comprehensive information on the biochemical processes, spontaneous Raman scattering is a relatively weak effect. Furthermore, Raman imaging based on collecting the full Raman spectrum from each pixel and integrating the Raman spectra to obtain images of samples such as cells and tissues is considered a time-consuming technique. With the scientific advancements relating to lasers and Raman spectrometers, new techniques involving Raman-active molecular transitions and based on nonlinear effects emerged and were developed substantially¹⁷³.

Unlike spontaneous Raman spectroscopy, SRS spectroscopy is a non-linear and coherent technique that relies on two synchronized pulsed lasers referred to as the pump and the stokes beams¹⁷⁴. SRS probes molecular vibrations similar to spontaneous Raman, however, it offers signal detection that is several orders of magnitude greater than spontaneous Raman scattering¹⁷⁵. Moreover, SRS is

advantageous for its ability to time-resolve vibrational motions. This makes SRS microscopy a great technique for subcellular imaging and for identifying molecules and biochemical interactions of interest with high sensitivity and speed.

While spontaneous Raman scattering techniques rely on the detection of the Stokes Raman scattering, CARS spectroscopy is based on the detection of the anti-Stokes shift. CARS is a third-order nonlinear optical process that offers substantial enhancement of the signal compared to spontaneous Raman scattering¹⁷⁶. It provides spectroscopic information relevant to that of Raman-active resonance while offering several orders of magnitudes higher signal and shorter acquisition times¹⁷⁶. Despite its drawbacks such as having a non-resonant background at the anti-Stokes frequency, CARS remains a great technique for imaging applications, especially imaging of cells and tissues^{173,177}.

16.2. Development of novel Raman probes for click chemistry applications

EdU labelled Raman imaging of ECs regeneration in *en face* aortae samples could benefit from EdU signal enhancement. This could be achieved through the development of azide Raman probes for click chemistry application with EdU following *in vivo* application or *ex vivo* incubation. This approach presents great potential in monitoring vital biological processes such as angiogenesis (the formation of new blood vessels from pre-existing ones) without the need for additional dyes.

“Copper(I)-catalysed azide-alkyne cycloaddition” reaction (CuAAC, “click chemistry”) is used for many applications in various fields due to its high yield, working in different conditions and being unaffected by the groups attached to the alkyne and azide^{178,179}. One of the applications for CuAAC is the fluorescence-based detection of cell proliferation by fluorescently labelling DNA tagged with EdU using an azide dye^{119,120}.

It is possible to detect EdU in complex biological environments such as cells because of the alkyne band that EdU exerts in the spectroscopically “silent region”, where the signal from EdU would not be interfered with by other signals from biological

compounds¹⁰⁸. Although Raman detection of EdU-labelled DNA could be done in a “click-free” fashion i.e. without the need for any additional dyes, the Raman band of alkyne-tagged EdU in cells is relatively weak, resulting in the need for longer incubation times and relatively higher concentration of EdU (at least 3 hours of incubation with 20 μM EdU was needed¹⁵⁵), compared to fluorescence subsequent imaging (ca. 1h of incubation of 10 μM EdU). Therefore, a Raman probe that gives an enhanced Raman signal, especially for *ex vivo* Raman imaging, could be of great value.

Here, two concepts of Raman probes for click chemistry applications are presented; One with the potential of improving Raman-based detection of EdU through resonance enhancement, and the other offers signal enhancement in the spectroscopic silent region.

16.2.1. Resonance Raman enhancement

As is the case with AXT (presented in the previous chapters), resonantly enhanced Raman bands could be achieved, resulting in an intense Raman signal easily observable in the Raman spectra of complex samples such as cells. EdU incorporates into cellular DNA during replication, and a click chemistry reaction could be used to label intracellular EdU allowing enhanced imaging of cellular DNA, particularly of newly synthesised DNA and cell proliferation. Utilizing click chemistry to improve Raman detection of cellular DNA; by following the intense characteristic bands of a resonance Raman probe labelling EdU-tagged DNA is the concept behind this proposed approach (Figure 13.9).



Figure 16.1. “Click chemistry” for Raman detection. The concept of Raman microscopy detection of EdU as EdU incorporates into DNA, then a CuAAC reaction “click chemistry” is used to enhance the EdU signal.

Retinol presents a resonantly enhanced Raman spectrum when excited with a 532 nm laser, with the most intense Raman band presented at ca. 1593 cm^{-1} (Figure 13.10). For its potential to enhance Raman imaging of EdU via click chemistry, the retinol structure was modified to accommodate a terminal azide. The resulting compound of the click chemistry reaction between EdU and modified retinol showed a clear resonance enhancement detected with Raman spectroscopy when the sample was excited using a laser with an excitation wavelength of 532 nm.

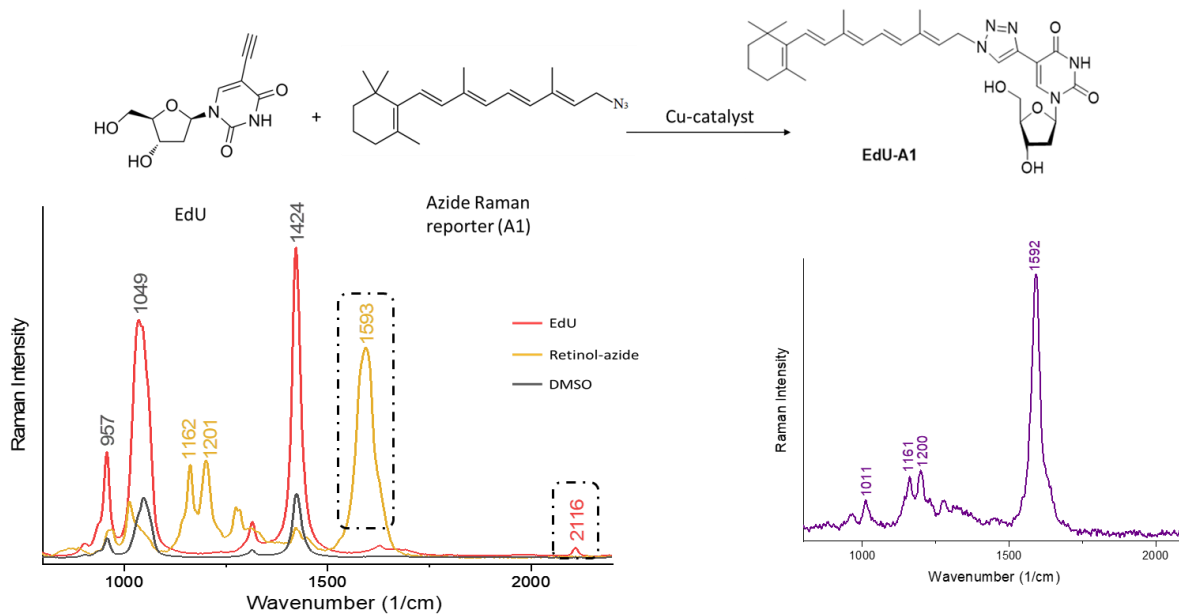


Figure 16.2. The “click chemistry” reaction between EdU and the azide Raman reporter, with the spectra of the azide reporter (yellow), and EdU (red) on the right side compared

the relative intensity of their respective characteristic bands. On the left side, the Raman spectrum of the end product (EdU-A1)

16.2.2. Enhancement of the Raman band in the silent region

Similarly to a previously reported method, a potential azide Raman probe with two (C≡C) bonds was synthesized for the purpose of enhancing the Raman imaging of EdU-labelled cell DNA. The multistep organic synthesis scheme shown in (Figure 13.11A) demonstrates in steps how the potential Raman probe was produced.

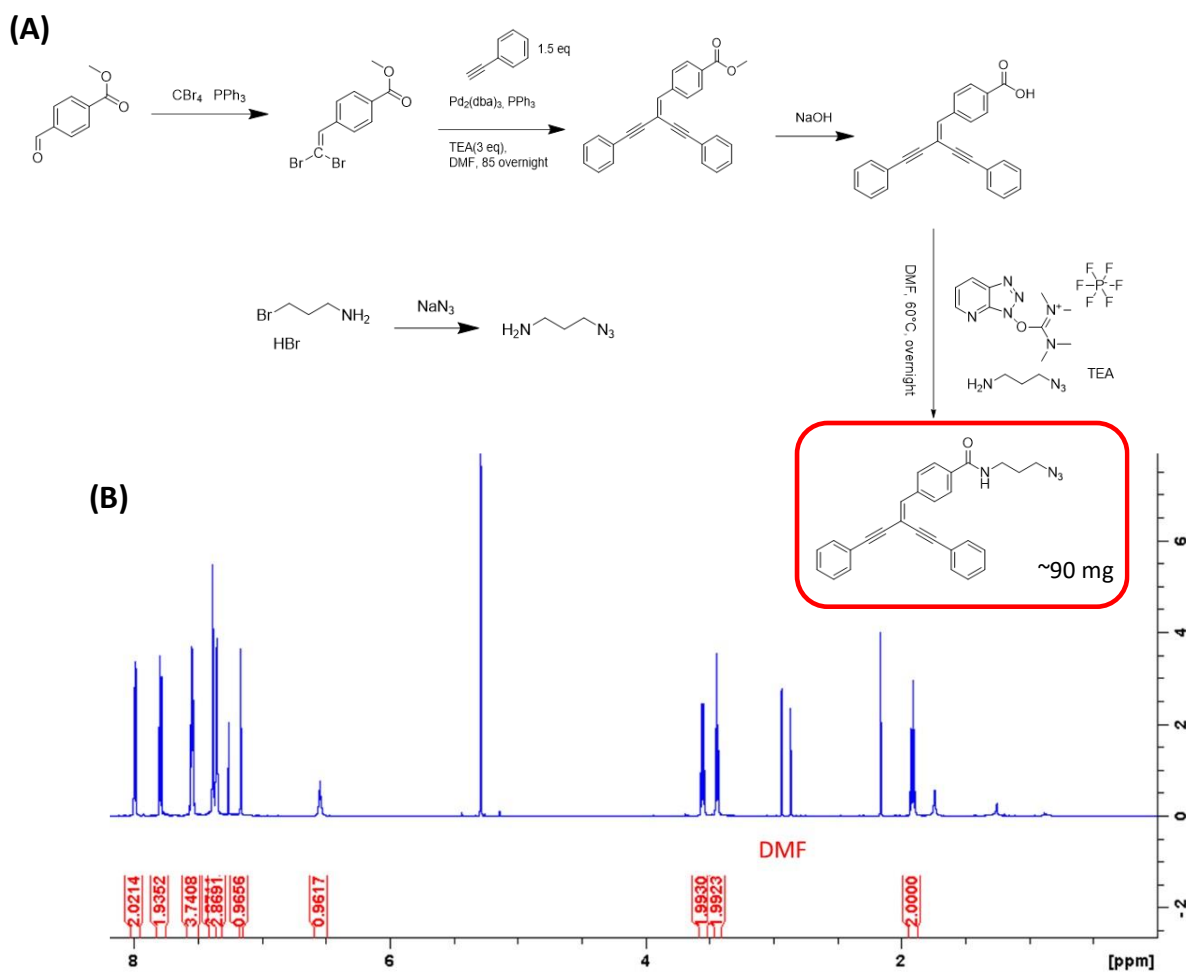


Figure 16.3. Synthesis of a potential azide Raman probe. (A) The synthesis scheme of the azide Raman probe. **(B)** NMR spectrum of the final product.

The resulting compound demonstrated significantly enhanced alkyne Raman bands compared to EdU, evidenced by the Raman spectra collected for both molecules in solid state and when dissolved in DMSO. The resulting molecule showed two overlapping alkyne Raman bands with peaks at ca. 2193 and 2209 cm^{-1} as opposed to EdU which demonstrates an alkyne Raman band at ca. 2122 cm^{-1} (Figure 13.12).

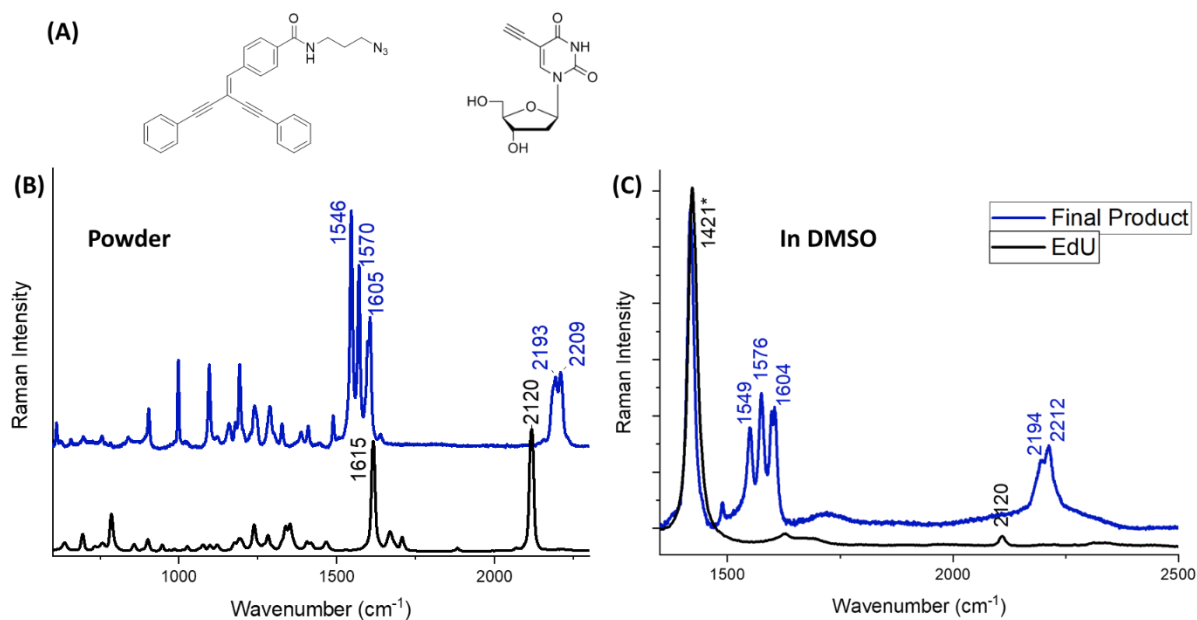


Figure 16.4. Enhancement of the Raman signal using a potential click chemistry Raman probe. (A) Structure of the synthesis final product and EdU. Raman spectra of the product (blue) and EdU (black) in solid state (B) and dissolved in DMSO (10 mM, C).

These potential Raman probes (presented in chapter 13.5) are aimed at enhancing the Raman signal of EdU following their click reaction with EdU-labelled DNA, especially in cells and tissues. To assess their applicability for such applications, their permeability through the cell membrane and the outcome of the click chemistry reaction performed *in cellulo* should be studied by the means of Raman microscopy.

16.3. Multiplex Raman imaging

Finally, a proof of concept study presented multiplex Raman imaging of ECs organelles, specifically nucleus, mitochondria and ER through labelling the same sample with EdU, MitoBADY and falcarinol, respectively (representative image shown in Figure 16.1). Multiplex labelled Raman imaging of subcellular structures could be utilized to investigate alterations in multiple cell organelles or changes in multiple cellular processes associated with disease development.

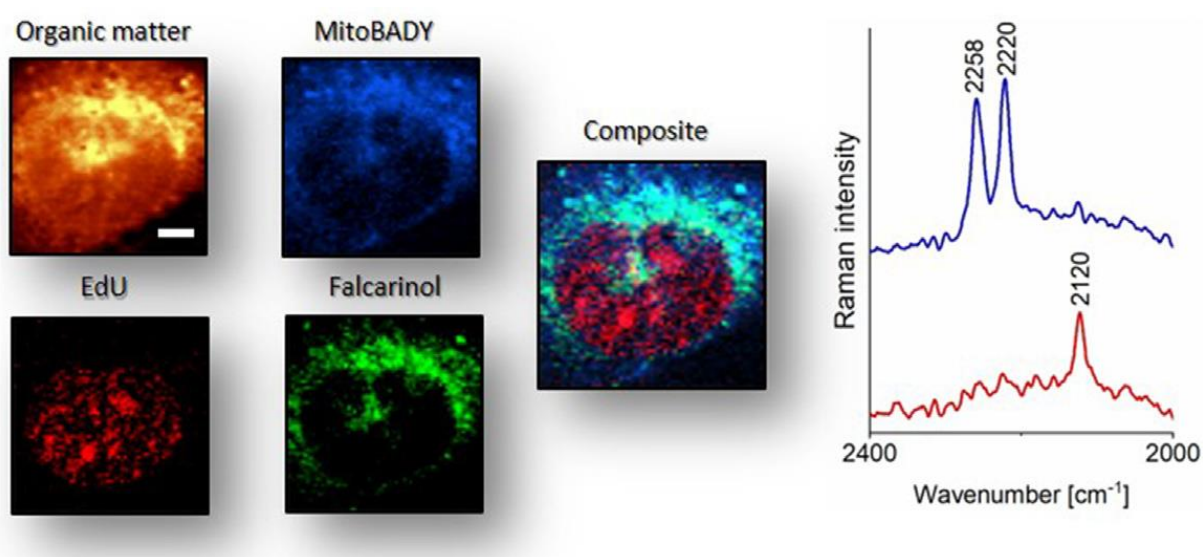


Figure 16.5. Multiplex labelled Raman imaging of cell organelles. HMEC-1 labelled with EdU, MitoBADY and falcarinol to image the nucleus, mitochondria and ER, respectively, showing their composite image and the distribution of all organic matter for reference. On the right side cropped Raman spectra of the nucleus (red) showing EdU alkyne band, and of the cytoplasm (blue) showing the alkyne bands of MitoBADY and falcarinol. The figure was adopted from Ref. [155].

List of Publications

Related to the PhD thesis:

- (1) “**Radwan, B.**; Prabhakaran, A.; Rocchetti, S.; Matuszyk, E.; Keyes, T. E.; Baranska, M. Uptake and anti-inflammatory effect of liposomal astaxanthin on endothelial cells studied by Raman imaging” (Submitted to Chemical Communications, Elsevier) **IF=6.065, MNiSW=200**
- (2) “**Radwan, B.**; Rocchetti, S.; Matuszyk, E.; Sternak, M.; Stodulski, M.; Pawlowski, R.; Mlynarski, J.; Brzozowski, K.; Chlopicki, S.; Baranska, M. EdU Sensing: The Raman Way of Following Endothelial Cell Proliferation in Vitro and Ex Vivo. *Biosens. Bioelectron.* **2022**, *216* (August), 114624. <https://doi.org/10.1016/j.bios.2022.114624>.” **IF=12.545, MNiSW=200**
- (3) “**Radwan, B.**; Adamczyk, A.; Tott, S.; Czamara, K.; Kaminska, K.; Matuszyk, E.; Baranska, M. Labeled vs. Label-Free Raman Imaging of Lipids in Endothelial Cells of Various Origins. *Molecules* **2020**, *25* (23), 5752. <https://doi.org/10.3390/molecules25235752>.” **IF=4.927, MNiSW=140**
- (4) “Czamara, K.; Adamczyk, A.; Stojak, M.; **Radwan, B.**; Baranska, M. Astaxanthin as a New Raman Probe for Biosensing of Specific Subcellular Lipidic Structures: Can We Detect Lipids in Cells under Resonance Conditions? *Cell. Mol. Life Sci.* **2021**, *78* (7), 3477–3484. <https://doi.org/10.1007/s00018-020-03718-1>.” **IF=10.001, MNiSW=140**
- (5) “Yang, T.; Chettri, A.; **Radwan, B.**; Matuszyk, E.; Baranska, M.; Dietzek, B. Monitoring Excited-State Relaxation in a Molecular Marker in Live Cells—a Case Study on Astaxanthin. *Chem. Commun.* **2021**, *57* (52), 6392–6395. <https://doi.org/10.1039/D1CC01907D>.” **IF=6.065, MNiSW=200**
- (6) “Adamczyk, A.; Matuszyk, E.; **Radwan, B.**; Rocchetti, S.; Chlopicki, S.; Baranska, M. Toward Raman Subcellular Imaging of Endothelial Dysfunction. *J. Med. Chem.* **2021**, *64* (8), 4396–4409. <https://doi.org/10.1021/acs.jmedchem.1c00051>.” **IF=8.039, MNiSW=200**
- (7) “Matuszyk, E.; Adamczyk, A.; **Radwan, B.**; Pieczara, A.; Szcześniak, P.; Mlynarski, J.; Kamińska, K.; Baranska, M. Multiplex Raman Imaging of Organelles in Endothelial Cells. *Spectrochim. Acta Part A Mol. Biomol. Spectrosc.* **2021**, *255*, 119658. <https://doi.org/10.1016/j.saa.2021.119658>.” **IF=4.831, MNiSW=140**

Not related to the PhD thesis:

- (1) “Radwan, B.; Bosgelmez, I. The Safety of Chelators for Iron Overload in Sickle Cell Disease: A Brief Systematic Review. **2019**, *50* (3), 50–60. <https://doi.org/10.32552/2019.ActaMedica.368>”
- (2) “**Radwan, B.** The Safety of Chelators Used For Transfusion-Induced Iron Overload in Sickle Cell Disease, Erciyes University, Masters of Pharmacy Thesis, **2019**.”
- (3) “Öztürk, E.; Karaboğa, K. A. A.; **Radwan, B.**; Yerer, M. B. Curcumin Enhances the Efficacy of 5-FU in Colo205 Cell Lines. **2017**, 8–11. <https://doi.org/10.3390/proceedings1100995>.”

Conference proceedings:

- (1) “**Radwan, B.**; Matuszyk, E.; Rocchetti, S.; Prabhakaran, A.; Sternak, M.; Chlopicki, S.; Keyes, T. E.; Baranska, M. Multimodal Imaging of Endothelial Pathology Models in Vitro and Ex Vivo. In *the 7th International Conference on Molecular Sensors and Molecular Logic Gates (MSMLG 2022)*; Dublin, Ireland, **2022**.” (Oral and poster presentations)
- (2) “**Radwan, B.**; Rocchetti, S.; Matuszyk, E.; Chlopicki, S.; Baranska, M. EdU-Labeling: Raman-Based Click-Free Detection of Endothelial Cell Proliferation. In *11th International Conference on Advanced Vibrational Spectroscopy (ICAVS 11)*; Krakow, Poland, **2011**.” (Poster flash presentation)
- (3) “**Radwan, B.**; Rocchetti, S.; Matuszyk, E.; Sternak, M.; Chlopicki, S.; Baranska, M. EdU-Labeling: Raman-Based Click-Free Detection of Endothelial Cell Proliferation. In *1st symposium on Molecular Biosensing: From Theory to Practice*; Online, **2021**; p 11.” (Oral presentation)

List of secondments and internships

- (1) Secondment at **Dublin City University (DCU)** – Visiting Researcher (June 2022 – July 2022).
 - Performed multistep organic synthesis of potential Raman probes, and the characterization of the synthetic products using NMR and MS.
 - Trained in liposomes preparation through lipid extrusion and electroformation, and characterization using DLS and confocal fluorescence microscopy.
 - Collaborated on a study to assess the liposomal encapsulation of AXT on AXT uptake into ECs and its anti-inflammatory effects.

- (2) Internship at the **Institute of Nuclear Physics Polish Academy of Sciences (PAS)** – Research Intern (October 2021).
 - Trained in surface-enhanced Raman scattering (SERS) microscopy, atomic force microscopy, Nano-IR, Fourier transform IR spectroscopy and RT-PCR techniques.

- (3) Internship at the **Institute of Physical Chemistry PAS** – Research Intern (October 2021).
 - Trained in SERS microscopy and the production of silver and gold substrates for SERS.
 - Trained on bacteriological culture.
 - Was introduced to chemometrics and multivariate analysis using Unscrambler software.

References

- (1) Rajendran, P.; Rengarajan, T.; Thangavel, J.; Nishigaki, Y.; Sakthisekaran, D.; Sethi, G.; Nishigaki, I. The Vascular Endothelium and Human Diseases. *Int. J. Biol. Sci.* **2013**, *9* (10), 1057–1069. <https://doi.org/10.7150/ijbs.7502>.
- (2) Tucker, W. D.; Arora, Y.; Mahajan, K. Anatomy, Blood Vessels. In *StatPearls [Internet]*; Treasure Island (FL), 2022.
- (3) Alberts, B.; Johnson, A.; Lewis, J.; Morgan, D.; Raff, M.; Roberts, K.; Walter, P. *Molecular Biology of the Cell*; Wilson, J., Hunt, T., Eds.; W.W. Norton & Company, 2017. <https://doi.org/10.1201/9781315735368>.
- (4) Shaw, C. J.; ter Haar, G. R.; Rivens, I. H.; Giussani, D. A.; Lees, C. C. Pathophysiological Mechanisms of High-Intensity Focused Ultrasound-Mediated Vascular Occlusion and Relevance to Non-Invasive Fetal Surgery. *J. R. Soc. Interface* **2014**, *11* (95), 20140029. <https://doi.org/10.1098/rsif.2014.0029>.
- (5) Michiels, C. Endothelial Cell Functions. *J. Cell. Physiol.* **2003**, *196* (3), 430–443. <https://doi.org/10.1002/jcp.10333>.
- (6) Yazdani, S.; Jaldin-Fincati, J. R.; Pereira, R. V. S.; Klip, A. Endothelial Cell Barriers: Transport of Molecules between Blood and Tissues. *Traffic* **2019**, *20* (6), 390–403. <https://doi.org/10.1111/tra.12645>.
- (7) Galley, H. F.; Webster, N. R. Physiology of the Endothelium. *Br. J. Anaesth.* **2004**, *93* (1), 105–113. <https://doi.org/10.1093/bja/aeh163>.
- (8) Cerutti, C.; Ridley, A. J. Endothelial Cell-Cell Adhesion and Signaling. *Exp. Cell Res.* **2017**, *358* (1), 31–38. <https://doi.org/https://doi.org/10.1016/j.yexcr.2017.06.003>.
- (9) Dejana, E.; Vestweber, D. The Role of VE-Cadherin in Vascular Morphogenesis and Permeability Control; 2013; pp 119–144. <https://doi.org/10.1016/B978-0-12-394311-8.00006-6>.

- (10) Adamczyk, A.; Matuszyk, E.; Radwan, B.; Rocchetti, S.; Chlopicki, S.; Baranska, M. Toward Raman Subcellular Imaging of Endothelial Dysfunction. *J. Med. Chem.* **2021**, *64* (8), 4396–4409. <https://doi.org/10.1021/acs.jmedchem.1c00051>.
- (11) Campbell, W. B.; Fleming, I. Epoxyeicosatrienoic Acids and Endothelium-Dependent Responses. *Pflügers Arch. - Eur. J. Physiol.* **2010**, *459* (6), 881–895. <https://doi.org/10.1007/s00424-010-0804-6>.
- (12) Battson, M. L.; Lee, D. M.; Gentile, C. L. Endoplasmic Reticulum Stress and the Development of Endothelial Dysfunction. *Am. J. Physiol. Circ. Physiol.* **2017**, *312* (3), H355–H367. <https://doi.org/10.1152/ajpheart.00437.2016>.
- (13) Félétou, M.; Köhler, R.; Vanhoutte, P. M. Nitric Oxide: Orchestrator of Endothelium-Dependent Responses. *Ann. Med.* **2012**, *44* (7), 694–716. <https://doi.org/10.3109/07853890.2011.585658>.
- (14) Félétou, M.; Vanhoutte, P. M. Endothelial Dysfunction: A Multifaceted Disorder (The Wiggers Award Lecture). *Am. J. Physiol. Circ. Physiol.* **2006**, *291* (3), H985–H1002. <https://doi.org/10.1152/ajpheart.00292.2006>.
- (15) Pernow, J.; Shemyakin, A.; Böhm, F. New Perspectives on Endothelin-1 in Atherosclerosis and Diabetes Mellitus. *Life Sci.* **2012**, *91* (13–14), 507–516. <https://doi.org/10.1016/j.lfs.2012.03.029>.
- (16) Benigni, A.; Cassis, P.; Remuzzi, G. Angiotensin II Revisited: New Roles in Inflammation, Immunology and Aging. *EMBO Mol. Med.* **2010**, *2* (7), 247–257. <https://doi.org/10.1002/emmm.201000080>.
- (17) Staton, C. A.; Reed, M. W. R.; Brown, N. J. A Critical Analysis of Current in Vitro and in Vivo Angiogenesis Assays. *Int. J. Exp. Pathol.* **2009**, *90* (3), 195–221. <https://doi.org/10.1111/j.1365-2613.2008.00633.x>.
- (18) Carmeliet, P. Angiogenesis in Life, Disease and Medicine. *Nature* **2005**, *438* (7070), 932–936. <https://doi.org/10.1038/nature04478>.
- (19) Deanfield, J. E.; Halcox, J. P.; Rabelink, T. J. Endothelial Function and Dysfunction. *Circulation* **2007**, *115* (10), 1285–1295.

<https://doi.org/10.1161/CIRCULATIONAHA.106.652859>.

- (20) Yau, J. W.; Teoh, H.; Verma, S. Endothelial Cell Control of Thrombosis. *BMC Cardiovasc. Disord.* **2015**, *15* (1), 130. <https://doi.org/10.1186/s12872-015-0124-z>.
- (21) Mohan Rao, L. V.; Esmon, C. T.; Pendurthi, U. R. Endothelial Cell Protein C Receptor: A Multiliganded and Multifunctional Receptor. *Blood* **2014**, *124* (10), 1553–1562. <https://doi.org/10.1182/blood-2014-05-578328>.
- (22) Boffa, M.-C.; Karmochkine, M. Thrombomodulin: An Overview and Potential Implications in Vascular Disorders. *Lupus* **1998**, *7* (2_suppl), 120–125. <https://doi.org/10.1177/096120339800700227>.
- (23) Kadl, A.; Leitinger, N. The Role of Endothelial Cells in the Resolution of Acute Inflammation. *Antioxid. Redox Signal.* **2005**, *7* (11–12), 1744–1754. <https://doi.org/10.1089/ars.2005.7.1744>.
- (24) Pober, J. S.; Sessa, W. C. Evolving Functions of Endothelial Cells in Inflammation. *Nature Reviews Immunology*. October 2007, pp 803–815. <https://doi.org/10.1038/nri2171>.
- (25) Liao, J. K. Linking Endothelial Dysfunction with Endothelial Cell Activation. *J. Clin. Invest.* **2013**, *123* (2), 540–541. <https://doi.org/10.1172/JCI66843>.
- (26) Maslak, E.; Gregorius, A.; Chlopicki, S. Liver Sinusoidal Endothelial Cells (LSECs) Function and NAFLD; NO-Based Therapy Targeted to the Liver. *Pharmacol. Reports* **2015**, *67* (4), 689–694. <https://doi.org/10.1016/j.pharep.2015.04.010>.
- (27) Smeda, M.; Przyborowski, K.; Stojak, M.; Chlopicki, S. The Endothelial Barrier and Cancer Metastasis: Does the Protective Facet of Platelet Function Matter? *Biochem. Pharmacol.* **2020**, *176*, 113886. <https://doi.org/10.1016/j.bcp.2020.113886>.
- (28) Smeda, M.; Chlopicki, S. Endothelial Barrier Integrity in COVID-19-Dependent Hyperinflammation: Does the Protective Facet of Platelet Function Matter? *Cardiovasc. Res.* **2020**, *116* (10), e118–e121. <https://doi.org/10.1093/cvr/cvaa190>.

- (29) Huertas, A.; Montani, D.; Savale, L.; Pichon, J.; Tu, L.; Parent, F.; Guignabert, C.; Humbert, M. Endothelial Cell Dysfunction: A Major Player in SARS-CoV-2 Infection (COVID-19)? *Eur. Respir. J.* **2020**, *56* (1), 2001634.
<https://doi.org/10.1183/13993003.01634-2020>.
- (30) Ruhl, L.; Pink, I.; Kühne, J. F.; Beushausen, K.; Keil, J.; Christoph, S.; Sauer, A.; Boblitz, L.; Schmidt, J.; David, S.; Jäck, H.-M.; Roth, E.; Cornberg, M.; Schulz, T. F.; Welte, T.; Höper, M. M.; Falk, C. S. Endothelial Dysfunction Contributes to Severe COVID-19 in Combination with Dysregulated Lymphocyte Responses and Cytokine Networks. *Signal Transduct. Target. Ther.* **2021**, *6* (1), 418.
<https://doi.org/10.1038/s41392-021-00819-6>.
- (31) World Health Organization. Cardiovascular diseases [https://www.who.int/en/news-room/fact-sheets/detail/cardiovascular-diseases-\(cvds\)](https://www.who.int/en/news-room/fact-sheets/detail/cardiovascular-diseases-(cvds)) (accessed Jan 27, 2023).
- (32) Touyz, R. M.; Chen, X.; Tabet, F.; Yao, G.; He, G.; Quinn, M. T.; Pagano, P. J.; Schiffrin, E. L. Expression of a Functionally Active Gp91phox-Containing Neutrophil-Type NAD(P)H Oxidase in Smooth Muscle Cells From Human Resistance Arteries. *Circ. Res.* **2002**, *90* (11), 1205–1213.
<https://doi.org/10.1161/01.RES.0000020404.01971.2F>.
- (33) Schiffrin, E. L.; Park, J. B.; Pu, Q. Effect of Crossing over Hypertensive Patients from a Beta-Blocker to an Angiotensin Receptor Antagonist on Resistance Artery Structure and on Endothelial Function. *J. Hypertens.* **2002**, *20* (1), 71–78.
<https://doi.org/10.1097/00004872-200201000-00011>.
- (34) Daiber, A.; Chlopicki, S. Revisiting Pharmacology of Oxidative Stress and Endothelial Dysfunction in Cardiovascular Disease: Evidence for Redox-Based Therapies. *Free Radic. Biol. Med.* **2020**, *157*, 15–37.
<https://doi.org/10.1016/j.freeradbiomed.2020.02.026>.
- (35) Chlopicki, S. Perspectives in Pharmacology of Endothelium: From Bench to Bedside. *Pharmacol. Reports* **2015**, *67* (4), vi–ix.
<https://doi.org/10.1016/j.pharep.2015.08.005>.
- (36) Czamara, K.; Petko, F.; Baranska, M.; Kaczor, A. Raman Microscopy at the

- Subcellular Level: A Study on Early Apoptosis in Endothelial Cells Induced by Fas Ligand and Cycloheximide. *Analyst* **2016**, *141* (4), 1390–1397.
<https://doi.org/10.1039/C5AN02202A>.
- (37) Smith, R.; Wright, K. L.; Ashton, L. Raman Spectroscopy: An Evolving Technique for Live Cell Studies. *Analyst* **2016**, *141* (12), 3590–3600.
<https://doi.org/10.1039/C6AN00152A>.
- (38) Duer, M.; Cobb, A. M.; Shanahan, C. M. DNA Damage Response. *Arterioscler. Thromb. Vasc. Biol.* **2020**, *40* (7), E193–E202.
<https://doi.org/10.1161/ATVBAHA.120.313792>.
- (39) Groschner, L. N.; Waldeck-Weiermair, M.; Malli, R.; Graier, W. F. Endothelial Mitochondria—Less Respiration, More Integration. *Pflügers Arch. - Eur. J. Physiol.* **2012**, *464* (1), 63–76. <https://doi.org/10.1007/s00424-012-1085-z>.
- (40) Kluge, M. A.; Fetterman, J. L.; Vita, J. A. Mitochondria and Endothelial Function. *Circ. Res.* **2013**, *112* (8), 1171–1188.
<https://doi.org/10.1161/CIRCRESAHA.111.300233>.
- (41) Elizabeth, M.; Hossein, A.; S., B. R.; Fabio, D.; W., D. G.; N., K. R.; Kinya, O.; Peipei, P.; Rosario, R.; N., S. M.; Douglas, W.; J., Y. R. Mitochondrial Function, Biology, and Role in Disease. *Circ. Res.* **2016**, *118* (12), 1960–1991.
<https://doi.org/10.1161/RES.000000000000104>.
- (42) Du, X. L.; Edelstein, D.; Dimmeler, S.; Ju, Q.; Sui, C.; Brownlee, M. Hyperglycemia Inhibits Endothelial Nitric Oxide Synthase Activity by Posttranslational Modification at the Akt Site. *J. Clin. Invest.* **2001**, *108* (9), 1341–1348. <https://doi.org/10.1172/JCI11235>.
- (43) Du, X.; Matsumura, T.; Edelstein, D.; Rossetti, L.; Zsengellér, Z.; Szabó, C.; Brownlee, M. Inhibition of GAPDH Activity by Poly(ADP-Ribose) Polymerase Activates Three Major Pathways of Hyperglycemic Damage in Endothelial Cells. *J. Clin. Invest.* **2003**, *112* (7), 1049–1057. <https://doi.org/10.1172/JCI18127>.
- (44) Hammes, H.-P.; Du, X.; Edelstein, D.; Taguchi, T.; Matsumura, T.; Ju, Q.; Lin, J.;

- Bierhaus, A.; Nawroth, P.; Hannak, D.; Neumaier, M.; Bergfeld, R.; Giardino, I.; Brownlee, M. Benfotiamine Blocks Three Major Pathways of Hyperglycemic Damage and Prevents Experimental Diabetic Retinopathy. *Nat. Med.* **2003**, *9*, 294–299. <https://doi.org/10.1038/nm834>.
- (45) K., D. A.; G., H. D.; I., D. S. Molecular Mechanisms of Angiotensin II–Mediated Mitochondrial Dysfunction. *Circ. Res.* **2008**, *102* (4), 488–496. <https://doi.org/10.1161/CIRCRESAHA.107.162800>.
- (46) Bunney, P. E.; Zink, A. N.; Holm, A. A.; Billington, C. J.; Kotz, C. M. Orexin Activation Counteracts Decreases in Nonexercise Activity Thermogenesis (NEAT) Caused by High-Fat Diet. *Physiol. Behav.* **2017**, *176*, 139–148. <https://doi.org/10.1016/j.physbeh.2017.03.040>.
- (47) Maamoun, H.; Abdelsalam, S.; Zeidan, A.; Korashy, H.; Agouni, A. Endoplasmic Reticulum Stress: A Critical Molecular Driver of Endothelial Dysfunction and Cardiovascular Disturbances Associated with Diabetes. *Int. J. Mol. Sci.* **2019**, *20* (7), 1658. <https://doi.org/10.3390/ijms20071658>.
- (48) Maamoun, H.; Abdelsalam, S. S.; Zeidan, A.; Korashy, H. M.; Agouni, A. Endoplasmic Reticulum Stress: A Critical Molecular Driver of Endothelial Dysfunction and Cardiovascular Disturbances Associated with Diabetes. *International journal of molecular sciences*. Department of Medical Biochemistry and Molecular Biology, Faculty of Medicine, Ain Shams University, Abbaseyya, Cairo 11566, Egypt. hatem_maamoun@med.asu.edu.eg. 2019. <https://doi.org/10.3390/ijms20071658>.
- (49) Luchetti, F.; Crinelli, R.; Cesarini, E.; Canonico, B.; Guidi, L.; Zerbinati, C.; Di Sario, G.; Zamaï, L.; Magnani, M.; Papa, S.; Iuliano, L. Endothelial Cells, Endoplasmic Reticulum Stress and Oxysterols. *Redox Biol.* **2017**, *13*, 581–587. <https://doi.org/https://doi.org/10.1016/j.redox.2017.07.014>.
- (50) Fiorentino, T. V.; Procopio, T.; Mancuso, E.; Arcidiacono, G. P.; Andreozzi, F.; Arturi, F.; Sciacqua, A.; Perticone, F.; Hribal, M. L.; Sesti, G. SRT1720 Counteracts Glucosamine-Induced Endoplasmic Reticulum Stress and Endothelial

- Dysfunction. *Cardiovasc. Res.* **2015**, *107* (2), 295–306.
<https://doi.org/10.1093/cvr/cvv169>.
- (51) Jarc, E.; Petan, T. A Twist of FATE: Lipid Droplets and Inflammatory Lipid Mediators. *Biochimie* **2020**, *169*, 69–87.
<https://doi.org/10.1016/j.biochi.2019.11.016>.
- (52) Czamara, K.; Majzner, K.; Pacia, M. Z.; Kochan, K.; Kaczor, A.; Baranska, M. Raman Spectroscopy of Lipids: A Review. *J. Raman Spectrosc.* **2015**, *46* (1), 4–20. <https://doi.org/10.1002/jrs.4607>.
- (53) Ference, B. A.; Graham, I.; Tokgozoglu, L.; Catapano, A. L. Impact of Lipids on Cardiovascular Health. *J. Am. Coll. Cardiol.* **2018**, *72* (10), 1141–1156.
<https://doi.org/10.1016/j.jacc.2018.06.046>.
- (54) Baranska, M.; Kaczor, A.; Malek, K.; Jaworska, A.; Majzner, K.; Staniszewska-Slezak, E.; Pacia, M. Z.; Zajac, G.; Dybas, J.; Wiercigroch, E. Raman Microscopy as a Novel Tool to Detect Endothelial Dysfunction. *Pharmacol. Reports* **2015**, *67* (4), 736–743. <https://doi.org/10.1016/j.pharep.2015.03.015>.
- (55) Jung, H. S.; Shimizu-Albergine, M.; Shen, X.; Kramer, F.; Shao, D.; Vivekanandan-Giri, A.; Pennathur, S.; Tian, R.; Kanter, J. E.; Bornfeldt, K. E. TNF- α Induces Acyl-CoA Synthetase 3 to Promote Lipid Droplet Formation in Human Endothelial Cells. *J. Lipid Res.* **2020**, *61* (1), 33–44.
<https://doi.org/10.1194/jlr.RA119000256>.
- (56) Czamara, K.; Majzner, K.; Selmi, A.; Baranska, M.; Ozaki, Y.; Kaczor, A. Unsaturated Lipid Bodies as a Hallmark of Inflammation Studied by Raman 2D and 3D Microscopy. *Sci. Rep.* **2017**, *7* (1), 40889.
<https://doi.org/10.1038/srep40889>.
- (57) Radwan, B.; Adamczyk, A.; Tott, S.; Czamara, K.; Kaminska, K.; Matuszyk, E.; Baranska, M. Labeled vs. Label-Free Raman Imaging of Lipids in Endothelial Cells of Various Origins. *Molecules* **2020**, *25* (23), 5752.
<https://doi.org/10.3390/molecules25235752>.

- (58) Jiang, F. Autophagy in Vascular Endothelial Cells. *Clin. Exp. Pharmacol. Physiol.* **2016**, *43* (11), 1021–1028. <https://doi.org/10.1111/1440-1681.12649>.
- (59) Schaaf, M. B.; Houbaert, D.; Meçe, O.; Agostinis, P. Autophagy in Endothelial Cells and Tumor Angiogenesis. *Cell Death Differ.* **2019**, *26* (4), 665–679. <https://doi.org/10.1038/s41418-019-0287-8>.
- (60) Nussenzweig, S. C.; Verma, S.; Finkel, T. The Role of Autophagy in Vascular Biology. *Circ. Res.* **2015**, *116* (3), 480–488. <https://doi.org/10.1161/CIRCRESAHA.116.303805>.
- (61) Bao, J.-X.; Xia, M.; Poklis, J. L.; Han, W.-Q.; Brimson, C.; Li, P.-L. Triggering Role of Acid Sphingomyelinase in Endothelial Lysosome-Membrane Fusion and Dysfunction in Coronary Arteries. *Am. J. Physiol. Circ. Physiol.* **2010**, *298* (3), H992–H1002. <https://doi.org/10.1152/ajpheart.00958.2009>.
- (62) Bao, J.-X.; Chang, H.; Lv, Y.-G.; Yu, J.-W.; Bai, Y.-G.; Liu, H.; Cai, Y.; Wang, L.; Ma, J.; Chang, Y.-M. Lysosome-Membrane Fusion Mediated Superoxide Production in Hyperglycaemia-Induced Endothelial Dysfunction. *PLoS One* **2012**, *7* (1), e30387. <https://doi.org/10.1371/journal.pone.0030387>.
- (63) Li, W.; Ghosh, M.; Eftekhari, S.; Yuan, X.-M. Lipid Accumulation and Lysosomal Pathways Contribute to Dysfunction and Apoptosis of Human Endothelial Cells Caused by 7-Oxysterols. *Biochem. Biophys. Res. Commun.* **2011**, *409* (4), 711–716. <https://doi.org/10.1016/j.bbrc.2011.05.071>.
- (64) Lei, Z.; Hu, X.; Wu, Y.; Fu, L.; Lai, S.; Lin, J.; Li, X.; Lv, Y. The Role and Mechanism of the Vascular Endothelial Niche in Diseases: A Review. *Front. Physiol.* **2022**, *13* (April), 1–11. <https://doi.org/10.3389/fphys.2022.863265>.
- (65) Storch, A. S.; Mattos, J. D. de; Alves, R.; Galdino, I. dos S.; Rocha, H. N. M. Methods of Endothelial Function Assessment: Description and Applications. *Int. J. Cardiovasc. Sci.* **2017**, *30* (3), 262–273. <https://doi.org/10.5935/2359-4802.20170034>.
- (66) Zhang, J. Biomarkers of Endothelial Activation and Dysfunction in Cardiovascular

- Diseases. *Rev. Cardiovasc. Med.* **2022**, *23* (2), 073.
<https://doi.org/10.31083/j.rcm2302073>.
- (67) Szmitko, P. E.; Wang, C.-H.; Weisel, R. D.; de Almeida, J. R.; Anderson, T. J.; Verma, S. New Markers of Inflammation and Endothelial Cell Activation. *Circulation* **2003**, *108* (16), 1917–1923.
<https://doi.org/10.1161/01.CIR.0000089190.95415.9F>.
- (68) Huo, Y.; Ley, K. Adhesion Molecules and Atherogenesis. *Acta Physiol. Scand.* **2001**, *173* (1), 35–43. <https://doi.org/10.1046/j.1365-201X.2001.00882.x>.
- (69) Hwang, S.-J.; Ballantyne, C. M.; Sharrett, A. R.; Smith, L. C.; Davis, C. E.; Gotto, A. M.; Boerwinkle, E. Circulating Adhesion Molecules VCAM-1, ICAM-1, and E-Selectin in Carotid Atherosclerosis and Incident Coronary Heart Disease Cases. *Circulation* **1997**, *96* (12), 4219–4225. <https://doi.org/10.1161/01.CIR.96.12.4219>.
- (70) Tzoulaki, I.; Murray, G. D.; Lee, A. J.; Rumley, A.; Lowe, G. D. O.; Fowkes, F. G. R. C-Reactive Protein, Interleukin-6, and Soluble Adhesion Molecules as Predictors of Progressive Peripheral Atherosclerosis in the General Population. *Circulation* **2005**, *112* (7), 976–983.
<https://doi.org/10.1161/CIRCULATIONAHA.104.513085>.
- (71) Gimbrone, M. A.; García-Cardena, G. Endothelial Cell Dysfunction and the Pathobiology of Atherosclerosis. *Circ. Res.* **2016**, *118* (4), 620–636.
<https://doi.org/10.1161/CIRCRESAHA.115.306301>.
- (72) Puddu, P.; Puddu, G. M.; Cravero, E.; Muscari, S.; Muscari, A. The Involvement of Circulating Microparticles in Inflammation, Coagulation and Cardiovascular Diseases. *Can. J. Cardiol.* **2010**, *26* (4), e140–e145. [https://doi.org/10.1016/S0828-282X\(10\)70371-8](https://doi.org/10.1016/S0828-282X(10)70371-8).
- (73) Cui, Y.; Zheng, L.; Jiang, M.; Jia, R.; Zhang, X.; Quan, Q.; Du, G.; Shen, D.; Zhao, X.; Sun, W.; Xu, H.; Huang, L. Circulating Microparticles in Patients with Coronary Heart Disease and Its Correlation with Interleukin-6 and C-Reactive Protein. *Mol. Biol. Rep.* **2013**, *40* (11), 6437–6442. <https://doi.org/10.1007/s11033-013-2758-1>.

- (74) Drenjancevic, I.; Jukic, I.; Stupin, A.; Cosic, A.; Stupin, M.; Selthofer-Relatic, K. The Markers of Endothelial Activation. In *Endothelial Dysfunction - Old Concepts and New Challenges*; InTech, 2018. <https://doi.org/10.5772/intechopen.74671>.
- (75) Zhang, J.; DeFelice, A. F.; Hanig, J. P.; Colatsky, T. Biomarkers of Endothelial Cell Activation Serve as Potential Surrogate Markers for Drug-Induced Vascular Injury. *Toxicol. Pathol.* **2010**, *38* (6), 856–871. <https://doi.org/10.1177/0192623310378866>.
- (76) Balta, S.; Mikhailidis, D. P.; Demirkol, S.; Ozturk, C.; Celik, T.; Iyisoy, A. Endocan: A Novel Inflammatory Indicator in Cardiovascular Disease? *Atherosclerosis* **2015**, *243* (1), 339–343. <https://doi.org/10.1016/j.atherosclerosis.2015.09.030>.
- (77) Tadzic, R.; Mihalj, M.; Vcev, A.; Ennen, J.; Tadzic, A.; Drenjancevic-Peric, I. The Effects of Arterial Blood Pressure Reduction on Endocan and Soluble Endothelial Cell Adhesion Molecules (CAMs) and CAMs Ligands Expression in Hypertensive Patients on Ca-Channel Blocker Therapy. *Kidney Blood Press. Res.* **2013**, *37* (2–3), 103–115. <https://doi.org/10.1159/000350064>.
- (78) Marin, V.; Kaplanski, G.; Grès, S.; Farnarier, C.; Bongrand, P. Endothelial Cell Culture: Protocol to Obtain and Cultivate Human Umbilical Endothelial Cells. *J. Immunol. Methods* **2001**, *254* (1–2), 183–190. [https://doi.org/10.1016/S0022-1759\(01\)00408-2](https://doi.org/10.1016/S0022-1759(01)00408-2).
- (79) Bouřis, D.; Hospers, G. A. P.; Meijer, C.; Molema, G.; Mulder, N. H. Endothelium in Vitro: A Review of Human Vascular Endothelial Cell Lines for Blood Vessel-Related Research. *Angiogenesis* **2001**, *4* (2), 91–102. <https://doi.org/10.1023/A:1012259529167>.
- (80) Leopold, B.; Strutz, J.; Weiß, E.; Gindlhuber, J.; Birner-Gruenberger, R.; Hackl, H.; Appel, H. M.; Cvitic, S.; Hiden, U. Outgrowth, Proliferation, Viability, Angiogenesis and Phenotype of Primary Human Endothelial Cells in Different Purchasable Endothelial Culture Media: Feed Wisely. *Histochem. Cell Biol.* **2019**, *152* (5), 377–390. <https://doi.org/10.1007/s00418-019-01815-2>.

- (81) Baker, M.; Robinson, S. D.; Lechertier, T.; Barber, P. R.; Tavora, B.; D'Amico, G.; Jones, D. T.; Vojnovic, B.; Hodivala-Dilke, K. Use of the Mouse Aortic Ring Assay to Study Angiogenesis. *Nat. Protoc.* **2012**, *7* (1), 89–104.
<https://doi.org/10.1038/nprot.2011.435>.
- (82) Moleiro, A. F.; Conceição, G.; Leite-Moreira, A. F.; Rocha-Sousa, A. A Critical Analysis of the Available In Vitro and Ex Vivo Methods to Study Retinal Angiogenesis. *J. Ophthalmol.* **2017**, *2017*, 1–19.
<https://doi.org/10.1155/2017/3034953>.
- (83) Elliott, A. D. Confocal Microscopy: Principles and Modern Practices. *Curr. Protoc. Cytom.* **2020**, *92* (1). <https://doi.org/10.1002/cpcy.68>.
- (84) Wiercigroch, E.; Staniszewska-Slezak, E.; Szkaradek, K.; Wojcik, T.; Ozaki, Y.; Baranska, M.; Malek, K. FT-IR Spectroscopic Imaging of Endothelial Cells Response to Tumor Necrosis Factor- α : To Follow Markers of Inflammation Using Standard and High-Magnification Resolution. *Anal. Chem.* **2018**, *90* (6), 3727–3736. <https://doi.org/10.1021/acs.analchem.7b03089>.
- (85) Lichtman, J. W.; Conchello, J.-A. Fluorescence Microscopy. *Nat. Methods* **2005**, *2* (12), 910–919. <https://doi.org/10.1038/nmeth817>.
- (86) Ettinger, A.; Wittmann, T. Fluorescence Live Cell Imaging; 2014; pp 77–94.
<https://doi.org/10.1016/B978-0-12-420138-5.00005-7>.
- (87) Bucevičius, J.; Lukinavičius, G.; Gerasimaitė, R. The Use of Hoechst Dyes for DNA Staining and Beyond. *Chemosensors* **2018**, *6* (2), 18.
<https://doi.org/10.3390/chemosensors6020018>.
- (88) Zhitomirsky, B.; Farber, H.; Assaraf, Y. G. LysoTracker and MitoTracker Red Are Transport Substrates of P-Glycoprotein: Implications for Anticancer Drug Design Evading Multidrug Resistance. *J. Cell. Mol. Med.* **2018**, *22* (4), 2131–2141.
<https://doi.org/10.1111/jcmm.13485>.
- (89) Rumin, J.; Bonnefond, H.; Saint-Jean, B.; Rouxel, C.; Sciandra, A.; Bernard, O.; Cadoret, J.-P.; Bougaran, G. The Use of Fluorescent Nile Red and BODIPY for

- Lipid Measurement in Microalgae. *Biotechnol. Biofuels* **2015**, 8 (1), 42.
<https://doi.org/10.1186/s13068-015-0220-4>.
- (90) Maekawa, M.; Fairn, G. D. Molecular Probes to Visualize the Location, Organization and Dynamics of Lipids. *J. Cell Sci.* **2014**, 127 (22), 4801–4812.
<https://doi.org/10.1242/jcs.150524>.
- (91) Davydova, D.; de la Cadena, A.; Akimov, D.; Dietzek, B. Transient Absorption Microscopy: Advances in Chemical Imaging of Photoinduced Dynamics. *Laser Photon. Rev.* **2016**, 10 (1), 62–81. <https://doi.org/10.1002/lpor.201500181>.
- (92) Ye, T.; Fu, D.; Warren, W. S. Nonlinear Absorption Microscopy. *Photochem. Photobiol.* **2009**, 85 (3), 631–645. <https://doi.org/10.1111/j.1751-1097.2008.00514.x>.
- (93) Brand, J. C. D. The Discovery of the Raman Effect. *Notes Rec. R. Soc. Lond.* **1989**, 43 (1), 1–23.
- (94) Singh, R. The 90th Anniversary of the Raman Effect. *Indian J. Hist. Sci.* **2018**, 53 (1). <https://doi.org/10.16943/ijhs/2018/v53i1/49363>.
- (95) Barańska, M., Małek, K., Bukowska, J., Skirlińska, A., Lipska, K., likowska, A., Czamara, K., Dybaś, J., Głogowska, M., Jaworska, A., Kaczor, A. & Kochan, K. Fundamentals of Raman Scattering Spectroscopy. In *Vibrational spectroscopy from theory to practice*; Malek, K., Ed.; Wydawnictwo Naukowe PWN: Warsaw, 2016; pp 19–25.
- (96) Benjamin Dietzek, Dana Cialla, M. S. and J. P. Introduction to the Fundamentals of Raman Spectroscopy. In *Confocal Raman Microscopy*; Toporski, J., Dieing, T., Hollricher, O., Eds.; Springer Series in Surface Sciences; Springer International Publishing: Cham, 2018; Vol. 66, pp 47–68. <https://doi.org/10.1007/978-3-319-75380-5>.
- (97) Puppels, G. J.; de Mul, F. F. M.; Otto, C.; Greve, J.; Robert-Nicoud, M.; Arndt-Jovin, D. J.; Jovin, T. M. Studying Single Living Cells and Chromosomes by Confocal Raman Microspectroscopy. *Nature* **1990**, 347 (6290), 301–303.

<https://doi.org/10.1038/347301a0>.

- (98) Adar, F.; Mamedov, S.; Whitely, A. Limits of Spatial Resolution of a Raman Microscope. *Microsc. Microanal.* **2005**, *11* (S02).
<https://doi.org/10.1017/S1431927605507384>.
- (99) Urone, P. P.; Hinrichs, R. Limits of Resolution: The Rayleigh Criterion. In *College Physics 2e*; OpenStax: Houston, Texas, 2022.
- (100) Myers, K. A.; Janetopoulos, C. Recent Advances in Imaging Subcellular Processes. *F1000Research* **2016**, *5*, 1553. <https://doi.org/10.12688/f1000research.8399.1>.
- (101) Czamara, K.; Adamczyk, A.; Stojak, M.; Radwan, B.; Baranska, M. Astaxanthin as a New Raman Probe for Biosensing of Specific Subcellular Lipidic Structures: Can We Detect Lipids in Cells under Resonance Conditions? *Cell. Mol. Life Sci.* **2021**, *78* (7), 3477–3484. <https://doi.org/10.1007/s00018-020-03718-1>.
- (102) Yamakoshi, H.; Palonpon, A.; Dodo, K.; Ando, J.; Kawata, S.; Fujita, K.; Sodeoka, M. A Sensitive and Specific Raman Probe Based on Bisarylbutadiyne for Live Cell Imaging of Mitochondria. *Bioorganic Med. Chem. Lett.* **2015**, *25* (3), 664–667.
<https://doi.org/10.1016/j.bmcl.2014.11.080>.
- (103) Bae, K.; Zheng, W.; Ma, Y.; Huang, Z. Real-Time Monitoring of Pharmacokinetics of Mitochondria-Targeting Molecules in Live Cells with Bioorthogonal Hyperspectral Stimulated Raman Scattering Microscopy. *Anal. Chem.* **2020**, *92* (1), 740–748. <https://doi.org/10.1021/acs.analchem.9b02838>.
- (104) Li, Y.; Heo, J.; Lim, C. K.; Pliss, A.; Kachynski, A. V.; Kuzmin, A. N.; Kim, S.; Prasad, P. N. Organelle Specific Imaging in Live Cells and Immuno-Labeling Using Resonance Raman Probe. *Biomaterials* **2015**, *53*, 25–31.
<https://doi.org/10.1016/j.biomaterials.2015.02.056>.
- (105) Yamakoshi, H.; Dodo, K.; Palonpon, A.; Ando, J.; Fujita, K.; Kawata, S.; Sodeoka, M. Alkyne-Tag Raman Imaging for Visualization of Mobile Small Molecules in Live Cells. *J. Am. Chem. Soc.* **2012**, *134* (51), 20681–20689.
<https://doi.org/10.1021/ja308529n>.

- (106) Hu, F.; Zeng, C.; Long, R.; Miao, Y.; Wei, L.; Xu, Q.; Min, W. Supermultiplexed Optical Imaging and Barcoding with Engineered Polyynes. *Nat. Methods* **2018**, *15* (3), 194–200. <https://doi.org/10.1038/nmeth.4578>.
- (107) Tian, S.; Li, H.; Li, Z.; Tang, H.; Yin, M.; Chen, Y.; Wang, S.; Gao, Y.; Yang, X.; Meng, F.; Lauher, J. W.; Wang, P.; Luo, L. Polydiacetylene-Based Ultrastrong Bioorthogonal Raman Probes for Targeted Live-Cell Raman Imaging. *Nat. Commun.* **2020**, *11* (1), 81. <https://doi.org/10.1038/s41467-019-13784-0>.
- (108) Yamakoshi, H.; Dodo, K.; Okada, M.; Ando, J.; Palonpon, A.; Fujita, K.; Kawata, S.; Sodeoka, M. Imaging of EdU, an Alkyne-Tagged Cell Proliferation Probe, by Raman Microscopy. *J. Am. Chem. Soc.* **2011**, *133* (16), 6102–6105. <https://doi.org/10.1021/ja108404p>.
- (109) Hong, S.; Chen, T.; Zhu, Y.; Li, A.; Huang, Y.; Chen, X. Live-Cell Stimulated Raman Scattering Imaging of Alkyne-Tagged Biomolecules. *Angew. Chemie Int. Ed.* **2014**, *53* (23), 5827–5831. <https://doi.org/10.1002/anie.201400328>.
- (110) Chen, Z.; Paley, D. W.; Wei, L.; Weisman, A. L.; Friesner, R. A.; Nuckolls, C.; Min, W. Multicolor Live-Cell Chemical Imaging by Isotopically Edited Alkyne Vibrational Palette. *J. Am. Chem. Soc.* **2014**, *136* (22), 8027–8033. <https://doi.org/10.1021/ja502706q>.
- (111) Asai, T.; Liu, H.; Ozeki, Y.; Sato, S.; Hayashi, T.; Nakamura, H. Imaging of Cellular Uptake of Boron Cluster Compound by Stimulated Raman Scattering Microscopy. *Appl. Phys. Express* **2019**, *12* (11), 112004. <https://doi.org/10.7567/1882-0786/ab4a5d>.
- (112) Wei, L.; Hu, F.; Shen, Y.; Chen, Z.; Yu, Y.; Lin, C.-C.; Wang, M. C.; Min, W. Live-Cell Imaging of Alkyne-Tagged Small Biomolecules by Stimulated Raman Scattering. *Nat. Methods* **2014**, *11* (4), 410–412. <https://doi.org/10.1038/nmeth.2878>.
- (113) Zhang, J.; Yan, S.; He, Z.; Ding, C.; Zhai, T.; Chen, Y.; Li, H.; Yang, G.; Zhou, X.; Wang, P. Small Unnatural Amino Acid Carried Raman Tag for Molecular Imaging of Genetically Targeted Proteins. *J. Phys. Chem. Lett.* **2018**, *9* (16), 4679–

4685. <https://doi.org/10.1021/acs.jpcelett.8b01991>.
- (114) Wei, L.; Shen, Y.; Xu, F.; Hu, F.; Harrington, J. K.; Targoff, K. L.; Min, W. Imaging Complex Protein Metabolism in Live Organisms by Stimulated Raman Scattering Microscopy with Isotope Labeling. *ACS Chem. Biol.* **2015**, *10* (3), 901–908. <https://doi.org/10.1021/cb500787b>.
- (115) Kuzmin, A. N.; Pliss, A.; Lim, C. K.; Heo, J.; Kim, S.; Rzhetskii, A.; Gu, B.; Yong, K. T.; Wen, S.; Prasad, P. N. Resonance Raman Probes for Organelle-Specific Labeling in Live Cells. *Sci. Rep.* **2016**, *6* (1), 1–9. <https://doi.org/10.1038/srep28483>.
- (116) Notingher, I. Raman Spectroscopy Cell-Based Biosensors. *Sensors* **2007**, *7* (8), 1343–1358. <https://doi.org/10.3390/s7081343>.
- (117) Czamara, K.; Petko, F.; Baranska, M.; Kaczor, A. Raman Microscopy at the Subcellular Level: A Study on Early Apoptosis in Endothelial Cells Induced by Fas Ligand and Cycloheximide. *Analyst* **2016**, *141* (4), 1390–1397. <https://doi.org/10.1039/C5AN02202A>.
- (118) Salic, A.; Mitchison, T. J. A Chemical Method for Fast and Sensitive Detection of DNA Synthesis in Vivo. *Proc. Natl. Acad. Sci. U. S. A.* **2008**, *105* (7), 2415–2420. <https://doi.org/10.1073/pnas.0712168105>.
- (119) Basile, D. P.; Friedrich, J. L.; Spahic, J.; Knipe, N.; Mang, H.; Leonard, E. C.; Changizi-Ashtiyani, S.; Bacallao, R. L.; Molitoris, B. A.; Sutton, T. A. Impaired Endothelial Proliferation and Mesenchymal Transition Contribute to Vascular Rarefaction Following Acute Kidney Injury. *Am. J. Physiol. Physiol.* **2011**, *300* (3), F721–F733. <https://doi.org/10.1152/ajprenal.00546.2010>.
- (120) Ishizuka, T.; Liu, H. S.; Ito, K.; Xu, Y. Fluorescence Imaging of Chromosomal DNA Using Click Chemistry. *Sci. Rep.* **2016**, *6* (1), 33217. <https://doi.org/10.1038/srep33217>.
- (121) Jao, C. Y.; Salic, A. Exploring RNA Transcription and Turnover in Vivo by Using Click Chemistry. *Proc. Natl. Acad. Sci.* **2008**, *105* (41), 15779–15784.

<https://doi.org/10.1073/pnas.0808480105>.

- (122) Morimoto, T.; Chiu, L.; Kanda, H.; Kawagoe, H.; Ozawa, T.; Nakamura, M.; Nishida, K.; Fujita, K.; Fujikado, T. Using Redox-Sensitive Mitochondrial Cytochrome Raman Bands for Label-Free Detection of Mitochondrial Dysfunction. *Analyst* **2019**, *144* (8), 2531–2540.
<https://doi.org/10.1039/C8AN02213E>.
- (123) Bik, E.; Mateuszuk, L.; Stojak, M.; Chlopicki, S.; Baranska, M.; Majzner, K. Menadione-Induced Endothelial Inflammation Detected by Raman Spectroscopy. *Biochim. Biophys. Acta - Mol. Cell Res.* **2021**, *1868* (2), 118911.
<https://doi.org/10.1016/j.bbamcr.2020.118911>.
- (124) Pieczara, A.; Matuszyk, E.; Szczesniak, P.; Mlynarski, J.; Baranska, M. Changes in the Mitochondrial Membrane Potential in Endothelial Cells Can Be Detected by Raman Microscopy. *Spectrochim. Acta Part A Mol. Biomol. Spectrosc.* **2023**, *286*, 121978. <https://doi.org/10.1016/j.saa.2022.121978>.
- (125) Baranska, M.; Kaczor, A.; Malek, K.; Jaworska, A.; Majzner, K.; Staniszevska-Slezak, E.; Pacia, M. Z.; Zajac, G.; Dybas, J.; Wiercigroch, E. Raman Microscopy as a Novel Tool to Detect Endothelial Dysfunction. *Pharmacol. Reports* **2015**, *67* (4), 736–743. <https://doi.org/http://dx.doi.org/10.1016/j.pharep.2015.03.015>.
- (126) Majzner, K.; Kochan, K.; Kachamakova-Trojanowska, N.; Maslak, E.; Chlopicki, S.; Baranska, M. Raman Imaging Providing Insights into Chemical Composition of Lipid Droplets of Different Size and Origin: In Hepatocytes and Endothelium. *Anal. Chem.* **2014**, *86* (13), 6666–6674. <https://doi.org/10.1021/ac501395g>.
- (127) Czamara, K.; Majzner, K.; Selmi, A.; Baranska, M.; Ozaki, Y.; Kaczor, A. Unsaturated Lipid Bodies as a Hallmark of Inflammation Studied by Raman 2D and 3D Microscopy. *Sci. Rep.* **2017**, *7*, 40889. <https://doi.org/10.1038/srep40889>.
- (128) Alfonso-García, A.; Pfisterer, S. G.; Riezman, H.; Ikonen, E.; Potma, E. O. D38-Cholesterol as a Raman Active Probe for Imaging Intracellular Cholesterol Storage. *J. Biomed. Opt.* **2016**, *21* (6), 61003.
<https://doi.org/10.1117/1.JBO.21.6.061003>.

- (129) Majzner, K.; Tott, S.; Roussille, L.; Deckert, V.; Chlopicki, S.; Baranska, M. Uptake of Fatty Acids by a Single Endothelial Cell Investigated by Raman Spectroscopy Supported by AFM. *Analyst* **2018**, *143* (4), 970–980. <https://doi.org/10.1039/c7an01043e>.
- (130) Jamieson, L. E.; Greaves, J.; McLellan, J. A.; Munro, K. R.; Tomkinson, N. C. O.; Chamberlain, L. H.; Faulds, K.; Graham, D. Tracking Intracellular Uptake and Localisation of Alkyne Tagged Fatty Acids Using Raman Spectroscopy. *Spectrochim. Acta Part A Mol. Biomol. Spectrosc.* **2018**, *197*, 30–36. <https://doi.org/10.1016/j.saa.2018.01.064>.
- (131) Li, X.; Li, Y.; Jiang, M.; Wu, W.; He, S.; Chen, C.; Qin, Z.; Tang, B. Z.; Mak, H. Y.; Qu, J. Y. Quantitative Imaging of Lipid Synthesis and Lipolysis Dynamics in *Caenorhabditis Elegans* by Stimulated Raman Scattering Microscopy. *Anal. Chem.* **2019**, *91* (3), 2279–2287. <https://doi.org/10.1021/acs.analchem.8b04875>.
- (132) Stiebing, C.; Meyer, T.; Rimke, I.; Matthäus, C.; Schmitt, M.; Lorkowski, S.; Popp, J. Real-Time Raman and SRS Imaging of Living Human Macrophages Reveals Cell-to-Cell Heterogeneity and Dynamics of Lipid Uptake. *J. Biophotonics* **2017**, *10* (9), 1217–1226. <https://doi.org/10.1002/jbio.201600279>.
- (133) van Hinsbergh, V. W. M. Endothelium--Role in Regulation of Coagulation and Inflammation. *Semin. Immunopathol.* **2012**, *34* (1), 93–106. <https://doi.org/10.1007/s00281-011-0285-5>.
- (134) Perera, C. O.; Yen, G. M. Functional Properties of Carotenoids in Human Health. *Int. J. Food Prop.* **2007**, *10* (2), 201–230. <https://doi.org/10.1080/10942910601045271>.
- (135) Kaczor, A.; Baranska, M.; Czamara, K. Carotenoids. In *Carotenoids*; John Wiley & Sons, Ltd: Chichester, UK, 2016; pp 1–13. <https://doi.org/10.1002/9781118622223.ch1>.
- (136) Visioli, F.; Artaria, C. Astaxanthin in Cardiovascular Health and Disease: Mechanisms of Action, Therapeutic Merits, and Knowledge Gaps. *Food Funct.* **2017**, *8* (1), 39–63. <https://doi.org/10.1039/C6FO01721E>.

- (137) Pereira, C.; Souza, A.; Vasconcelos, A.; Prado, P.; Name, J. Antioxidant and Anti-inflammatory Mechanisms of Action of Astaxanthin in Cardiovascular Diseases (Review). *Int. J. Mol. Med.* **2020**, *47* (1), 37–48.
<https://doi.org/10.3892/ijmm.2020.4783>.
- (138) Rao, A. R.; Sindhuja, H. N.; Dharmesh, S. M.; Sankar, K. U.; Sarada, R.; Ravishankar, G. A. Effective Inhibition of Skin Cancer, Tyrosinase, and Antioxidative Properties by Astaxanthin and Astaxanthin Esters from the Green Alga *Haematococcus Pluvialis*. *J. Agric. Food Chem.* **2013**, *61* (16), 3842–3851.
<https://doi.org/10.1021/jf304609j>.
- (139) Kim, H.-Y.; Kim, Y.-M.; Hong, S. Astaxanthin Suppresses the Metastasis of Colon Cancer by Inhibiting the MYC-Mediated Downregulation of MicroRNA-29a-3p and MicroRNA-200a. *Sci. Rep.* **2019**, *9* (1), 9457. <https://doi.org/10.1038/s41598-019-45924-3>.
- (140) Ni, Y.; Nagashimada, M.; Zhuge, F.; Zhan, L.; Nagata, N.; Tsutsui, A.; Nakanuma, Y.; Kaneko, S.; Ota, T. Astaxanthin Prevents and Reverses Diet-Induced Insulin Resistance and Steatohepatitis in Mice: A Comparison with Vitamin E. *Sci. Rep.* **2015**, *5*, 17192. <https://doi.org/10.1038/srep17192>.
- (141) Baranska, M.; Dobrowolski, J. C.; Zajac, G. In Situ Studies of Carotenoids in Plants and Animals. In *Carotenoids*; John Wiley & Sons, Ltd: Chichester, UK, 2016; pp 131–146. <https://doi.org/10.1002/9781118622223.ch8>.
- (142) Withnall, R.; Chowdhry, B. Z.; Silver, J.; Edwards, H. G. M.; de Oliveira, L. F. C. Raman Spectra of Carotenoids in Natural Products. *Spectrochim. Acta Part A Mol. Biomol. Spectrosc.* **2003**, *59* (10), 2207–2212.
[https://doi.org/https://doi.org/10.1016/S1386-1425\(03\)00064-7](https://doi.org/https://doi.org/10.1016/S1386-1425(03)00064-7).
- (143) Akbarzadeh, A.; Rezaei-Sadabady, R.; Davaran, S.; Joo, S. W.; Zarghami, N.; Hanifehpour, Y.; Samiei, M.; Kouhi, M.; Nejati-Koshki, K. Liposome: Classification, Preparation, and Applications. *Nanoscale Res. Lett.* **2013**, *8* (1), 102. <https://doi.org/10.1186/1556-276X-8-102>.
- (144) Trif, M.; Craciunescu, O. Liposome as Efficient System for Intracellular Delivery

of Bioactive Molecules. In *Nanotechnology and Functional Foods*; John Wiley & Sons, Ltd: Chichester, UK, 2015; pp 191–213.

<https://doi.org/10.1002/9781118462157.ch12>.

- (145) Sangsuriyawong, A.; Limpawattana, M.; Siriwan, D.; Klaypradit, W. Properties and Bioavailability Assessment of Shrimp Astaxanthin Loaded Liposomes. *Food Sci. Biotechnol.* **2019**, *28* (2), 529–537. <https://doi.org/10.1007/s10068-018-0495-x>.
- (146) Shimokawa, T.; Yoshida, M.; Fukuta, T.; Tanaka, T.; Inagi, T.; Kogure, K. Efficacy of High-Affinity Liposomal Astaxanthin on up-Regulation of Age-Related Markers Induced by Oxidative Stress in Human Corneal Epithelial Cells. *J. Clin. Biochem. Nutr.* **2019**, *64* (1), 27–35. <https://doi.org/10.3164/jcbn.18-27>.
- (147) Chiu, C.-H.; Chang, C.-C.; Lin, S.-T.; Chyau, C.-C.; Peng, R. Improved Hepatoprotective Effect of Liposome-Encapsulated Astaxanthin in Lipopolysaccharide-Induced Acute Hepatotoxicity. *Int. J. Mol. Sci.* **2016**, *17* (7), 1128. <https://doi.org/10.3390/ijms17071128>.
- (148) Radwan, B.; Rocchetti, S.; Matuszyk, E.; Sternak, M.; Stodulski, M.; Pawlowski, R.; Mlynarski, J.; Brzozowski, K.; Chlopicki, S.; Baranska, M. EdU Sensing: The Raman Way of Following Endothelial Cell Proliferation in Vitro and Ex Vivo. *Biosens. Bioelectron.* **2022**, *216* (August), 114624. <https://doi.org/10.1016/j.bios.2022.114624>.
- (149) Bulin, A.-L.; Broekgaarden, M.; Hasan, T. Comprehensive High-Throughput Image Analysis for Therapeutic Efficacy of Architecturally Complex Heterotypic Organoids. *Sci. Rep.* **2017**, *7* (1), 16645. <https://doi.org/10.1038/s41598-017-16622-9>.
- (150) Li, X.; Dancausse, H.; Grijalva, I.; Oliveira, M.; Levi, A. D. O. Labeling Schwann Cells with CFSE—an in Vitro and in Vivo Study. *J. Neurosci. Methods* **2003**, *125* (1–2), 83–91. [https://doi.org/10.1016/S0165-0270\(03\)00044-X](https://doi.org/10.1016/S0165-0270(03)00044-X).
- (151) Gerdes, J. Ki-67 and Other Proliferation Markers Useful for Immunohistological Diagnostic and Prognostic Evaluations in Human Malignancies. *Semin. Cancer*

Biol. **1990**, *1* (3), 199–206.

- (152) Sun, X.; Bizhanova, A.; Matheson, T. D.; Yu, J.; Zhu, L. J.; Kaufman, P. D. Ki-67 Contributes to Normal Cell Cycle Progression and Inactive X Heterochromatin in P21 Checkpoint-Proficient Human Cells. *Mol. Cell. Biol.* **2017**, *37* (17).
<https://doi.org/10.1128/MCB.00569-16>.
- (153) Matatall, K. A.; Kadmon, C. S.; King, K. Y. Detecting Hematopoietic Stem Cell Proliferation Using BrdU Incorporation. *Methods Mol. Biol.* **2018**, *1686*, 91–103.
https://doi.org/10.1007/978-1-4939-7371-2_7.
- (154) Flomerfelt, F. A.; Gress, R. E. Analysis of Cell Proliferation and Homeostasis Using EdU Labeling. *Methods Mol. Biol.* **2016**, *1323*, 211–220.
https://doi.org/10.1007/978-1-4939-2809-5_18.
- (155) Matuszyk, E.; Adamczyk, A.; Radwan, B.; Pieczara, A.; Szcześniak, P.; Mlynarski, J.; Kamińska, K.; Baranska, M. Multiplex Raman Imaging of Organelles in Endothelial Cells. *Spectrochim. Acta Part A Mol. Biomol. Spectrosc.* **2021**, *255*, 119658. <https://doi.org/10.1016/j.saa.2021.119658>.
- (156) Henriksson, S.; Groth, P.; Gustafsson, N.; Helleday, T. Distinct Mechanistic Responses to Replication Fork Stalling Induced by Either Nucleotide or Protein Deprivation. *Cell Cycle* **2018**, *17* (5), 568–579.
<https://doi.org/10.1080/15384101.2017.1387696>.
- (157) Liu, X.; Yang, J.-M.; Zhang, S. S.; Liu, X.-Y.; Liu, D. X. Induction of Cell Cycle Arrest at G1 and S Phases and CAMP-Dependent Differentiation in C6 Glioma by Low Concentration of Cycloheximide. *BMC Cancer* **2010**, *10* (1), 684.
<https://doi.org/10.1186/1471-2407-10-684>.
- (158) Liu, S. J.; Melchert, R. B. In Vitro Cultured Cardiomyocytes for Evaluating Cardiotoxicity. In *Comprehensive Toxicology*; Elsevier, 2010; pp 113–131.
<https://doi.org/10.1016/B978-0-08-046884-6.00706-5>.
- (159) Yang, T.; Chettri, A.; Radwan, B.; Matuszyk, E.; Baranska, M.; Dietzek, B. Monitoring Excited-State Relaxation in a Molecular Marker in Live Cells—a Case

- Study on Astaxanthin. *Chem. Commun.* **2021**, 57 (52), 6392–6395.
<https://doi.org/10.1039/D1CC01907D>.
- (160) Siebert, R.; Akimov, D.; Schmitt, M.; Winter, A.; Schubert, U. S.; Dietzek, B.; Popp, J. Spectroscopic Investigation of the Ultrafast Photoinduced Dynamics in π -Conjugated Terpyridines. *ChemPhysChem* **2009**, 10 (6), 910–919.
<https://doi.org/10.1002/cphc.200800847>.
- (161) Zhu, Y.; Cheng, J.-X. Transient Absorption Microscopy: Technological Innovations and Applications in Materials Science and Life Science. *J. Chem. Phys.* **2020**, 152 (2), 020901. <https://doi.org/10.1063/1.5129123>.
- (162) Fuciman, M.; Durchan, M.; Šlouf, V.; Keřan, G.; Polívka, T. Excited-State Dynamics of Astaxanthin Aggregates. *Chem. Phys. Lett.* **2013**, 568–569, 21–25.
<https://doi.org/10.1016/j.cplett.2013.03.009>.
- (163) Billsten, H. H.; Sundström, V.; Polívka, T. Self-Assembled Aggregates of the Carotenoid Zeaxanthin: Time-Resolved Study of Excited States. *J. Phys. Chem. A* **2005**, 109 (8), 1521–1529. <https://doi.org/10.1021/jp044847j>.
- (164) Radwan, B.; Matuszyk, E.; Rocchetti, S.; Prabhakaran, A.; Sternak, M.; Chlopicki, S.; Keyes, T. E.; Baranska, M. Multimodal Imaging of Endothelial Pathology Models in Vitro and Ex Vivo. In *the 7th International Conference on Molecular Sensors and Molecular Logic Gates (MSMLG 2022)*; Dublin, Ireland, 2022.
- (165) Reiterer, M.; Branco, C. M. Endothelial Cells and Organ Function: Applications and Implications of Understanding Unique and Reciprocal Remodelling. *FEBS J.* **2020**, 287 (6), 1088–1100. <https://doi.org/10.1111/febs.15143>.
- (166) Ribatti, D.; Tamma, R.; Annese, T. The Role of Vascular Niche and Endothelial Cells in Organogenesis and Regeneration. *Exp. Cell Res.* **2021**, 398 (1), 112398.
<https://doi.org/10.1016/j.yexcr.2020.112398>.
- (167) Bik, E.; Dorosz, A.; Mateuszuk, L.; Baranska, M.; Majzner, K. Fixed versus Live Endothelial Cells: The Effect of Glutaraldehyde Fixation Manifested by Characteristic Bands on the Raman Spectra of Cells. *Spectrochim. Acta Part A*

- Mol. Biomol. Spectrosc.* **2020**, *240*, 118460.
<https://doi.org/10.1016/j.saa.2020.118460>.
- (168) Dębowska, K.; Dębski, D.; Michałowski, B.; Dybala-Defratyka, A.; Wójcik, T.; Michalski, R.; Jakubowska, M.; Selmi, A.; Smulik, R.; Piotrowski, Ł.; Adamus, J.; Marcinek, A.; Chlopicki, S.; Sikora, A. Characterization of Fluorescein-Based Monoboronate Probe and Its Application to the Detection of Peroxynitrite in Endothelial Cells Treated with Doxorubicin. *Chem. Res. Toxicol.* **2016**, *29* (5), 735–746. <https://doi.org/10.1021/acs.chemrestox.5b00431>.
- (169) Majzner, K.; Wojcik, T.; Szafraniec, E.; Lukawska, M.; Oszczapowicz, I.; Chlopicki, S.; Baranska, M. Nuclear Accumulation of Anthracyclines in the Endothelium Studied by Bimodal Imaging: Fluorescence and Raman Microscopy. *Analyst* **2015**, *140* (7), 2302–2310. <https://doi.org/10.1039/C4AN01882F>.
- (170) Wojcik, T.; Buczek, E.; Majzner, K.; Kolodziejczyk, A.; Miszczyk, J.; Kaczara, P.; Kwiatek, W.; Baranska, M.; Szymonski, M.; Chlopicki, S. Comparative Endothelial Profiling of Doxorubicin and Daunorubicin in Cultured Endothelial Cells. *Toxicol. Vitro.* **2015**, *29* (3), 512–521.
<https://doi.org/10.1016/j.tiv.2014.12.009>.
- (171) Manska, S.; Octaviano, R.; Rossetto, C. C. 5-Ethynyl-2'-Deoxycytidine and 5-Ethynyl-2'-Deoxyuridine Are Differentially Incorporated in Cells Infected with HSV-1, HCMV, and KSHV Viruses. *J. Biol. Chem.* **2020**, *295* (18), 5871–5890.
<https://doi.org/10.1074/jbc.RA119.012378>.
- (172) Haskins, J. S.; Su, C.; Maeda, J.; Walsh, K. D.; Haskins, A. H.; Allum, A. J.; Froning, C. E.; Kato, T. A. Evaluating the Genotoxic and Cytotoxic Effects of Thymidine Analogs, 5-Ethynyl-2'-Deoxyuridine and 5-Bromo-2'-Deoxyuridine to Mammalian Cells. *Int. J. Mol. Sci.* **2020**, *21* (18), 6631.
<https://doi.org/10.3390/ijms21186631>.
- (173) Slipchenko, M. N.; Cheng, J.-X. Nonlinear Raman Spectroscopy: Coherent Anti-Stokes Raman Scattering (CARS). In *Encyclopedia of Biophysics*; Springer Berlin Heidelberg: Berlin, Heidelberg, 2013; pp 1744–1750. <https://doi.org/10.1007/978->

3-642-16712-6_136.

- (174) Hu, F.; Shi, L.; Min, W. Biological Imaging of Chemical Bonds by Stimulated Raman Scattering Microscopy. *Nat. Methods* **2019**, *16* (9), 830–842. <https://doi.org/10.1038/s41592-019-0538-0>.
- (175) Prince, R. C.; Frontiera, R. R.; Potma, E. O. Stimulated Raman Scattering: From Bulk to Nano. *Chem. Rev.* **2017**, *117* (7), 5070–5094. <https://doi.org/10.1021/acs.chemrev.6b00545>.
- (176) Jones, R. R.; Hooper, D. C.; Zhang, L.; Wolverson, D.; Valev, V. K. Raman Techniques: Fundamentals and Frontiers. *Nanoscale Res. Lett.* **2019**, *14* (1), 231. <https://doi.org/10.1186/s11671-019-3039-2>.
- (177) Li, S.; Li, Y.; Yi, R.; Liu, L.; Qu, J. Coherent Anti-Stokes Raman Scattering Microscopy and Its Applications. *Front. Phys.* **2020**, *8*. <https://doi.org/10.3389/fphy.2020.598420>.
- (178) Hein, J. E.; Fokin, V. V. Copper-Catalyzed Azide–Alkyne Cycloaddition (CuAAC) and beyond: New Reactivity of Copper(i) Acetylides. *Chem. Soc. Rev.* **2010**, *39* (4), 1302. <https://doi.org/10.1039/b904091a>.
- (179) Haldón, E.; Nicasio, M. C.; Pérez, P. J. Copper-Catalysed Azide–Alkyne Cycloadditions (CuAAC): An Update. *Org. Biomol. Chem.* **2015**, *13* (37), 9528–9550. <https://doi.org/10.1039/C5OB01457C>.